Measurement of Branching Fractions of Rare Charmless Hadronic B Decays to $\pi^+\pi^0K_S^0$

by

David Knowles

A thesis submitted to

The University of Birmingham

for the degree of

Doctor of Philosophy

Particle Physics Group

School of Physics and Astronomy

University of Birmingham

June 2003

Abstract

In this report branching fraction limits at 90% CL are presented for the three body final state $B^+ \to K^0_S \pi^+ \pi^0$, through the resonances:

$B(B \to K^{*0}\pi^+, K^{*0} \to K^0_S \pi^0) \ < 3 \times 10^{-6}$ 90%CL
$B(B \to K^{*+}\pi^0, K^{*+} \to K^0_S \pi^+) \ < 1 \times 10^{-7}$ 90%CL
$B(B \to K^0_S \rho^+, \rho^+ \to \pi^0 \pi^+) \ < 8 \times 10^{-7}$ 90%CL

Charge conjugate states are also included in the results. No effort is made to separate these conjugate states. The data used for these analyses was 22.1×10^6 B^+B^- pairs produced by the PEP-II collider at SLAC and detected by the BaBar detector in 1999-2001.

Acknowledgements

I would first like to thank the Birmingham University Particle Physics department for giving me the opportunity to do a PhD in particle physics. My thanks also go to PPARC who funded me throughout my course and allowed me to work at SLAC and experience life in California. A thanks also goes out to all those behind the PEP-II B meson factory, whose tireless efforts produced the data that made this report possible.

On a more personal note I would like to thank my supervisor Chris Hawkes and fellow scientists at Birmingham; Alan Watson, Nigel Watson, Theresa Harrison and everyone else who helped in creating a friendly and supportive working atmosphere.

A special thanks goes out to my family and friends whose constant belief and support throughout my educational life made this possible. And to my partner who supported me through the whole experience I owe my greatest thanks.

Declaration

I declare that no part of this thesis has been previously presented to this, or any other university as part of the requirements of a higher degree. The experimental analysis described in this document was undertaken by the BaBar Collaboration of which I have been a member since 1999. I have helped to run the detector, process the data and improve ongoing monitoring. The preselection code was written by the non-charm B three-body decay group. All the analysis after the preselection is my own work except where stated and referenced in the text.

Contents

List of Tables

List of Figures

Chapter 1

Introduction

1.1 Introduction

Our universe is believed to have originated from the Big Bang. However, from this explosion came not only matter but anti-matter as well. Theory once assumed baryonic symmetry, with no distinction as to whether the universe was made out of matter or anti-matter. Since the creation of the universe these particles and anti-particles have been annihilating each other, reversing the creation process. Today we see vast quantities of matter objects: planets, stars and galaxies; yet we see no anti-matter. Due to our very existence we must refute our earlier hypothesis of matter-antimatter symmetry. In refuting it we must study the asymmetry problem. The BaBar experiment is designed to do just this. The BaBar experiment is not the first experiment to investigate such a phenomenon.

C is the charge conjugation operator, P is the parity operator. Together they change the sign of the quantum numbers and invert the spatial coordinates of a particle. When combined they transform a particle into its anti-particle. If the combined quantum number is conserved then there is no asymmetry between matter and anti-matter. However, if CP can be shown to be violated it proves there is such an asymmetry. The first CP violating process was observed by J.H. Christenson et al in 1964 [1] in the neutral kaon system $K_L \to \pi\pi$. This decay was observed to occur with 10^{-3} branching fraction.

Further weight was added to the importance of CP violation by A.D. Sakharov in 1967 [2]. He stated that for an asymmetric universe to occur the following criteria must have been simultaneously met during the evolution of the universe.

- A baryon number violating process.
- CP violation.
- The universe out of thermal equilibrium.

CP violation is known to be allowed in the Standard Model (SM). It is a result of one non-trivial phase in the Cabibbo-Kobayashi-Maskawa (CKM) mixing matrix that relates the quark mass eigenstate to the weak interaction eigenstates. This asymmetry within the Standard Model, in its present understanding, is not large enough to create the matter anti-matter asymmetry observed in the universe. However this area of the Standard Model is one of the least experimentally constrained. This fact alone makes it an area of interest. It may not only increase our understanding of the Standard Model but also help discover new physics [3].

Before the BaBar experiment commenced, *CP* violation had not been observed outside the neutral kaon system.

The B meson system is an excellent environment to study *CP* violation. Its many decay modes relate to the CKM matrix elements, which can be measured through branching fractions. The phase of the CKM matrix can be measured through *CP* violating asymmetries. i.e. the difference between the branching fraction of one B meson decay and that of the *CP* conjugate process. B mesons are bound states of a b quark (anti-quark) and a light anti-quark (quark). The b quark was first discovered in the bound state $b\bar{b}$ in 1977 [4], designated Υ. PEP-II collides electrons and positrons at the Υ(4S) resonance, which has an energy just above that of a pair of B^+B^- or

$B^0\overline{B^0}$ mesons. This decay to $B\overline{B}$ is observed 100% of the time. The B^0 or $B^{\pm}$ mesons produced have very little momentum in the $\Upsilon(4S)$ rest frame. This is utilized in measuring time-dependent CP asymmetries. PEP-II can produce an unprecedented luminosity, which is paramount due to the small branching fractions of the interesting B decays. BaBar, after two years of running, had already observed CP violation in B mesons [5]. Within the next few years the BaBar experiment will be able to make a precision test of CP violation in the Standard Model.

This report presents the work carried out on the three body final state $B^+ \to K^0_S\pi^0\pi^+$. This mode has yet to be observed. This final state is accessible through resonant modes and direct processes. These not only help in measuring the CKM matrix parameters but can also be used as a portal for new physics research. This, and some of the theory behind the BaBar experiment, is covered in chapter two of this report.

Production and detection of such rare modes requires the use of a unique machine capable of high luminosity and excellent particle detection methods. The production and detection of the particles used in this report was made possible by the PEP-II BaBar system. Chapter three will give an introduction into the Stanford Linear Accelerator and PEP-II system with a detailed description of the BaBar sub-detectors and their uses.

Identification of specific particles and decays from the large amounts of data produced by BaBar makes necessary the development of specific analysis techniques. These techniques begin with a general reduction of unwanted events before more detailed identification methods are imposed. Chapter four presents a detailed look at the analysis techniques used by BaBar and those developed specifically for this report.

The results obtained from my study will then be presented in chapter five. Here I will present my findings and the conclusions I drew from them.

Chapter 2

CP Violation in the B Meson System

2.1 Introduction

This chapter will introduce some of the theory behind *CP* violation. It will begin by defining the Charge Conjugation, Parity and Time Reversal quantum operators and how *CP* violation arises. Following this will be a discussion of *CP* violation in the Standard Model via the Cabbibo-Kobayashi-Maskawa (CKM) matrix and its testability through the Unitarity Triangle. Next there will be a section covering the different types of *CP* violation within the B meson system before going on to look at charmless hadronic physics in BaBar and the role played by the modes covered in this report. At the end of this chapter there is a short summary of some possible new physics that could be observed through these decays.

2.2 CP Violation in Field Theory

The charge conjugation operator C changes a particle, described by the wavefunction $|f(\vec{p},\vec{s})\rangle$, where p and s are its momentum and spin respectively, into its anti-particle. The anti-particle is defined by reversing the signs of all the charges associated with the particle.

$$C|f(\vec{p},\vec{s})\rangle = \eta_c|\bar{f}(\vec{p},\vec{s})\rangle \tag{2.1}$$

where η_c is a phase. The parity operator P transforms the space vector r into $-r$. The momentum $\vec{p} = m\frac{d\vec{r}}{dt}$ also changes so p becomes $-p$. However, the orbital angular momentum L remains unchanged ($\vec{L} = \vec{r} \times \vec{p}$). The spin of the particle is not affected. However the helicity, defined as $\lambda = \frac{\vec{p}}{|\vec{p}|}.\vec{s}$ is reversed.

$$P|f(\vec{p},\vec{s})\rangle = \eta_p|f(-\vec{p},\vec{s})\rangle \tag{2.2}$$

The time reversal operator replaces t by $-t$. Because of this both momentum and spin are changed to negative values. This results in the helicity remaining unchanged. The wavefunction describing the particle is also replaced by its complex conjugate.

$$T|f(\vec{p},\vec{s})\rangle = \eta_T|f(-\vec{p},-\vec{s})\rangle^* \tag{2.3}$$

The CP transformation is the combination of the parity operator and the charge-conjugation operator. The combination of both operators replaces a particle by its anti-particle, reversing both its momentum and helicity.

In quantum field theory a Hamiltonian operator H is invariant under a Lorentz transformation and is invariant under combined CPT transformations. An unstable particle can be regarded as an eigenstate of the effective hamiltonian:

$$H = M - \frac{i}{2}\Gamma \tag{2.4}$$

where M is the mass and Γ is the total decay width. So CPT invariance implies that the mass and the lifetime of the particle and anti-particle are equal, but partial decay widths may still be different. The conservation of CPT implies that when we violate CP, T is also violated. As stated the time reversal operator transforms H into it's complex conjugate H^*. Hence if $H \neq H^*$ then CP is violated.

2.3 CP Violation in the Standard Model

Now we have discussed how CP violation may arise we will now examine how this phenomenon is generated within the Standard Model. The mechanism for producing CP violation in the Standard Model was introduced in 1973 [6]. In the Standard Model fermions appear in three families. These fermions experience two types of interactions: gauge interactions, where two fermions couple to a gauge boson, and Yukawa interactions, where two fermions couple to a scalar. In the Standard Model there are twelve gauge bosons, related to the gauge symmetry

$$G_{SM} = SU(3)_C \times SU(2)_L \times U(1)_Y \tag{2.5}$$

and a single Higgs scalar, related to the spontaneous symmetry breaking.

$$G_{SM} \to SU(3)_C \times U(1)_{EM}. \tag{2.6}$$

The Standard Model gauge interactions do not distinguish between the different generations. The interaction of the $SU(2)_L$ gauge boson W_μ^a (a=1,2,3) with quarks is described by:

$$-L_W = \frac{g}{2}\overline{Q^I_{L_i}}\gamma^\mu \tau^a Q^I_{L_i} W^a_\mu \tag{2.7}$$

The index I corresponds to the interaction eigenstate. L means they are left handed doublets with the index i referring to the generation index i.e. i = 1,2,3. The Dirac matrix γ^μ, describing two spin 1/2 quark fields and one spin-1 gauge boson field, operates in Lorentz space. The 2×2 τ^a matrix operates in the $SU(2)_L$ space and it describes the combination of the two quark doublets and W^a triplet into an $SU(2)_L$ singlet.

The Yukawa interactions involve 3×3 complex matrices and couplings between fermions from different generations. In order to generate quark masses we must transform to the mass basis. This is achieved through spontaneous symmetry breaking. Within the Standard Model this symmetry breaking is the result of a vacuum expectation value of the neutral component of the Higgs doublet. After this spontaneous symmetry breaking the resultant mass matrices are not diagonal. They can be diagonalise by biunitary transformations. Then the charged current interactions in the mass basis are represented as:

$$-L_{W^{\pm}} = \frac{g}{\sqrt{2}}\overline{u_{Li}}\gamma^{\mu}\left(V_{uL}V_{dL}^{\dagger}\right)_{ij}d_{Lj}W_{\mu}^{+} + \text{h.c} \tag{2.8}$$

where $W^{\pm}$ are the observed charge gauge bosons and $(V_{uL}V_{dL}^{\dagger})$ is the 3×3 unitary matrix known as the CKM matrix. This matrix relates the weak eigenstates to the mass eigenstates.

$$V_{CKM} = V_{uL}V_{dL}^{\dagger} = \begin{pmatrix} V_{ud} & V_{us} & V_{ub} \\ V_{cd} & V_{cs} & V_{cb} \\ V_{td} & V_{ts} & V_{tb} \end{pmatrix} \tag{2.9}$$

2.3.1 The CKM matrix

The V_{CKM} matrix is the mixing matrix for quark flavours as described in [6] [7]. The CKM matrix is complex and contains three dimensions, therefore it consists of eighteen free parameters. Exploiting the unitarity of the CKM matrix provides nine constraints. Of the remaining free parameters three can be defined as the Euler angles, which is the number of independent rotations in three dimensions. This results in six parameters that are pure phases.

The quark fields can be re-phased by the following.

$$\begin{pmatrix} u_L^{'} \\ c_L^{'} \\ t_L^{'} \end{pmatrix} = \begin{pmatrix} e^{i\phi_u} & 0 & 0 \\ 0 & e^{i\phi_c} & 0 \\ 0 & 0 & e^{i\phi_t} \end{pmatrix} \begin{pmatrix} u_L \\ c_L \\ t_L \end{pmatrix}$$

$$\begin{pmatrix} d_L^{'} \\ s_L^{'} \\ b_L^{'} \end{pmatrix} = \begin{pmatrix} e^{i\phi_d} & 0 & 0 \\ 0 & e^{i\phi_s} & 0 \\ 0 & 0 & e^{i\phi_b} \end{pmatrix} \begin{pmatrix} d_L \\ s_L \\ b_L \end{pmatrix} \tag{2.10}$$

The result of this transformation is that V_{CKM} becomes

$$V_{CKM}^{'} = \begin{pmatrix} e^{i(\phi_u-\phi_d)}V_{ud} & e^{i(\phi_u-\phi_s)}V_{us} & e^{i(\phi_u-\phi_b)}V_{ub} \\ e^{i(\phi_c-\phi_d)}V_{cd} & e^{i(\phi_c-\phi_s)}V_{cs} & e^{i(\phi_c-\phi_b)}V_{cb} \\ e^{i(\phi_t-\phi_d)}V_{td} & e^{i(\phi_t-\phi_s)}V_{ts} & e^{i(\phi_t-\phi_b)}V_{tb} \end{pmatrix} \tag{2.11}$$

It is only possible to observe relative phases. This allows the removal of five of the six phases in the CKM matrix. The last phase cannot be removed, hence this remaining phase, δ, is the source of CP violation within the Standard Model.

It is possible to parameterise the CKM matrix in many different ways. The first being put forward in 1973 by Kobayashi and Maskawa [6]. The parameterisation adopted by the Particle Data Group [8] is:

$$V = \begin{pmatrix} 1 & 0 & 0 \\ 0 & c_{23} & s_{23} \\ 0 & -s_{23} & c_{23} \end{pmatrix} \begin{pmatrix} c_{13} & 0 & s_{13}e^{-i\delta_{13}} \\ 0 & 1 & 0 \\ -s_{13}e^{i\delta_{13}} & 0 & c_{13} \end{pmatrix} \begin{pmatrix} c_{12} & s_{12} & 0 \\ -s_{12} & c_{12} & 0 \\ 0 & 0 & 1 \end{pmatrix}$$

$$= \begin{pmatrix} c_{12}c_{13} & s_{12}c_{13} & s_{13}e^{-i\delta} \\ -s_{12}c_{23} - c_{12}s_{23}s_{13}e^{i\delta} & c_{12}c_{23} - s_{12}s_{23}s_{13}e^{i\delta} & s_{23}c_{13} \\ s_{12}s_{13} - c12c_{23}s_{13}e^{i\delta} & -c_{12}s_{23} - s_{12}c_{23}s_{13}e^{i\delta} & c_{23}c_{13} \end{pmatrix} \tag{2.12}$$

where $c_{ij} \equiv \cos\theta_{ij}$ and $s_{ij} \equiv \sin\theta_{ij}$, represent the three Euler mixing angles ($i \neq j$). δ represents the phase that is the source of CP violation.

For CP violation within the CKM matrix a number of conditions must be met. $\theta_{ij} \neq 0$ or 2π and $\delta \neq 0$ or π. All necessary conditions for CP violation can be grouped together into a single variable. This was first shown by Jarlskog [9] with the following equation.

$$J = c_{12}c_{23}c_{13}^{2}s_{12}s_{23}s_{13}sin\delta \tag{2.13}$$

This explicitly shows the requirements on the mixing angles and δ. As the magnitude of J is estimated to be small (order of 10^{-4}) [10], CP violation in the Standard Model is expected to be a small effect.

Further simplification of the CKM matrix was introduced by Wolfenstein in 1983 [11]. It was based upon the observation $|V_{cb}| \approx |V_{us}|^2$. This parameterisation upholds unitarity to an approximation.

$$V = \begin{pmatrix} 1-\frac{\lambda^2}{2} & \lambda & A\lambda^3(\rho - i\eta) \\ -\lambda & 1-\frac{\lambda^2}{2} & A\lambda^2 \\ A\lambda^3(1-\rho-i\eta) & -A\lambda^2 & 1 \end{pmatrix} + \mathcal{O}(\lambda^4) \tag{2.14}$$

where $\lambda = \sin\theta_{12} \approx 0.22$ and the phase is given by η. The quantities A and ρ are real numbers of order unity. The quark mixing parameters can only be determined from weak interaction processes. There are three ways to determine the CKM parameters.

1. Direct measurements: Standard Model tree level processes;
2. Unitarity: relations among the CKM elements following from $V_{CKM}V^{\dagger}_{CKM} = \mathbf{1}$;
3. Indirect measurements: Standard Model loop processes.

It is possible to measure six of the nine CKM elements by Standard Model tree level processes. To determine even more parameters we exploit the unitarity of the matrix to produce unitarity triangles.

2.3.2 The Unitarity Triangle

To further study the CKM matrix and hence CP violation within the Standard Model it is possible to exploit the unitary nature of the matrix. The unitarity of the CKM matrix $VV^{\dagger} = 1$ gives

$$V_{ud}V^*_{us} + V_{cd}V^*_{cs} + V_{td}V^*_{ts} = 0, \tag{2.15}$$

$$V_{us}V^*_{ub} + V_{cs}V^*_{cb} + V_{ts}V^*_{tb} = 0, \tag{2.16}$$

$$V_{ud}V^*_{ub} + V_{cd}V^*_{cb} + V_{td}V^*_{tb} = 0. \tag{2.17}$$

These relations can be represented graphically as triangles in a complex $\rho - \eta$ plane. There are six such triangles (three more from $V^{\dagger}V$) with the same area, which is proportional to the amount of CP violation in the Standard Model. Equation 2.15 is most closely related to CP violation in the K meson system and equation 2.16 is most closely related to CP violation in the B_s system. The BaBar experiment concerns itself with equation 2.17, which is associated with the CP violation in the B_d system. Figure 2.1 shows the triangle corresponding to equation 2.17 in the Wolfenstein parameterisation. Here the phase is present in the V_{ub} and V_{td} terms. Dividing by $V_{cd}V_{cb}^*$ normalises the base of the triangle and forms the apex (ρ,η) in the complex plane. Then the angles α, β, γ and sides R_b and R_t are given by,

$$\alpha \equiv arg\left[-\frac{V_{td}V_{tb}^*}{V_{ud}V_{ub}^*}\right], \qquad \beta \equiv arg\left[-\frac{V_{cd}V_{cb}^*}{V_{td}V_{tb}^*}\right], \qquad \gamma \equiv arg\left[-\frac{V_{ud}V_{ub}^*}{V_{cd}V_{cb}^*}\right], \tag{2.18}$$

$$R_b \equiv \sqrt{\overline{\rho}^2 + \overline{\eta}^2} = \frac{1-\lambda^2/2}{\lambda}\left|\frac{V_{ub}}{V_{cb}}\right|, \qquad R_t \equiv \sqrt{(1-\overline{\rho}^2 + \overline{\eta}^2} = \frac{1}{\lambda}\left|\frac{V_{td}}{V_{cb}}\right| \tag{2.19}$$

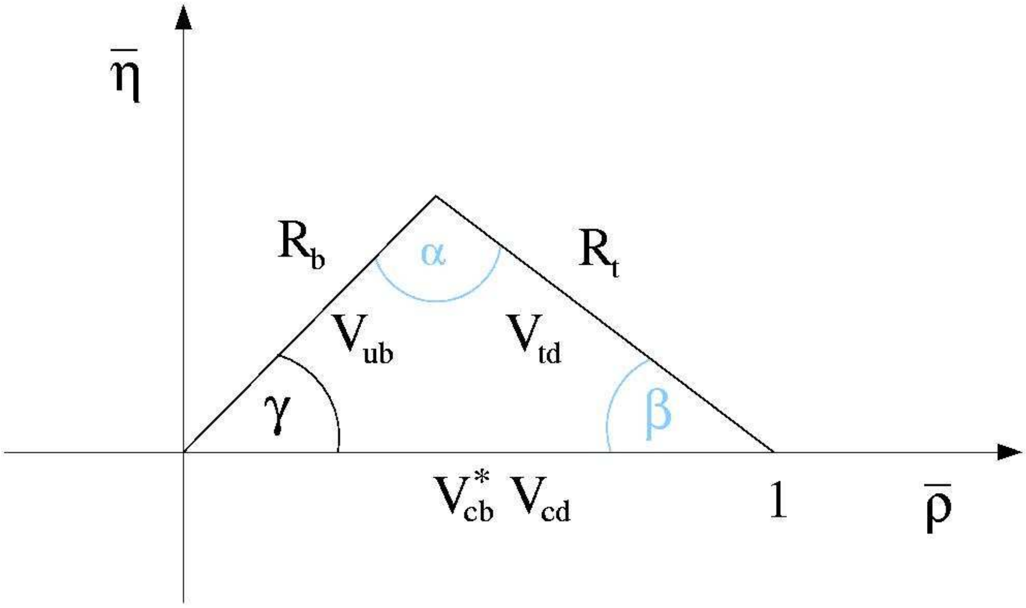

Figure 2.1: Diagram showing the Unitarity triangle associated with equation 2.17 in the Wolfenstein parameterisation.

The area of the Unitarity Triangle is given by $J/2$, where

$$J = c_{12}c_{23}c_{13}^2 s_{12}s_{23}s_{13}\sin\delta \approx A^2\eta\lambda^6 \tag{2.20}$$

2.4 *CP* Violation in the *B* meson System

There are three types of CP violation that may occur in the B meson system.

- CP violation in decay. Such a process occurs in both charged and neutral decays. It occurs when the amplitude for a decay and its CP conjugate have different magnitudes.
- CP violation in mixing, which occurs when the neutral mass eigenstates cannot be chosen to be CP eigenstates.
- CP violation in the interference between decays with and without mixing. This occurs when the final state is common to both B^0 and $\overline{B^0}$ decays.

These different manifestations of CP violation are detailed below.

2.4.1 CP Violation in Hadronic B Physics

When one considers any final state f and its CP conjugate $\overline{f}$, accessible via the decay amplitudes A_f and $\overline{A}_{\overline{f}}$ representing $B \to f$ and $\overline{B} \to \overline{f}$ respectively then the parameter

$$\left|\frac{\overline{A}_{\overline{f}}}{A_f}\right| \neq 1 \Rightarrow \text{CP Violation} \tag{2.21}$$

gives evidence for direct CP violation in decay as it is independent of phase convention. This is provided we have interference between two different phases. Consider the complex parameters that appear in a Lagrangian term that contributes to the amplitude. It will appear in its complex conjugate form in the CP conjugate amplitude, hence appearing with opposite signs for A_f and $\overline{A}_{\overline{f}}$. We associate the phase with the CKM matrix. And it is therefore given the name "weak phase" and is convention dependent. Now we consider a second phase which can occur in both scattering or decay amplitudes. Such a phase does not violate CP, hence they appear in both A_f and $\overline{A}_{\overline{f}}$ with the same sign. The origin of such a phase is the possible contribution from intermediate states in decay processes. As the dominant re-scattering is due to strong interactions we assign the name “strong phase”.

We can then write the full amplitude with each contributing factor as:

$$A_f = \sum_i A_i e^{i(\delta_i + \phi)} \qquad \overline{A}_{\overline{f}} = \sum_i A_i e^{i(\delta_i - \phi)} \tag{2.22}$$

where A_i is the magnitude, $e^{i\phi}$ is the weak phase term and $e^{i\delta}$ is the strong phase term. So the convention independent quantity is then

$$\left| \frac{\overline{A}_{\overline{f}}}{A_f} \right| = \left| \frac{\sum_i A_i e^{i(\delta_i - \phi)}}{\sum_i A_i e^{i(\delta_i + \phi)}} \right| \tag{2.23}$$

This is called Direct CP Violation. CP violation of this type cannot occur unless at least the two terms that have different weak phases acquire different strong phases, i.e. there must be at least two different strong and weak phases present for the same transition $B \to f$.

If we consider the rates,

$$|A_f|^2 = |A_1 e^{i(\delta_1 + \phi_1)} + A_2 e^{i(\delta_2 + \phi_2)}|^2 \tag{2.24}$$

$$|\overline{A}_{\overline{f}}|^2 = |A_1 e^{i(\delta_1 - \phi_1)} + A_2 e^{i(\delta_2 - \phi_2)}|^2 \tag{2.25}$$

then the asymmetry is given by

$$a_f = \frac{|A_f|^2 - |\overline{A}_{\overline{f}}|^2}{|A_f|^2 + |\overline{A}_{\overline{f}}|^2} \tag{2.26}$$

$$= \frac{-2A_1A_2 \sin(\phi_1 - \phi_2)\sin(\delta_1 - \delta_2)}{A_1^2 + A_2^2 + 2A_1A_2\cos(\phi_1 - \phi_2)\cos(\delta_1 - \delta_2)} \tag{2.27}$$

Any CP asymmetries in charged B decays must be due to direct CP violation as there is no mixing.

$$a_f = \frac{\Gamma(B^+ \to f) - \Gamma(B^- \to \overline{f})}{\Gamma(B^+ \to f) + \Gamma(B^- \to \overline{f})} \tag{2.28}$$

Direct CP violation in decays can also occur in neutral B meson decays. However there is as yet no unambiguous evidence as there is interference from the two other types of CP violation processes.

2.4.2 *CP* Violation in Mixing

Mixing can occur between any two neutral pseudo-scalar mesons which contain opposite flavour content. This applies to any of the following; K^0, D^0, B^0, and B^0_s. Such states are considered stable with respect to strong and electromagnetic decay. This leaves the weak decay. Such a decay can be flavour violating. Hence our two general pseudo-scalar mesons can occur through second order weak interactions.

An arbitrary linear combination of the neutral B meson flavour eigenstates, $a|B^0\rangle + b|\overline{B}^0\rangle$ is governed by a time-dependent Schrődinger equation:

$$i\hbar\frac{d}{dt}\begin{pmatrix} a \\ b \end{pmatrix} = H\begin{pmatrix} a \\ b \end{pmatrix} = (M - \frac{i}{2}\Gamma)\begin{pmatrix} a \\ b \end{pmatrix} \tag{2.29}$$

where M and Γ are 2×2 Hermitian matrices. M comes from the box diagram and Γ from the decays. Diagonalization of this equation is required to obtain the mass eigenstates. imposing CPT invariance then guarantees that $H_{11} = H_{22}$ and H_{12} and H_{21} are the transitional amplitudes between B^0 and $\overline{B}^0$. If these transitional amplitudes are zero then no mixing is observed. The mass eigenstates are called B_L and B_H, light and heavy, and are linear combinations of the flavour eigenstates. These are represented as:

$$|B_L\rangle = p|B^0\rangle + q|\overline{B}^0\rangle \tag{2.30}$$

$$|B_H\rangle = p|B^0\rangle - q|\overline{B}^0\rangle \tag{2.31}$$

Hence if B_L and B_H are CP eigenstates then $|p| = |q|$. If $|\frac{p}{q}| \neq 1$ we have CP violation. This is often referred to as indirect CP Violation. It arises because the mass eigenstates are different from the CP eigenstates. For the neutral B meson an asymmetry effect would be, in theory, observed in semi-leptonic decays.

$$a_{SL} = \frac{\Gamma(\overline{B}^0(t) \to l^+\overline{v}\mathrm{X}) - \Gamma(B^0(t) \to l^-v\mathrm{X})}{\Gamma(\overline{B}^0(t) \to l^+\overline{v}\mathrm{X}) + \Gamma(B^0(t) \to l^-v\mathrm{X})} \tag{2.32}$$

2.4.3 CP Violation in Interference Between Mixing and Decay

The second type of indirect CP violation is due to the interference between decays with and without mixing, where neutral B decays to final states are accessible by both B^0 and $\overline{B}^0$.

$$B^0_{Pure} \rightarrow f, \tag{2.33}$$

$$B^0_{Pure} \rightarrow \overline{B}^0_{Pure} \rightarrow f, \tag{2.34}$$

where we have started with an initially pure B^0 ($\overline{B}^0$) state. The decay rates are obtained by squaring the modulus of each amplitude for these processes.

$$R_{B^0_{Pure}} = |\langle f|H|B^0_{Pure}\rangle|^2 \tag{2.35}$$

$$= e^{-\Gamma t}|A|^2\{1 + |\lambda_f|^2 + (1 + |\lambda_f|^2)\cos(\Delta m_B t) - 2\mathrm{Im}\lambda_f \sin(\Delta m_B t)\} \tag{2.36}$$

$$R_{\overline{B}^0_{Pure}} = |\langle f|H|\overline{B}^0_{Pure}\rangle|^2 \tag{2.37}$$

$$= e^{-\Gamma t}|A|^2\{1 + |\lambda_f|^2 - (1 - |\lambda_f|^2)\cos(\Delta m_B t) + 2\mathrm{Im}\lambda_f \sin(\Delta m_B t)\} \tag{2.38}$$

where $\Delta m_B = m_L - m_H$, $\Gamma = \frac{\Gamma_H + \Gamma L}{2}$ and:

$$\lambda_f \equiv \frac{q}{p}\frac{\overline{A}_f}{A_f} = \left|\frac{q}{p}\right|\left|\frac{\overline{A}_{\overline{f}}}{A_f}\right| e^{i\Delta\phi} \tag{2.39}$$

and $\Delta\phi = \phi_M - \phi_D$ is the relative phase between mixing and decay. Therefore the time-dependent asymmetry rate is,

$$a_f(t) = \frac{R_{B^0_{Pure}} - R_{\overline{B}^0_{Pure}}}{R_{B^0_{Pure}} + R_{\overline{B}^0_{Pure}}} \tag{2.40}$$

so,

$$a_f(t) = \frac{1 - |\lambda_f|^2}{1 + |\lambda_f|^2}\cos(\Delta m_B t) + \frac{-2\mathrm{Im}\lambda_f}{1 + |\lambda_f|^2}\sin(\Delta m_B t) \tag{2.41}$$

CP is conserved if $|q/p| = 1$, $|\overline{A}_{\overline{f}}/A_f| = 1$ and there is no relative phase between q/p and $\overline{A}_{\overline{f}}/A_f$, i.e. λ must have no phase. Therefore

$$\lambda \neq \pm 1 \Rightarrow \text{implies CP violation} \tag{2.42}$$

2.5 Charmless Hadronic B Decays

Rare charmless hadronic B decays play an important role within the BaBar experiment. These very low branching fraction decays are interesting for a number of reasons. As the tree diagram amplitudes within these modes are suppressed, they are roughly the same order of magnitude as the penguin amplitudes. Penguins involve internal decays to weak charged bosons and the emission of a neutral boson or gluon before re absorbing the charged weak boson. This is expected in some decays to produce significant direct CP violation which has not yet been significantly observed in B decays. This represents fertile ground to study these loop processes. It is also possible to measure all three angles of the unitarity triangle through charmless hadronic B decays.

Angle α

Any mode involving a $b \rightarrow du\overline{u}$ transition is a possible source of measuring α [3]. Primarily two and three pion final states are used, however some of the modes in this report can be used for this purpose.

Angle β

Overall this is the easiest angle to measure with BaBar already producing measurements. While the largest contribution to the measurement of this angle comes from $B \rightarrow J/\Psi K^0_S$, it can also be measured through decays where either penguins dominate or are the only possible decay method. These are $b \rightarrow s\overline{s}s$ or $d\overline{d}s$ decays.

Angle γ

This is the most difficult angle to measure. However it is possible by comparing $B \rightarrow \pi\pi$ and $B \rightarrow K\pi$ decays [3].

The decay modes investigated in this report are shown in figures 2.2, 2.3 and 2.4. As can be seen they cover a wide range of decays including $b \to u$ and $b \to s$ which can be used in determining angles α and β respectively. Also the Unitarity Triangle side R_b can be obtained. However before these can be measured with the modes covered in this report a selection method must first be obtained.

2.6 New Physics

BaBar is set to gather large amounts of data over its lifetime. This will provide the means to probe the Standard Model to an unprecedented level of precision. Such precision measurements of rare modes can provide an insight into high-energy scales via the effects of new interactions. New physics can manifest itself in a number of ways within the B meson system. The angles of the Unitarity Triangle could result in $\alpha + \beta + \gamma \neq \pi$. Large asymmetries may be observed where there should be none, or very little. Also rare decay modes, such as the ones covered in this report, may be larger than expected. All these potential deviations from the Standard Model may be due to new interactions at the tree level or from virtual effects in loop physics. The decays presented in this report may be used in future studies to assist in these searches for new physics.

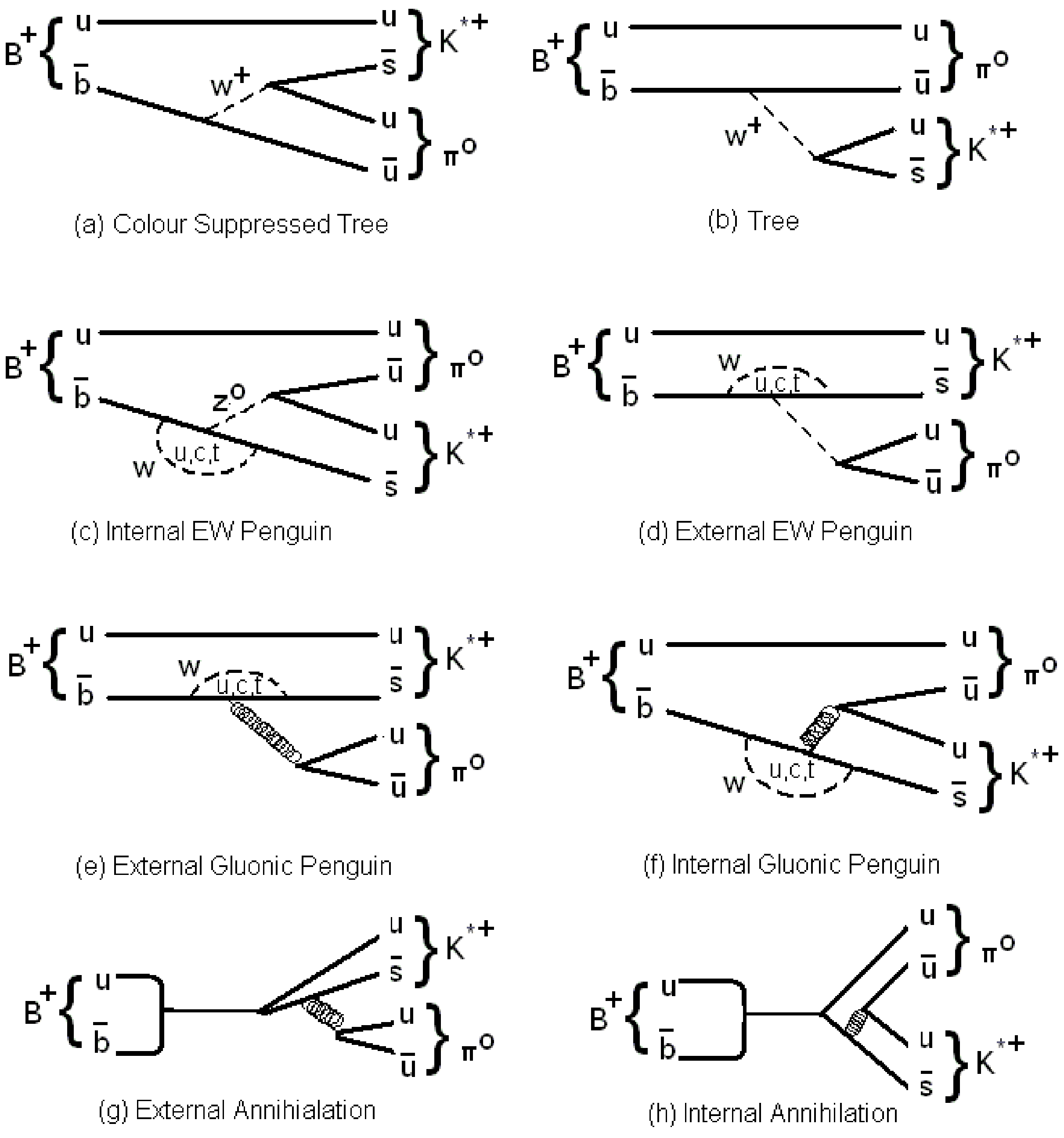

(a) Colour Suppressed Tree

(b) Tree

(c) Internal EW Penguin

(d) External EW Penguin

(e) External Gluonic Penguin

(f) Internal Gluonic Penguin

(g) External Annihialation

(h) Internal Annihilation

Figure 2.2: All possible decays for $B^+ \to K^{*+}\pi^0$. (a) and (b) show the colour suppressed tree and tree processes. (c) and (d) show the internal and external electroweak penguin decay process. (e) and (f) show the internal and external gluonic penguin process. (g) and (h) show the external and internal annihilation process.

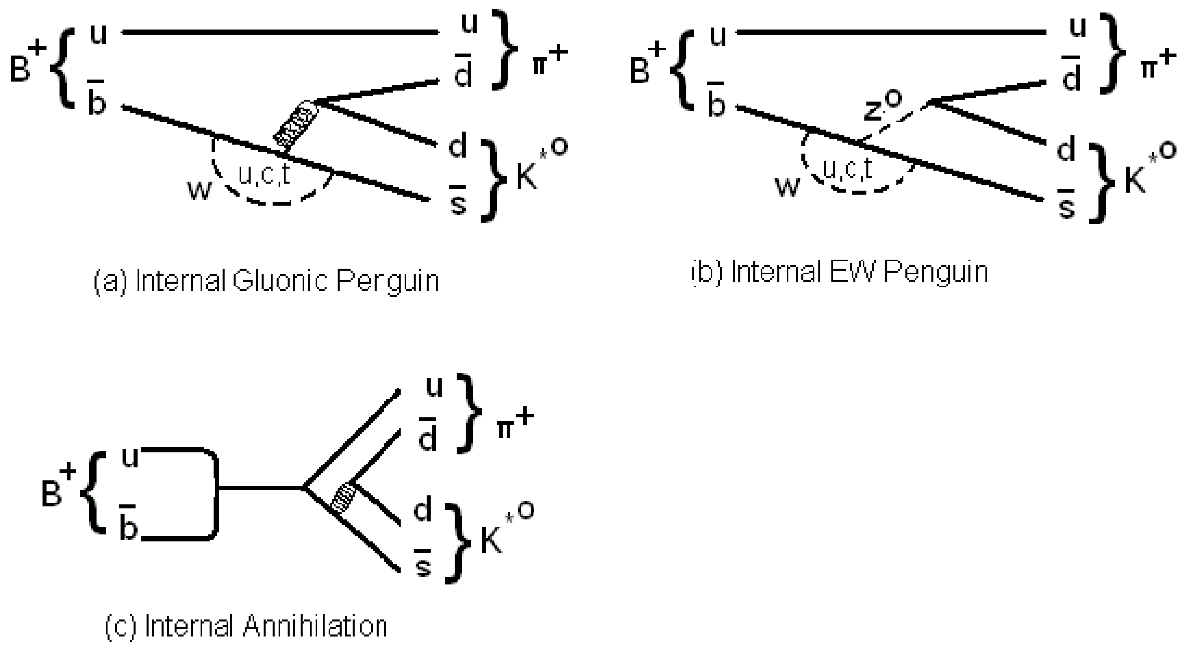

Figure 2.3: All possible decays for $B^+ \to K^{*0}\pi^+$: (a) shows the internal gluonic penguin, (b) shows the internal electroweak penguin, (c) shows the internal annihilation.

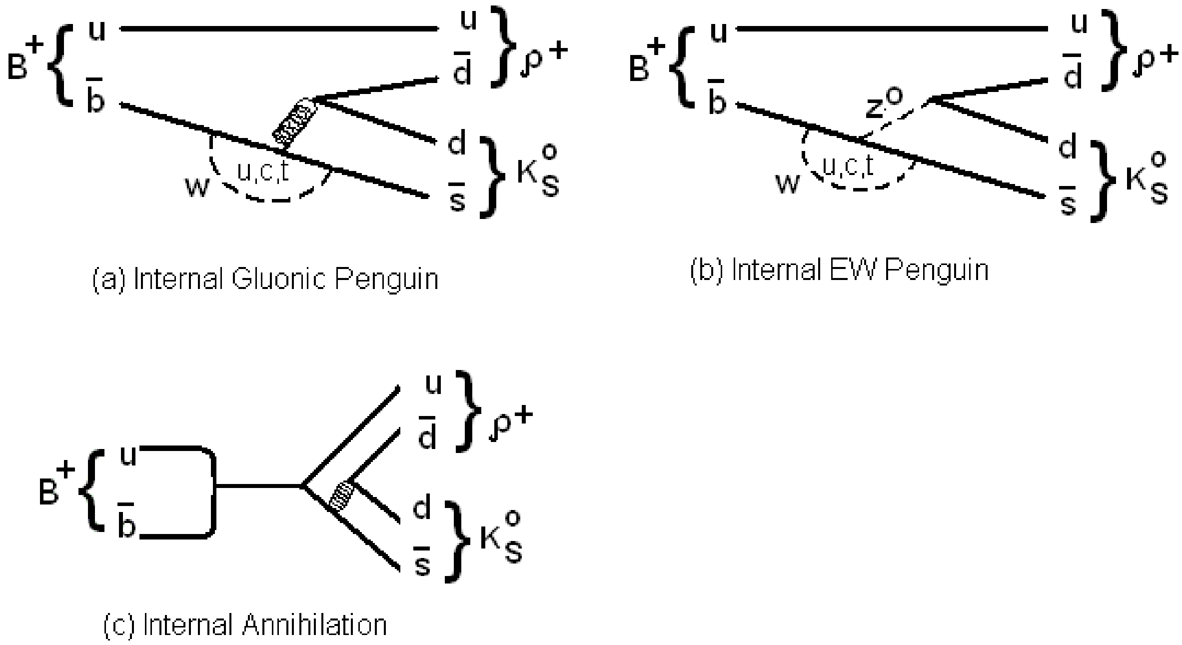

Figure 2.4: All possible decays for $B^+ \to K^0_S\rho^+$: (a) shows the internal gluonic penguin, (b) shows the internal electroweak penguin, (c) shows the internal annihilation.

Chapter 3

The BaBar Experiment

3.1 Introduction

The principle aim of the BaBar experiment is the systematic study of CP asymmetries in the B meson system. In addition to this a number of rare B meson decays, once carefully studied, in conjunction with sensitive measurements of the CKM matrix element V_{ub} can be used to further constrain fundamental parameters of the Standard Model.

Such studies may only require a few hundred fully reconstructed events in specific channels. However the exclusive B meson final states of interest have very small branching ratios, e.g., $\sim 10^{-4}$ to 10^{-6}, so the experiment must produce in excess of 10^7 $B^- B^+$ pairs. This requires a luminosity of a few times $10^{33}\mathrm{cm}^{-2}\mathrm{s}^{-1}$ to limit our errors to 10% level or better.

This chapter will begin with a look at B meson production through the $\Upsilon(4s)$ using the Stanford Linear Accelerator and the PEP-II collider system. It will then go on to describe the BaBar detector, how it tracks, measures and identifies particles produced in B meson decay. Finally it will explain how the BaBar triggering system functions, how BaBar measures the luminosity and how the simulated data, like that used in this report, is produced.

3.2 The Stanford Linear Accelerator and the PEP-II Storage Ring

Electron bunches are created by an electron gun. They are then accelerated to 9 GeV by the Stanford Linear Accelerator and then injected into the PEP-II high energy ring. Positron bunches are created by accelerating a bunch of electrons in the linac and colliding them with a stationary Beryllium target. These positron bunches are then accelerated by the linac and injected into the PEP-II low energy ring. This PEP-II system is situated at the end of the two mile long Stanford Linear Accelerator.

The PEP-II e^+e^- collider operates at the $\Upsilon(4s)$ resonance in an asymmetric mode. This asymmetry is achieved by injecting 9 GeV electrons and 3.1 GeV positrons into the high energy ring (HER) and low energy ring (LER) respectively and colliding them. A diagram of the PEP-II rings is shown in Figure 3.1.

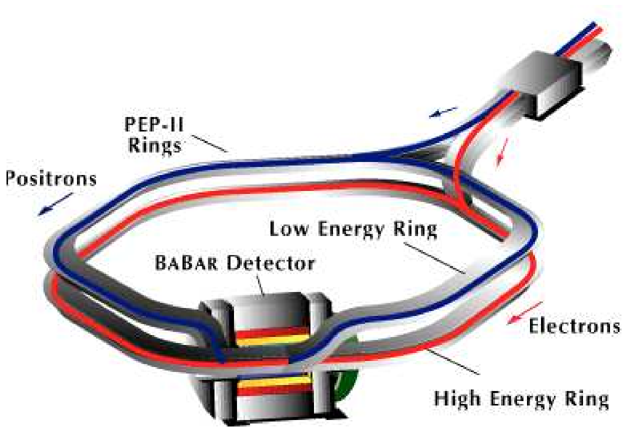

Figure 3.1: A diagram of the PEP-II storage ring system, the coloured rings represent the high and low energy electrons and positrons respectively.

3.3 Why the $\Upsilon(4s)$

Operating at the $\Upsilon(4s)$ resonance has several advantages. It decays to $B\overline{B}$ 100% of the time. In an asymmetric configuration, such as that produced by PEP-II, the resultant B meson has significant momentum in the laboratory frame. This enables the B mesons flight time to be inferred from their measured decay lengths. Also running at the $\Upsilon(4s)$ energy allows the energies of the B mesons to be known, which is utilized to fight backgrounds. Running at the $\Upsilon(4s)$ energy level aids in background studies. Running below the $\Upsilon(4s)$ ($\approx$ 40 MeV) produces "offpeak" data that contains no B mesons, this can be utilized in studying non-$B\overline{B}$ backgrounds. This technique is not used in this report due to low statistics.

3.4 The BaBar Detector

In order to achieve the physics set out by the aims of the experiment it needs to be able to measure three vital quantities: The exclusive final state needs to be fully reconstructed; the flavour of the decaying particle needs to be tagged and the proper time of the B^0 decay with respect to its production must be measured.

The BaBar detector was designed to provide all the above features. A schematic of the detector is shown in Figure 3.2. A detailed description of the BaBar detector can be found in [12]. The BaBar detector is divided into five sub-detectors and a magnetic coil. The sub-detectors are listed below in order starting nearest the beam-pipe:

- A Silicon Vertex Tracker (SVT); this provides positional information and tracking for low energy charged particles.
- A Drift Chamber (DCH); this is filled with a helium based gas and provides the main momentum measurements for charged particles. It also provides particle identification through dE/dx information.

- A Detector of Internally Reflected Cherenkov light (DIRC); this was designed for charged hadron particle identification, especially kaons and pions at higher momentum.
- A Caesium Iodide Electromagnetic Calorimeter (EMC); this provides neutral particle identification as well as good electron identification. Due to the asymmetry of the experiment it contains only one end cap, as well as the main barrel.
- A superconducting coil; this provides a 1.5T solenoid magnetic field.
- An Instrumented Flux Return (IFR); this is used for muon and neutral particle identification.

3.4.1 The BaBar co-ordinate system

The Babar co-ordinate system is defined as a right handed system with the z-axis corresponding to the Drift Chamber principal axis in the direction of the high energy electron beam. The x-axis points horizontally away from the centre of the PEP-II ring. The y-axis points vertically upward. The polar (θ) and azimuthal (ϕ) angles are defined as in the standard spherical polar co-ordinate system.

3.4.2 The Silicon Vertex Tracker

The primary task of the silicon vertex tracker is to reconstruct the decay vertices of the initial B mesons. This enables the determination of the time between the decays, which is important in the determination of the time dependent CP asymmetry. For particles with a transverse momentum lower than 100 MeV/c the silicon vertex tracker provides the complete tracking information. Figure 3.3 shows a dissected view of the silicon vertex tracker.

The silicon vertex tracker consists of five concentric cylindrical layers of double sided silicon detectors. The inner three layers consist of six detector modules arranged

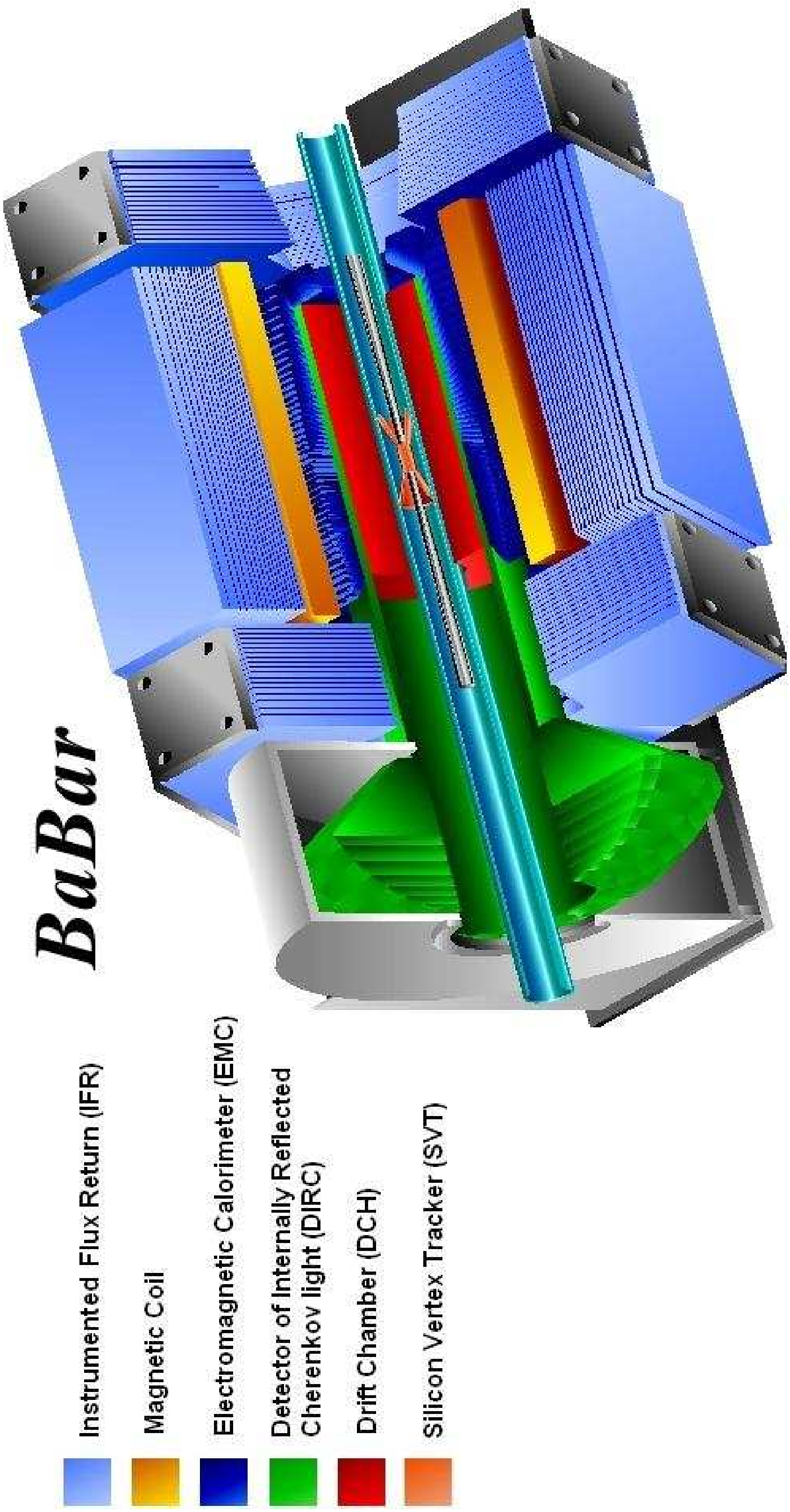

Figure 3.2: A schematic of the BaBar detector.

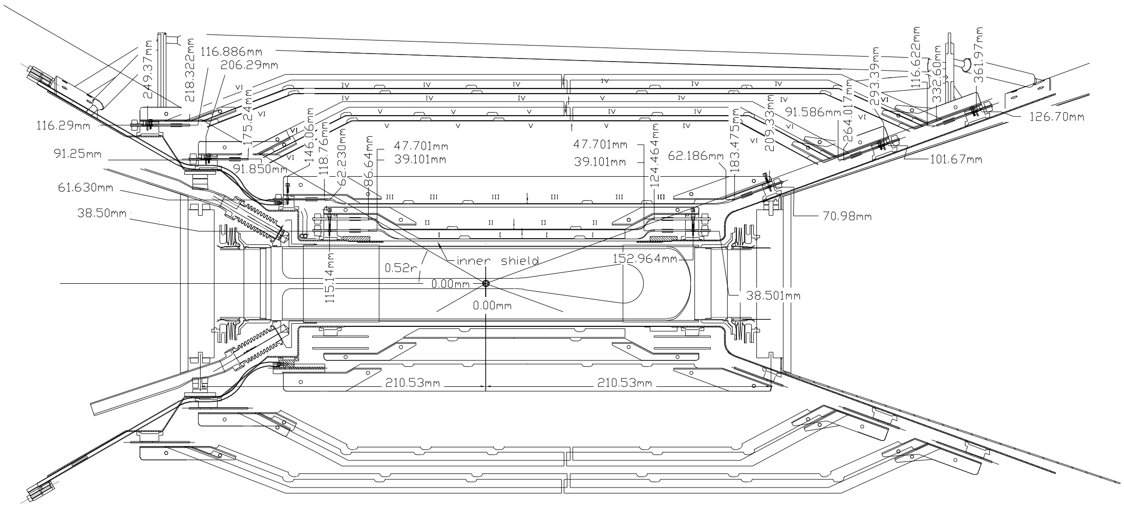

Figure 3.3: A schematic of the Silicon Vertex Tracker.

in a traditional barrel formation. The outer two layers consist of 16 and 18 detector modules respectively. They employ a new arch structure that is designed to increase the solid angle cover. The outer layer modules are further divided into "a" and "b" modules. These differ in size enabling an overlap structure.

The silicon vertex tracker modules are split into inner and outer sides. The inner side has strips perpendicular to the beam direction to measure the z component. The outer side has longitudinal strips that allow us to measure the ϕ co-ordinate. In total the silicon vertex tracker contains 340 silicon detectors covering an area of approximately 1m^2. It has a resolution of 25-65μm,which is an better than the 80μm required for accurate z-separation between two B vertices.

3.4.3 The Drift Chamber

The Drift Chamber is the main tracking device in the BaBar experiment. For tracks of higher than 100 MeV/c transverse momentum it is possible to obtain up to 40 spatial co-ordinate measurements per track. It is also possible to combine this information with the silicon vertex tracker to improve the spatial and momentum resolutions.

The original aim of the Drift Chamber was to achieve a spatial resolution of better than 140μm [12]. A spatial resolution of around 70μm has already been achieved. Another important role for the Drift Chamber is that of particle identification. Figure 3.4 shows the standard scatter distribution obtained from the five parameter Bethe-Bloch formula for the mean rate of ionization loss of a charged particle. Using dE/dx information it is possible to obtain a resolution of 7% for a track of 40 spatial measurements. Once the particle's momentum exceeds 1 GeV/c a resolution of $\sigma \approx 0.3\% \times P_t$ is expected. This resolution limit for low momentum tracks is due to multiple scattering in the silicon vertex tracker and drift chamber.

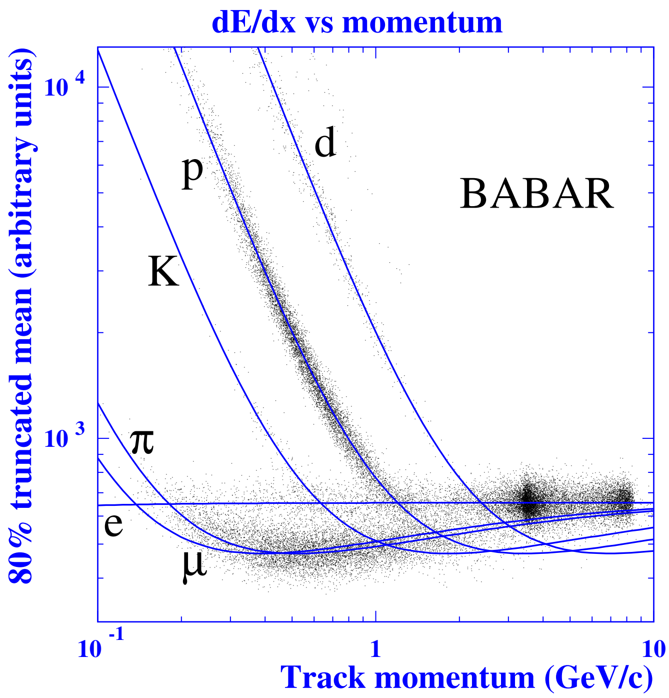

Figure 3.4: A Scatter plot of dE/dx versus momentum showing how paritcle identification can be achieved. Taken from [13]

The Drift Chamber is a 2.8m long cylinder situated asymmetrically around the interaction point as shown in Figure 3.5 (Left). To minimize multiple scattering the chamber is filled with a helium-isobutane gas mixture in a 4:1 ratio. A small amount of water vapour is also added to help prolong the life of the chamber. The sense wires are gold-plated tungsten-rhenium with a 20μm diameter. The field wires are gold-plated aluminium with diameters of 120μm and 80μm.

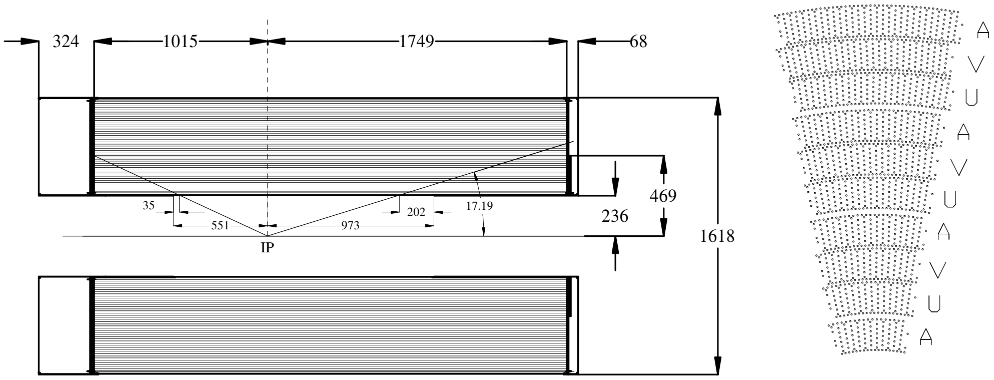

Figure 3.5: (Left) A cross-section view of the Drift Chamber. (Right) Cell layout of the superlayers.

The Drift Chamber is made up of 10 superlayers; each consisting of 4 layers of cells. The superlayers are arranged into axial(A) and stereo (U,V) in the order AUVAUVAUVA as show in Figure 3.5 (Right).

3.4.4 The Detector of Internally Reflected Cherenkov light

The detector of internally reflected Cherenkov light is an excellent particle identification tool that can achieve a kaon-pion separation over a wide momentum range. An example is the rare two-body mode $B^0 \to \pi^+\pi^-$ and $B^0 \to K^+\pi^-$, where the DIRC can separate pions from kaons up to 4 GeV/c. The DIRC design principle is shown in figure 3.6.

The DIRC consists of 144 synthetic quartz bars arranged in a 12-sided polygon barrel outside the Drift Chamber. The bars are 17mm thick, 35mm wide and 4.9m long. There are approximately 11,000 photomultiplier tubes lining the stand-off box. The stand-off box itself contains 6000 litres of purified water, this being chosen for its refractive index, which is close to that of the quartz bar. This minimizes total internal reflection at the quartz-water boundary. The DIRC takes up just 8cm of radial space, however it only covers approximately 83% of the polar angle in the centre of mass frame.

As a particle traverses the bar with a velocity $\beta \geq \frac{1}{n_1}$, where n_1 is the refractive index of the quartz, it radiates a Cherenkov cone of light at the angle $\theta_c = \frac{1}{\beta n}$. Due to the high refractive index of the quartz bar some of the produced Cherenkov photons undergo total internal reflection successively down the bar to the backward end. Any forward going photons are reflected back by a mirror positioned at the forward end. The angle θ_c is preserved throughout. When the light reaches the end of the bar it expands into a large expanse of high quality purified water producing a Cherenkov ring image. This image is the read out by a close-packed array of photomultiplier tubes arranged on a toroidal surface. From the radius of the Cherenkov ring θ_c is calculated. This provides the particle velocity, which when combined with the particle momentum yields a particle mass.

3.4.5 The Electromagnetic Calorimeter

Many of the decays needed to measure *CP* violation parameters contain one or more π^0's in the final state. The initial design constraint placed on the electromagnetic calorimeter was to reconstruct photons with energies above 20MeV with good efficiency, which could then be used to construct π^0's. The electromagnetic calorimeter consists of 5670 CsI(Tl) crystals arranged in a barrel with a forward end-cap. Due to the asymmetry of the beams only one end-cap is required. Figure 3.7 shows a cross sectional view of the Electromagnetic Calorimeter. It has full coverage in the azimuthal angle and covers approximately 90% of the solid angle in the centre of mass frame.

The barrel is made up of 48 rows in θ, each row containing 120 crystals in ϕ. The crystals are grouped into modules of 7 crystals in θ and ϕ respectively. The end-cap is arranged as 8 rings in θ, the ninth ring (surrounding the beam) contains lead shielding blocks to reduce the beam background effect on the end-cap crystals. Again the crystals are grouped into modules, here they are split into 20 modules each

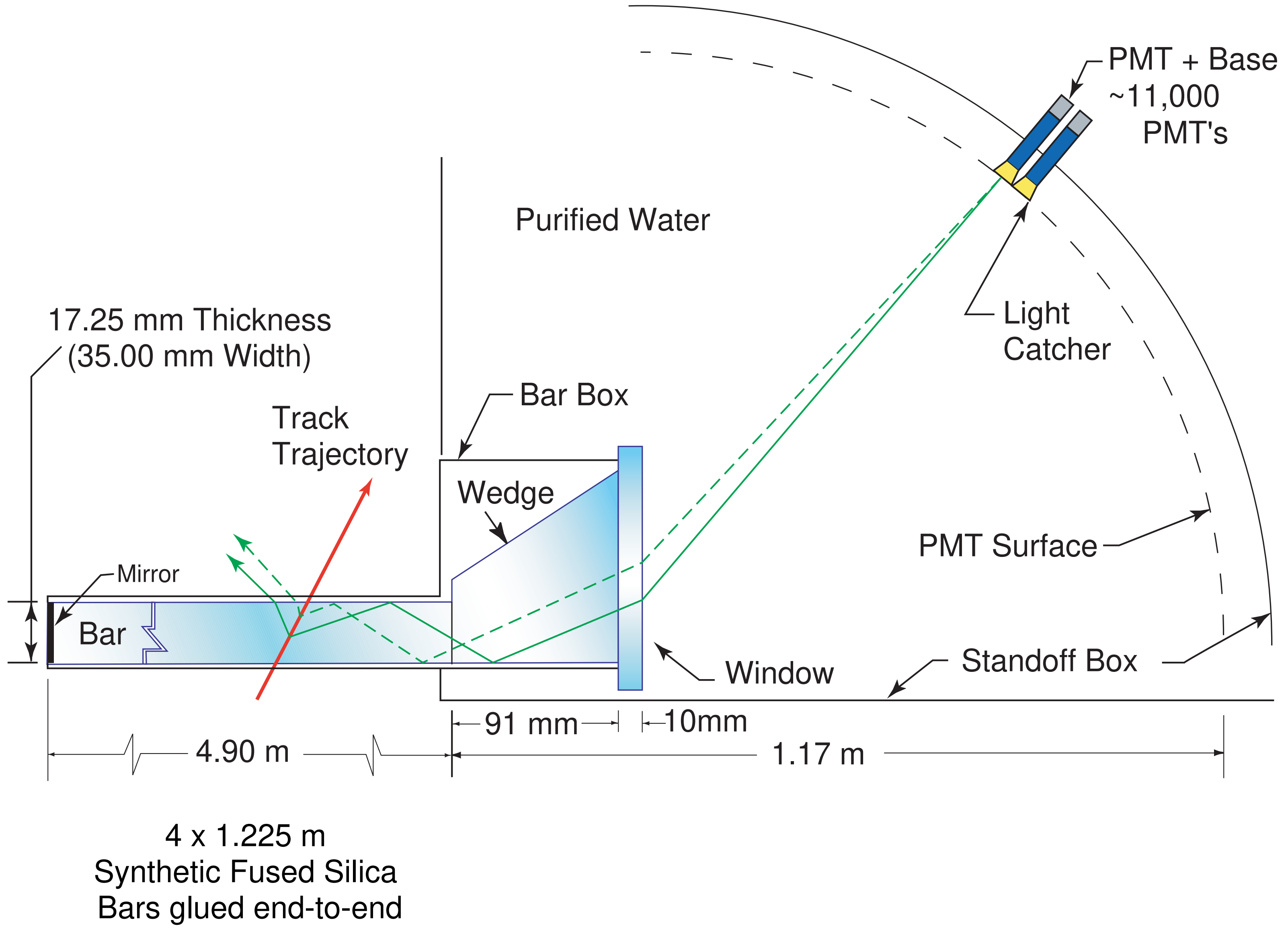

Figure 3.6: Principle of the Detector of Internally Reflected light.

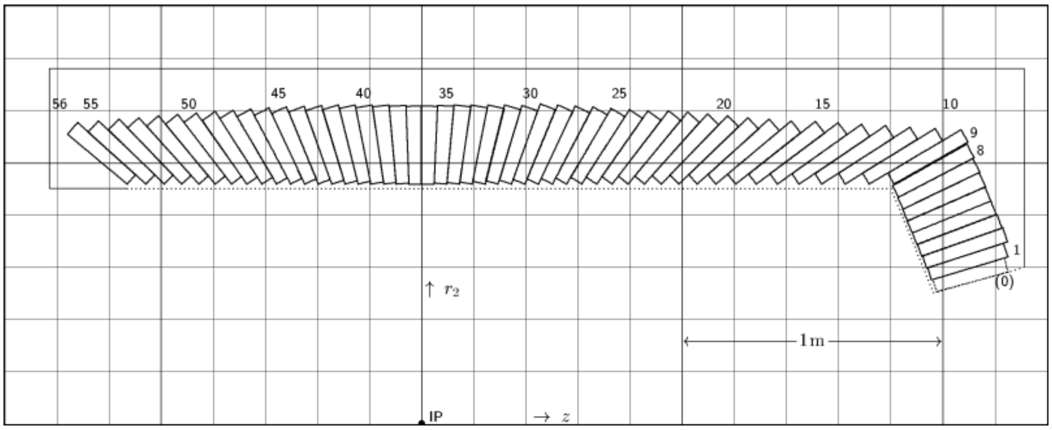

Figure 3.7: A diagram showing the cross section view of the Electromagnetic Calorimeter barrel and end-cap

containing 41 crystals.

A particle showering in the calorimeter will generally deposit energy over several crystals. The individual crystals are then grouped into 'clusters', which are further separated into 'bumps'. A 'bump' is a local maximum within a cluster that provides the resolution of particles that shower close together. A correction factor must be applied to the bump energy to account for energy lost through showering in material in front of the calorimeter.

3.4.6 The Instrumented Flux Return

The Instrumented Flux Return was designed for neutral hadronic and muon identification. Again many of the important CP modes under investigation contain muons in the final state, e.g. $B \rightarrow XJ/\psi$ where $J/\psi \rightarrow e^+e^-$ or $\mu^+\mu^-$. Muons are also used in tagging the flavour of the non-CP B meson through its semi-leptonic decay. The IFR is constructed of iron and serves as the flux return for the 1.5T magnetic field. It is instrumented with Resistive Plate Counters (RPC's). These RPC's are segmented and form a hexagonal barrel around the interaction point. There are also two endcaps, unlike the electromagnetic calorimeter. The barrel itself is segmented into 19 layers, and 18 layers for the end-caps. A diagram of this can be seen in Figure 3.8

Monte Carlo studies conducted to optimize both muon and neutral hadron identification resulted in a novel design feature. The thickness of each successive layer increases from 2cm at the inner radius to 10cm at the outer radius.

3.4.7 The Trigger

The BaBar trigger is required to provide high efficiency for selecting B physics events. The BaBar trigger is implemented in two levels, a level 1 hardware trigger (L1) and a level 3 software trigger (L3). It was concluded that no level 2 trigger is necessary under current background and luminosity conditions at BaBar.

The level 1 trigger, consists of four subsystems: the charged particle trigger (the Drift Chamber Trigger, or DCT), the neutral particle trigger (the Electromagnetic Calorimeter Trigger, or EMT), the cosmic trigger (the Instrumented Flux Return (IFR) Trigger, or IFT) and the Global Level Trigger (GLT).

The Trigger operates in the following way, the DCT and EMT receive information from the Drift Chamber and Calorimeter detectors, process it, and send condensed data to the Global Trigger. The GLT attempts to match the angular locations of calorimeter towers and drift chamber tracks, it then generates Level 1 triggers and sends them on to the Fast Control and Timing system (FCTS), based on the results of the processing. It must generate these output Level 1 triggers with a rate of less than 2 kHz, though the incoming rate is upwards of millions of events per second. The GLT also uses the IFT information to veto cosmic ray events. The level 3 trigger then uses the online event processing (OEP) to select events for data storage at a rate of 100 Hz.

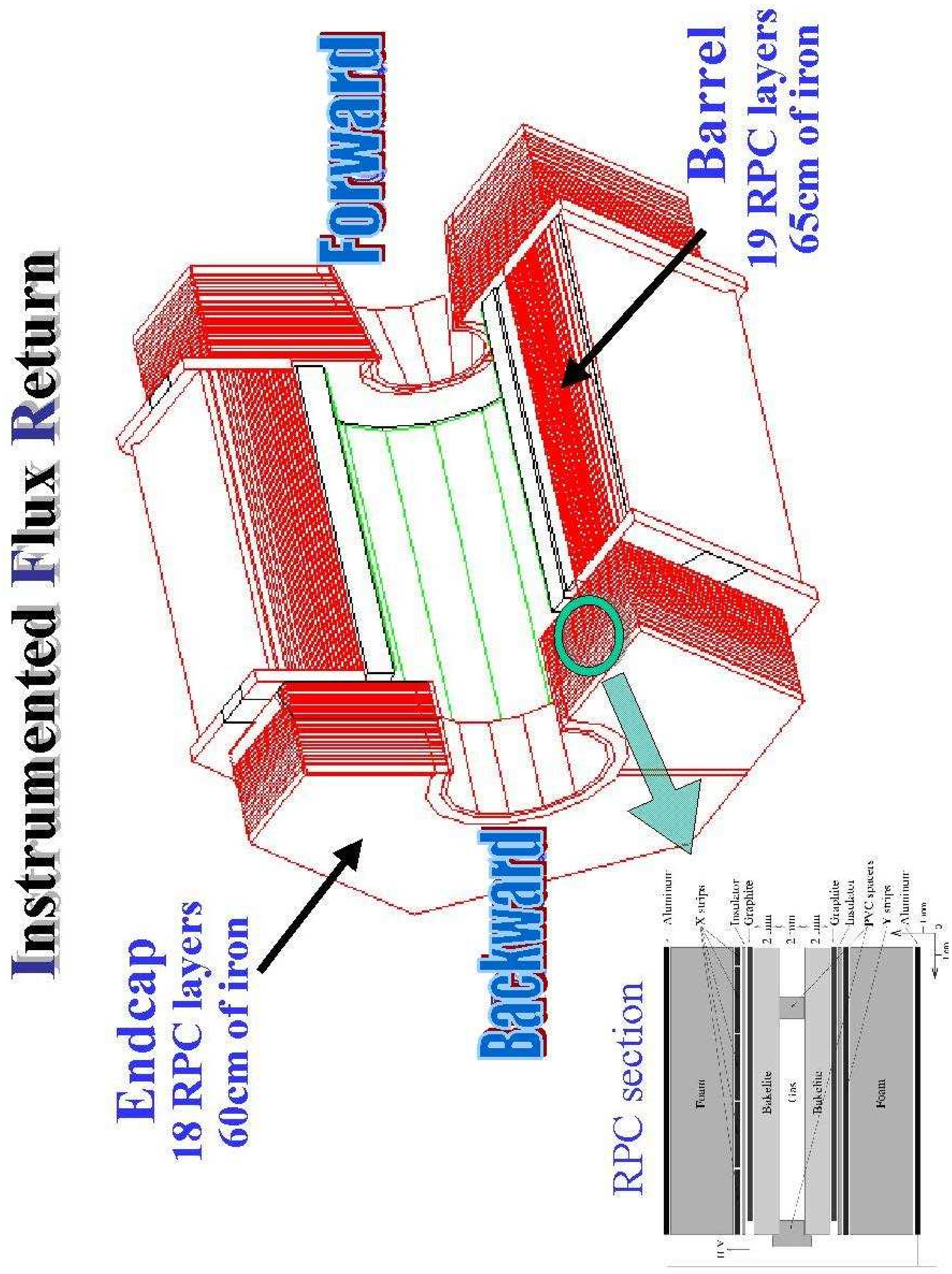

Figure 3.8: Diagram showing the barrel and end-caps of the Instrumented Flux Return with a Resistive Plate Counter cross section

3.5 Luminosity Measurements at BaBar

The method for determining luminosity L in the Babar e^+e^- collider is through the relationship $L= N/\sigma_{vis}$, where N is the number of events observed for a reference reaction and $\sigma_{vis} = \epsilon \times \sigma_{th}$ is the visible cross section for this reaction. σ_{th} is the theoretically expected cross section and ϵ is the efficiency for identifying these events. ϵ is calculated using full detector simulation. This method therefore must use reactions that have high and well known theoretical cross sections and the simulation of the detector must be accurate and easy to validate using real data.

In BaBar the luminosity is measured through the rates of $e^+e^- \to e^+e^-(\gamma)$ and $e^+e^- \to \mu^+\mu^-(\gamma)$ events. Full details can be found in [14].

3.6 BaBar Simulation

The BaBar simulation reproduces in detail the generation of events at the interaction point, the propagation of the resulting particles through the detector and the response of the detector to these particles. Detector response quantities are then used to construct candidate events which can be analyzed as if they were real data. A simplified simulation architecture can be seen in figure 3.9.

There are four main stages in producing a simulated event. The first is generation where the physics of the e^+e^- collision is performed by one of several event generators. The generators provide a set of four-vectors which represent the final state of the collision near the e^+e^- interaction point. The second is particle transport and hit scoring. Here the four-vectors from the generator stage are transported through the simulated detector, where energy loss, production of secondaries, multiple scattering and decay can occur. As these particles pass through regions of the detector the energy, charge and angular information is used to calculate positions and idealized energy deposits in the detector. Thirdly there is Detector Response and Background Mixing. Here data is retrieved from the database and transformed into simulates realistic signals

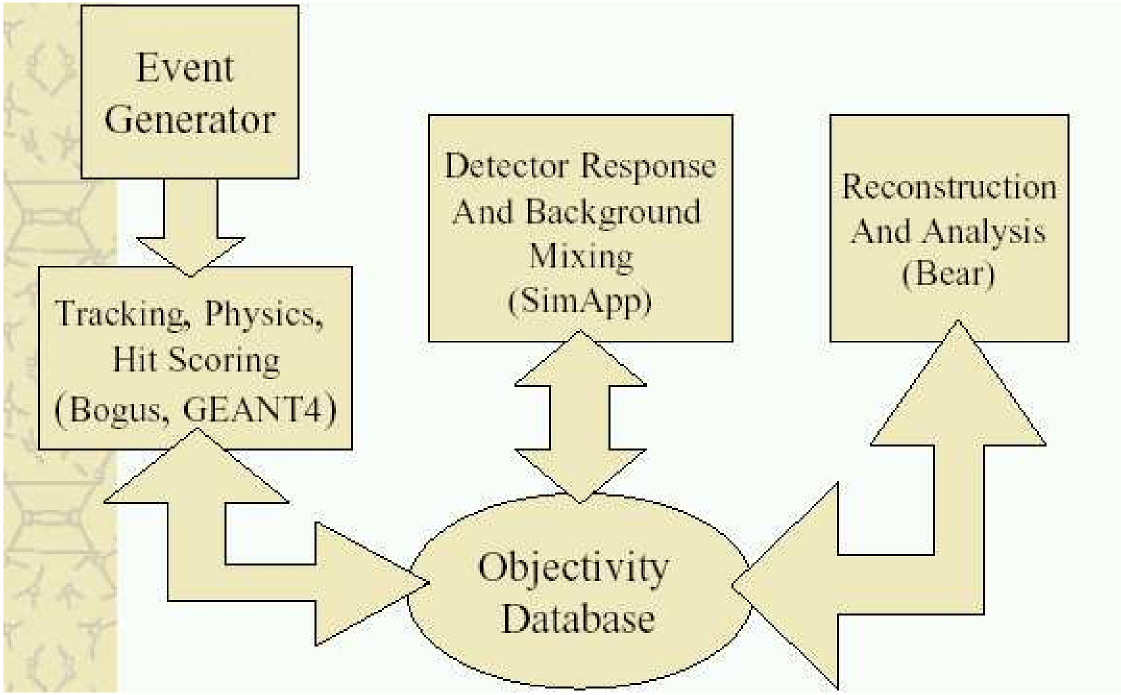

Figure 3.9: Monte Carlo simulation architecture as depicted by the BaBar simulation team

that mimic those collected from the detector electronics. Real background events, stored in the database, may be mixed in with the simulated event to more closely reproduce signal data. The final stage is reconstruction in which simulated raw data is combined into candidate events consisting of particle tracks, energy clusters, and probable particle identifications.

Chapter 4

Analysis Techniques For $B^+ \to K_S^0 \pi^+ \pi^0$

The aim of the analyses contained in this report is a measurement of, or upper limit on, the branching fractions of the rare three body final-state decays $B^+ \to \pi^+ K^{*0}$, $B^+ \to \pi^0 K^{*+}$ and $B^+ \to \rho^+ K_s^0$ where $K^{*0} \to \pi^0 K_s^0$, $K^{*+} \to \pi^+ K_s^0$ and $\rho^+ \to \pi^+ \pi^0$ respectively. These analyses are cut based counting analyses. Branching fractions and upper limits of the resonance modes have previously been presented by the BaBar [15], BELLE [16] and CLEO [17] collaborations. Table 4.1 shows the corresponding values at the time this analysis was conducted.

Decay Mode	BF or UL (90% CL)
$B^+ \to \pi^+ K^{*0}$	$16.7^{+3.7+2.1+3.0}_{-3.4-2.1-5.9} \times 10^{-6}$
$B^+ \to \pi^0 K^{*+}$	$< 99 \times 10^{-6}$
$B^+ \to \rho^+ K_S^0$	$< 48 \times 10^{-6}$

Table 4.1: The Branching Fraction of $B^+ \to \pi^+ K^{*0}$ comes from the BELLE collaboration [16], $B^+ \to \pi^0 K^{*+}$ and $B^+ \to \rho^+ K_S^0$ were presented by the CLEO collaboration. [8]

There exist many areas of interest within these decay channels, as discussed in chapter 2. This chapter presents an overview of the analysis techniques used. While a commonality exists between the modes, specific details, unique to each mode, will be covered in Chapter 5. Results of the respective analyses will be given in Chapter 5.

4.1 Analysis Overview

The charged B candidates are constructed from a charged track a π^0 candidate and a K_S^0 candidate. Selection requirements are imposed on a set of discriminating variables. The number of B candidates is then counted. An estimated number of background events passing the imposed selection criteria are subtracted from the number of observed B candidates to produce N_{sig}, the number of signal events. The branching fraction is then calculated using

$$B = \frac{N_{sig}}{N_{B\overline{B}}\varepsilon} \tag{4.1}$$

where $N_{B\overline{B}}$ is the number of $B\overline{B}$ pairs and ε is the efficiency for signal selection. ε is obtained through Monte Carlo studies. It is important to note that above equation is correct as there are two factors of two in its derivation. Two B's are produced per $B\overline{B}$ event, however half are B^+B^- events and half are $B^0\overline{B}^0$ events. Selection criteria are applied to the Monte Carlo simulated data. The selection criteria are chosen through direct comparisons between Monte Carlo data and background. Corrections are applied later for modelling discrepancies.

Selection cuts were imposed on the π^0 mass, minimum energy of the constituent photons and the photon lateral energy distribution, as detailed in section 4.5.3. We impose particle identification criteria on the charged track, which is covered in section 4.6. K_S^0 candidates were constrained via a mass cut and a lifetime significance cut, which is presented in section 4.5.4. Resonances were selected with additional cuts on their mass and decay angle, as detailed in section 4.5.5. An additional two event shape variables were used for background rejection, featured in section 4.5.6. There are also constraints on two kinematic variables ΔE and M_{ES}, which will be discussed in section 4.3.

The analyses described are conducted "blind", (see section 4.4). This means the data within the defined signal region are neither plotted nor counted until the method and selection criteria have been frozen. This analysis technique involves first characterising the background, which is fully covered in section 4.8. This is achieved by selecting regions in the ΔE-M_{ES} plane near the signal region. The number of background events expected in the signal region then becomes RN_{GSB}. R is a ratio between a defined signal region and background region that takes into account shape and size. N_{GSB} is the number of events observed in the defined background region. The selection criteria are chosen to optimise $S/\sqrt{S+B}$. This is discussed in section 4.9. B represents the number of background events expected in the signal region. S is the signal estimated from the Monte Carlo efficiency studies from assumed branching fractions. This analysis then counts the number of events in the defined signal region. Caution must be taken however as many events have multiple candidates. It therefore becomes necessary to select a best candidate based upon a constructed candidate χ^2, which is covered in section 4.7.

4.2 Data Sample

The data sample used in these analyses includes 19.4fb^{-1} of $\Upsilon(4S)$ data recorded in 1999-2000, which corresponds to 22.1×10^6 $B\overline{B}$ events. For each mode under investigation 6000 simulated events of mode specific B decays were produced to determine signal distributions and calculate signal efficiencies. Monte Carlo continuum and $B\overline{B}$ and B^+B^- events were used to characterise background events. The generation of this simulated data has been discussed in section 3.6. An important note here is that we use Monte Carlo simulation data to define the expected signal distributions, where as data is used to get background distributions as signal areas are excluded.

4.3 Kinematic Constraints: ΔE and M_{ES}

As the $\Upsilon(4S)$ decays to B mesons it provides powerful kinematic constraints that are dictated by the initial beam energies and can be utilized to discriminate between signal and background. Two kinematic constraints that are used in this report, and to a larger extent by BaBar [22] [23], come from the B meson reconstruction and are: the difference between the reconstructed and the expected (according to beam-energy) B meson energy, ΔE, and the beam energy substituted mass, M_{ES}.

$$\Delta E = E_B^* - \frac{\sqrt{s}}{2} \tag{4.2}$$

$$M_{ES} = \sqrt{\left(\frac{\frac{1}{2}s + P_{e^+e^-}.P_B}{E_{e^+e^-}}\right)^2 - P_B^2} \tag{4.3}$$

Here E and P are the energy and magnitude of momentum. The asterisk superscript denotes a lab frame value, subscripts e^+e^- denote the beam energies, B the B meson and s the beam energy. For signal ΔE is peaked at zero but is dependent on the mass hypotheses assigned to the B daughter tracks. M_{ES} is independent of the masses of the B meson daughters, so is much more accurate, and is peaked at the B mass, 5.279 GeV/c^2.

Since our analyses are “blind”, cuts are derived from fitted Monte Carlo samples. These are corrected through control samples of B decays from data with similar kinematics but with much larger branching fractions than the signal. Any errors from incorrect modelling are therefore accounted for in a systematic error.

4.4 Blind Analysis

The analyses conducted within this report are conducted without observing the signal region in data samples, until the end. This reduces the risk of biasing our results. To conduct this type of analysis we must first define a signal region in phase space. We chose to parameterise phase space in terms of the two kinematic variables ΔE

and M_{ES} (defined in section 4.3), which are almost uncorrelated. To construct our analysis dependent signal box we fit to Monte Carlo data in each variable prior to any selection and place a three standard deviation cut; this is our signal region. The size of the signal box is mode dependent. Figure 4.1 shows this process for the $B^+ \to \pi^+ K^{*0}$ decay mode. The blinded region is extended to cover a slightly greater area to eliminate the possibility of being influenced by boundary signal events.

Three areas around the signal region are used for characterisation of the backgrounds and selection optimisation. The one shown in Fig 4.1 is the grand-side-band (GSB) and is used for signal optimisation. The number of events in this region is used to estimate the amount of combinatoric background in the signal region. In order to extrapolate the number of events in the GSB to the signal region, the background in this plane must be characterised. A further two regions are used in conjunction with the GSB to accomplish this. They correspond to distributions in M_{ES}, in ΔE side-bands, above and below the signal region. A ratio R corresponding to the number of background events in the signal region to grand-side-band is constructed from the background characterisation so that RN_{GSB} is the amount of combinatoric background in the signal region, where N_{GSB} is the number of events observed in the grand-side-band. This technique of background characterisation is not unique to "blind" analyses.

Additional backgrounds from specific B decays are also taken into account for each decay mode via comprehensive background checks using Monte Carlo simulated data.

4.5 Event Selection

4.5.1 Preselection

The candidate particles in these analyses are created from reconstructed detector information: charged tracks, in conjunction with EMC, IFR and DIRC information, and neutral particles from EMC bumps with no associated track information. The B

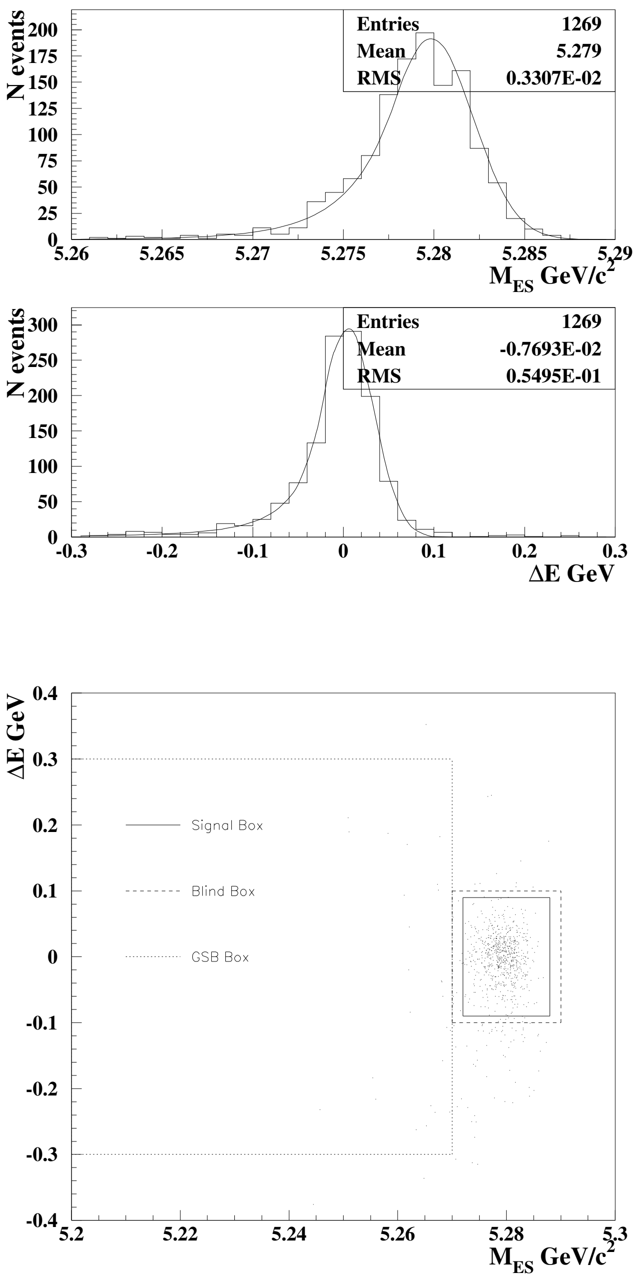

Figure 4.1: (Top) Fits of ΔE and M_{ES} using gaussian fit with a power law tail. This type of fit is know as a Crystal Ball fit. (Bottom) The constructed signal, blind and grand-side-band regions for $B^+ \to \pi^+ K^{*0}$, $K^{*0} \to K_s^0 \pi^0$.

candidates are supplied at the analysis level as a list. These used in these analyses are constructed from a charged track supplied by the *ChargedTracks* list (this being a selected list of charged tracks), a composite candidate list of π^0 candidates and a composite list of K_S^0 candidates. All three lists are created at the reconstruction stage. The selection limits on these initial candidates are very loose. Selection criteria for charged tracks and π^0 candidates are covered in section 4.5.2 and section 4.5.3 respectively. K_S^0 selection criteria are detailed in section 4.5.4. The constraint on the absolute difference between the reconstructed and expected B meson energy, $|\Delta E|$, is that it must be less than 450 MeV. Due to the dependence of ΔE on the daughter masses both kaon and pion mass hypotheses are used to calculate ΔE. The beam-energy substituted B mass, M_{ES}, of the reconstructed B meson must be within 100 MeV/c^2 of the centre of mass beam-energy limit, $\sqrt{s}/2$. There may exist more than one B candidate per event in our selected samples. While no particle identification selection is imposed at this stage a number of particle identification selectors are run over the tracks for use later. Further information on masses and decay angles of all B meson daughter combinations is calculated and stored so that the resonances can be studied. A total of over 200 variables are stored in the $h^{\pm}\pi^0 K_S^0$ selection. As the charged track can be either a pion or kaon, any quantity that is reliant upon the masses of the B daughters is entered for every combination of mass hypothesis.

4.5.2 Track Selection

The charged tracks used in this analysis come from the *GoodTracksLoose* list, a detailed definition of this can be obtained in [19], which satisfy the following track criteria:

- the number of **DCH** hits > 12,
- the track momentum $p < 10$ GeV/c,
- the transverse momentum $p_t > 0.10$ GeV/c,

- the distance of closest approach to the interaction point in the x-y plane < 1.5 cm,
- the absolute distance of closest approach to x-y plane must be < 10 cm.

Tracks are first reconstructed from hits in the drift chamber (**DCH**). They are then projected into the silicon vertex tracker (**SVT**). While Monte Carlo studies result in almost a 100% efficiency for tracking, actual data is not so accommodating. The tracking efficiency for *GoodTracksLoose* tracks in data has been studied as a function of momentum, θ, ϕ and multiplicity by the *Tracking Efficiency Task Force* [20]. Due to the dependence of *GoodTracksLoose* on the drift chamber the tracking efficiency study uses tracks selected by the silicon vertex tracker. Tables of tracking efficiency corrections were produced that are used with signal Monte Carlo to estimate an efficiency correction for each track. Overall efficiency corrections for tracking are imposed per event. The systematic error is due to the assumption made in measuring the data efficiency and was estimated to be 1.2% per track.

4.5.3 π^0 Selection

There exist two lists of π^0's that are available for use in analyses. They correspond to a list of merged π^0's and a list of resolved π^0's. A merged π^0 is defined as a single deposit within the electromagnetic calorimeter and is not associated with a track. These merged π^0's have a high energy. Not incorporating them into the analyses reduces the background considerably and hence they are vetoed after preselection. The remaining resolved π^0 list consists of those neutral pions reconstructed from a combination of two **EMC** deposits that are not associated with any tracks. The list imposes the initial constraints of 100 MeV/c^2 $< M_{\gamma\gamma} <$ 160 MeV/c^2 on mass and a photon energy limit of $E_\gamma >$ 30 MeV. A further constraint is made on the lateral energy distribution of the photon showers within the calorimeter, $0.0 <$ **LAT**< 0.6. Lateral shower distributions differ significantly between hadronic and electromagnetic showers. Electromagnetic showers are typically confined to one or two crystals whereas hadronic showers are typically broader. Hence LAT is smaller for electromagnetic showers when compared to hadronic ones. If the number of crystals associated with an electromagnetic shower is defined as N, the LAT of a shower is defined as:

$$\mathrm{LAT} = \frac{\sum_{i=3}^{\mathrm{N}} E_i r_i^2}{\sum_{i=3}^{N} E_i r_i^2 + E_1 R_0^2 + E_2 R_0^2} \tag{4.4}$$

R_0 is the average distance between the centres of crystals, which is 5 cm for BaBar. r_i is the distance from the centre of the cluster to the centre of the i^{th} crystal. The energy deposits are labelled such that $E_1 \geq E_2 \geq \cdots \geq E_N$, were E_i is the energy deposited in the i^{th} crystal.

The π^0 efficiency has been measured in data by the Neutral Analysis Working Group at BaBar using τ decays [26]. The results showed lower efficiency in data than in simulations and a correction of 0.939 ± 0.022 for energies up to 3 GeV was recommended. For modes containing a bachelor π^0 (particle direct from the B meson decay), for which energies can extend to 4.5 GeV, correction instructions were devised from $B^+ \to h^+ h^0$ decays [29]. Here the data is refitted with a linear dependence in energy for π^0 candidates above 3 GeV. The correction stated is $0.971 \pm 0.026 \times E_{\pi^0}$ with a recommended 5 % systematic error.

4.5.4 K_S^0 Selection

Studies on K_S^0 reconstruction have been carried out at BABAR [30]. We only consider $K_S^0 \to \pi^+\pi^-$ in our analyses. This therefore imposes an initial loss of 33% on our expected efficiency. The K_S^0 is reconstructed by pairing all possible tracks of opposite sign and looking for the point where they have a common vertex. The vertex fit is then required to have $\chi^2_{prob} > 0.01$ and the resultant invariant mass must lie between 450 MeV/c^2 and 550 MeV/c^2. Finally the K_S^0 decay point must be greater than 2 mm from the primary vertex in the x-y plane and no greater than 50 cm away in any direction. The result is the *KsDefault* list, which is used in this analysis as the source of K_S^0's. Along with constraints on the mass we impose an additional lifetime significance cut. This is defined as the flight length divided by the error on the flight length. Only events that are inconsistent with having originated at the primary vertex are selected. This selection is most powerful as Figure 4.2 shows.

4.5.5 Resonant Mass Selection

The resonant mass is a result of the 4-vector addition of the K_S^0 and π^0 in the case of K^{*0}, K_S^0 and π^+ in the case of K^{*+} or π^+ and π^0 in the case of the ρ^+. Each resonant mass is then fitted with either a Breit-Wigner or double gaussian before a fitted resolution cut of three standard deviations is applied.

4.5.6 Event Shape Variables

The B mesons are produced almost at rest in the centre of mass frame resulting in a spherical decay. In contrast the primary source of background, continuum events where $e^+e^- \to u\overline{u}$, $d\overline{d}$, $s\overline{s}$ and $c\overline{c}$, are jet like. This fundamental shape difference is utilised to allow us to distinguish between our background and signal.

In calculating the event shape variables we separate the event into the three particles that make up the B candidate and the "rest of the event". Three event shape variables are used in this analysis.

- $\cos\theta_T$; The thrust angle. θ_T is defined as the angle between the direction of the thrust of the B candidate and the thrust of the rest of the event in the centre of mass frame. The direction of the true B thrust is random resulting in a flat distribution for B events. For continuum background a strong peak is observed at zero due to the jet nature where the fake B candidate will tend to lie along the axis of the jets.
- The Fisher discriminant: This is a function of several variables. It is summed energy of the rest of the event taken in nine energy cones around the thrust axis

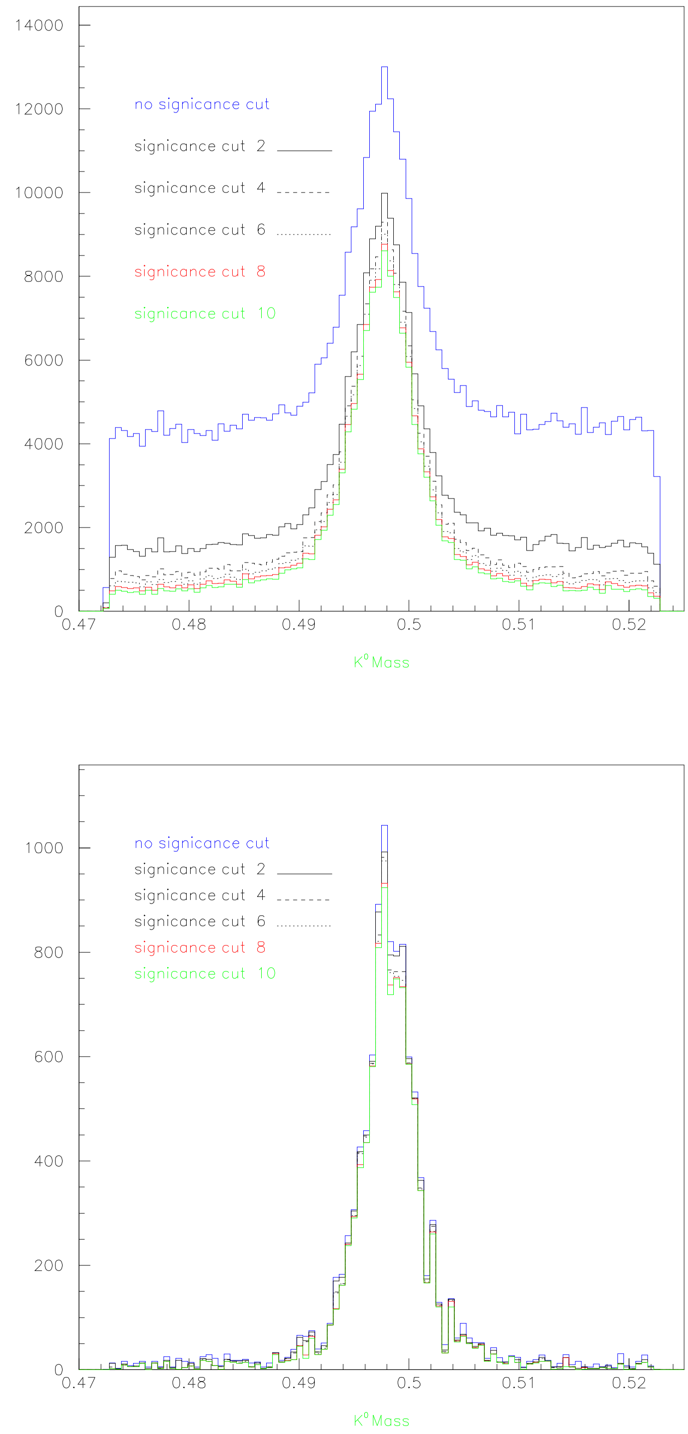

Figure 4.2: This shows the mass of the K_S^0 after successive life-time significance cuts for data (Top) and MC (Bottom)

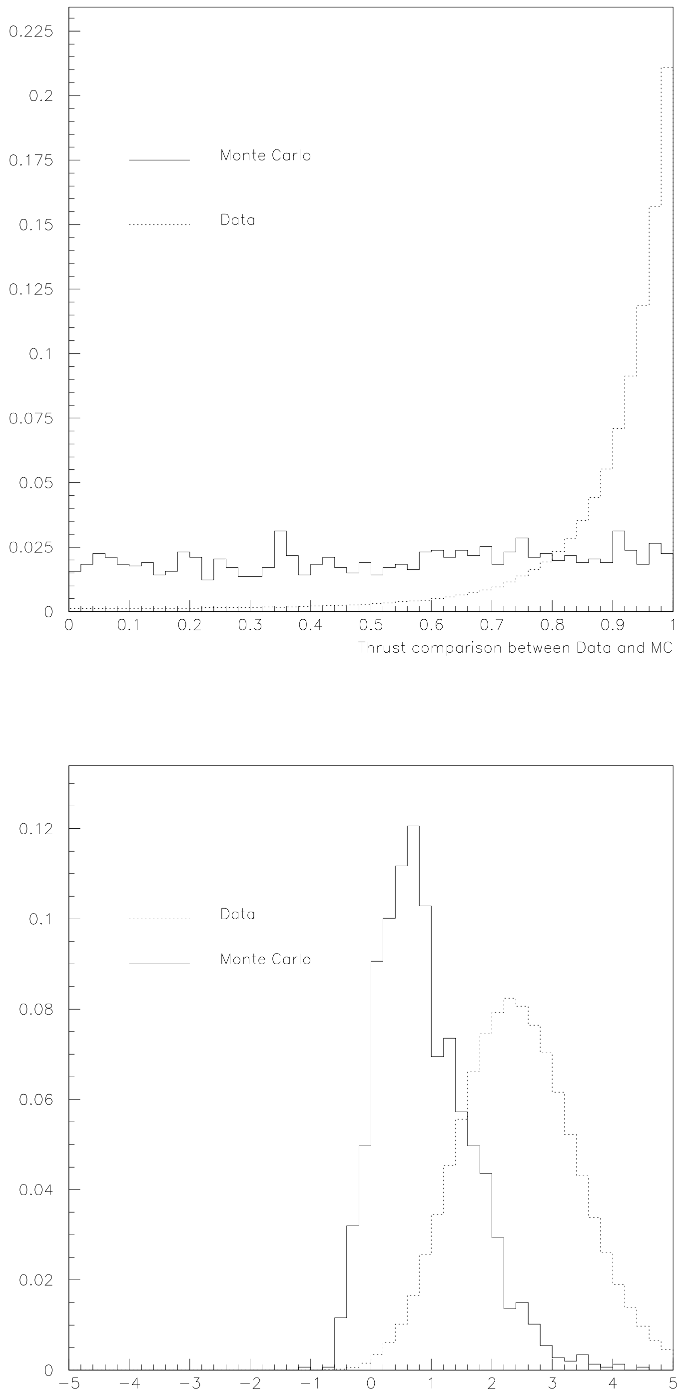

Figure 4.3: Comparisons of the Thrust and Fisher discriminant between continuum background and Monte Carlo signal data for the $B^+ \to K^{*+}\pi^0$ decay.

of the B candidate, the cosine of the B thrust axis with respect to the beam axis and the cosine of the B decay axis with respect to the beam axis.

- $\cos\theta_H$: θ_H is defined as the angle between the direction of flight of the B meson and the direction of decay of the daughters of the resonance in the B meson frame. Studies were conducted on both a folded and unfolded helicity distribution in an attempt to improve efficiency and reduce backgrounds.

4.6 Particle Identification

The use of particle identification information to discriminate between pions and kaons is necessary to reduce backgrounds. The kaon selection in BaBar is mainly based on the information from the silicon vertex tracker (**SVT**), the drift chamber (**DCH**) and the internally reflecting Cherenkov detector (**DIRC**) as detailed in sections 3.4.2, 3.4.3 and 3.4.4 respectively. The analyses in this report use the standard BaBar kaon selection, the *SMSKaonSelector* [27]. The *SMSKaonSelector* uses dE/dx information from the **SVT** and **DCH** for candidates with momentum below 0.7 GeV/c and **DIRC** information for candidates with momentum above 0.6 GeV/c. The **DIRC** likelihood is calculated from a comparison of the Cherenkov angle and the number of photons to the expected values for that particle hypothesis, where a gaussian is assumed for the angle and a poisson distribution for the number of photons. The **SVT** and **DCH** likelihoods are calculated from the deviation of dE/dx values from the expected ionisation values that are modelled on the five parameter Bethe-Bloch formula. For the SVT a three parameter Bethe Bloch formula is used. Where overlap occurs in the detectors the best reading is taken.

In the analyses reported in this document pion candidates are required to fail the *SMSKaonSelector* in its tight configuration.

4.7 Best Candidate Selection

A consequence of having a final state containing a neutral pion is that one observes multiple candidates per event. Even after selection criteria have been applied this problem still exists. It is necessary to resolve this problem before conducting further studies. Selecting one candidate and discarding all others overcomes this problem. It is done on an event-by-event basis, where we construct a χ^2 to distinguish the best candidate using π^0 and K_s^0 candidates.

$$\chi^2_{\rm cand} = \left(\frac{\mathbf{M}_{\pi^0} - 0.135}{\pi^0\text{Resolution}}\right)^2 + \left(\frac{\mathbf{M}_{K_s^0} - 0.498}{K_S^0\text{Resolution}}\right)^2$$

M_{π^0} and $M_{K_s^0}$ represent the reconstructed masses with resolution equal to the measured width. We obtain both these values by fitting to the distributions after applying all selection criteria.

4.8 Background Characterisation

It is important to note that if we use the full data set to conduct both background characterisation and selection optimisation we risk biasing our results. We would risk optimising with respect to background fluctuations. This problem is amplified when dealing with low statistics. To counter this the selected events used in background characterisation are not used in the selection optimisation process. In background characterisation we use every odd event in the data sample.

To approximate the level of combinatoric background expected in the signal regions we first determine the shape of the backgrounds for each mode across the phase space in which we wish to optimise. Once characterisation is achieved the expected number of background events in the signal regions can be calculated from the number of background events in the sidebands.

$$B_{Signal} = RN_{GSB}$$

B_{Signal} is the number of background events expected in the signal region. N_{GSB} is the number of events located in the grand-side-band, as defined in figure 4.1. The ratio factor 'R' accounts for the relative areas covered. Figure 4.4 (top-left) shows the three regions used for characterisation.

Two projections are used for M_{ES} characterisation. Here we use $5.2 < M_{ES} < 5.3$ GeV/c^2 for $0.1 < \Delta E < 0.3$ GeV and $-0.3 < \Delta E < -0.1$ GeV as a demonstration. We designate these the upper and lower bands respectively. The fits are checked in each before combining them into a single projection. We use the Argus function to parameterise these distributions.

$$\frac{dN}{dx} = Ax\sqrt{1-x^2}\exp[-\xi\sqrt{1-x^2}] \tag{4.5}$$

where $x = M_{ES}/M_{max}$ and the ξ parameter is determined from the fit. The A normalisation parameter is also determined from the fit. Figure 4.4(top-right and bottom-left) shows the fits for the $B^+ \to K^{*0}\pi^+$ mode. Table 4.2 lists the results. We use the area

Argus parameter value	
Area fitted	Value
Upper Band	15.3 ± 11.8
Lower Band	24.5 ± 7.4
Both Bands	24.9 ± 6.3

Table 4.2: The Argus ξ parameter for On-Resonant data after applying selection criteria and best candidate selection. We use the combined value for our characterisation.

$-0.3 < \Delta E < 0.3$ GeV and $5.2 < M_{ES} < 5.27$ GeV/c^2 for ΔE characterisation, again as an example. Figure 4.4 (bottom-right) shows the shape of the background in this region. We now calculate the 'R' value as a product of the ratios of both fits. For M_{ES}:

$$\frac{\int_{5.272}^{5.288} Ax\sqrt{1-x^2}\exp[-\xi\sqrt{1-x^2}]dx}{\int_{5.2}^{5.27} Ax\sqrt{1-x^2}\exp[-\xi\sqrt{1-x^2}]dx} = 0.15 \pm 0.015 \tag{4.6}$$

For ΔE:

$$\frac{\int_{-0.09}^{0.09} -17.15x + 15.57dx}{\int_{-0.3}^{0.3} -17.15x + 15.57dx} = 0.3 \tag{4.7}$$

Hence we calculate the ratio product as $R = 0.3 \times 0.15 = 0.045 \pm 0.005$. The error shown is due to the one standard deviation error from the Argus fit. This method is used in all analysis modes.

4.9 Selection Optimisation

In optimising our selection criteria we maximise the signal to background ratio $S/\sqrt{S+B}$. Studies were conducted into using $S/\sqrt{B}$ but no significant difference was observed. In continuation of being unbiased we use only even events to conduct the optimisation procedure. The signal S is calculated as $S = \sigma L B_R \epsilon$, where σ is the $B\overline{B}$ cross section, L is the luminosity, B_R is the assumed branching fraction (calculated using the upper limits from Table 4.1) and ϵ is the efficiency of the selection as calculated from Monte Carlo Simulation. B is the number of events observed in the grand-side-band multiplied by the product ratio, as explained in section 4.8 and calculated in Section 5.1.1. We optimise using 19.424fb^{-1} of on-resonance data and 6000 mode specific Monte Carlo events. We optimise with all the selection criteria applied. After each parameter is optimised we update the value and continue. The cuts on the following quantities are optimised.

- Fitted resonant mass, as a function of its width.
- Fisher discriminant, optimised over a range specific to each mode.
- Helicity angle, where studies were conducted using both a folded and unfolded helicity.
- $|\cos\theta_T|$ optimised over a range specific to each mode.

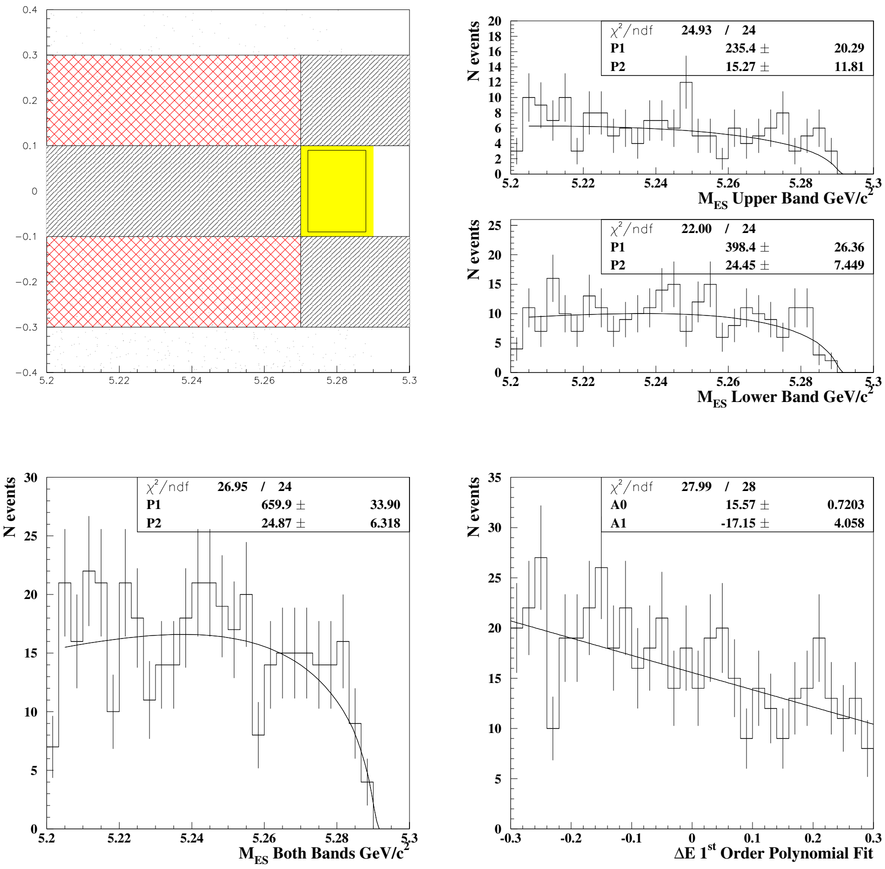

Figure 4.4: Top-left shows the regions used for characterisation of M_{ES} and ΔE. Top-right shows the Argus shape for the upper and lower bands. Bottom-Left represents the combination of both upper and lower bands, again with an Argus fit. Bottom-Right shows the ΔE for odd events fitted with a first order polynomial.

- Mass of K_S^0 optimised with respect to the fitted mass distribution.
- K_S^0 Lifetime significance.
- Photon energies, which are optimised together.
- Photon Lateral energy distribution, again optimised together.
- Reconstructed π^0 mass, optimised with respect to the fitted mass range.

Once we have the optimised values we re-characterise the background distribution to obtain a new background characterisation 'R' value.

Chapter 5

Results

This chapter describes the mode specific analyses and presents the results for:

- $B^+ \to K^{*0}\pi^+$, $K^{*0} \to K^0_S\pi^0$
- $B^+ \to K^{*+}\pi^0$, $K^{*+} \to K^0_S\pi^+$
- $B^+ \to \rho^+ K^0_S$, $\rho^+ \to \pi^+\pi^0$.

5.1 $B^+ \to K^{*0}\pi^+$, $K^{*0} \to K^0_S\pi^0$

This section describes the analysis $B^+ \to K^{*0}\pi^+$, $K^{*0} \to K^0_S\pi^0$. Table 5.1 shows the bounding limits used on the signal and grand-side-band boxes as depicted by Figure 5.1.

Table 5.2 shows the effects of each successive cut as it was applied to 6000 Monte Carlo events. The result was an overall efficiency of 11.7%. Here we defined 'events' as the number of events containing at least one candidate after selection criteria have been applied. 'Mean Candidates per event' was defined as the mean number of candidates per event after each selection criterion is applied. 'Efficiency' was defined as a function of the number of events containing at least one candidate present in the signal region

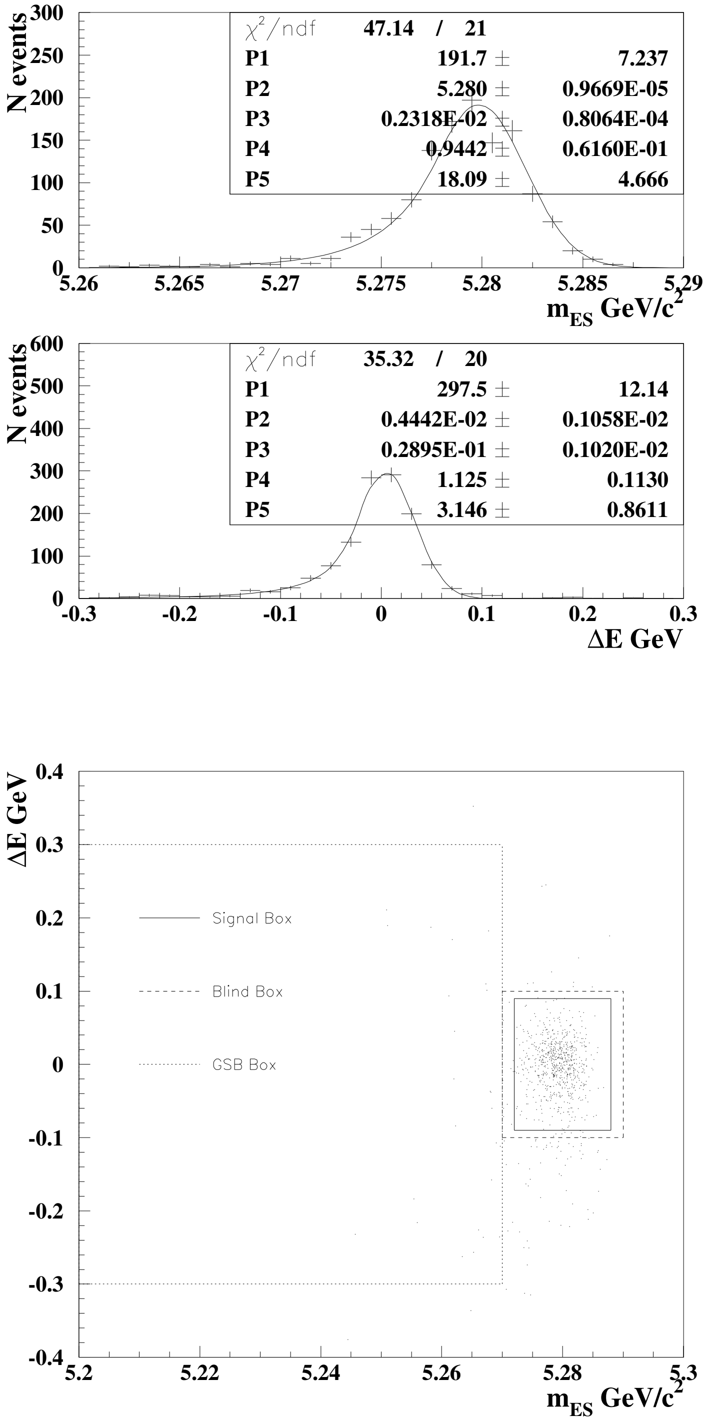

Figure 5.1: The top two plots show ΔE and M_{ES} distributions fitted with a gaussian and a "power law" tail, also known as a Crystal Ball fit (see Appendix A). The bottom plot shows the resultant signal box by imposing a 3σ cut on each, where the σ comes from the gaussian part of the distribution. The 'P' parameters in the top plot are as follows; P1 is an arbitrary amplitude, P2 is the mean of the gaussian fit, P3 is the width of the gaussian fit while P4 gives the merge point of the two fits and P5 is the power function in the power law.

Area	ΔE bounded (GeV)	M_{ES} bounded (GeV/c^2)
Signal Region	$\|\Delta E\| < 0.09$	$5.272 < M_{ES} < 5.288$
Grand Sideband	$\|\Delta E\| < 0.3$	$5.2 < M_{ES} < 5.27$

Table 5.1: The signal box and grand-side-band box as calculated from 6000 Monte Carlo mode specific events.

after selection criteria had been applied. Figure 5.2 shows some of these distributions, comparing Monte Carlo signal events to background events from the data.

5.1.1 Background Characterisation

Figure 5.3 shows the shape of the background in the M_{ES} and ΔE regions. We calculated the product ratio from both fits to estimate the level of background expected in the signal region.

For M_{ES}:

$$\frac{\int_{5.272}^{5.288} Ax\sqrt{1-x^2}\exp[-\xi\sqrt{1-x^2}]\ dx}{\int_{5.2}^{5.27} Ax\sqrt{1-x^2}\exp[-\xi\sqrt{1-x^2}]\ dx} = 0.15 \pm 0.015 \tag{5.1}$$

For ΔE:

$$\frac{\int_{-0.09}^{0.09} -17.15x + 15.57\ dx}{\int_{-0.3}^{0.3} -17.15x + 15.57\ dx} = 0.3 \tag{5.2}$$

Hence we calculated the ratio product to be R $= 0.3 \times 0.15 = 0.045 \pm 0.005$. The error shown is due to the one standard deviation error from the Argus fit.

5.1.2 Unfolding the Helicity Angle

A study into unfolding the helicity distribution was conducted. This was an attempt to improve efficiency and background suppression. As shown in figure 5.4 there is an asymmetric distribution of the background. This effect is due to large combinatorics

$B^+ \to K^{*0}\pi^+$ Selection Cut Efficiencies (%)			
Selection Cut	Events	Mean Cand/Event	Efficiency
Preselection and signal Box	1581	2.13	26.35
$0.804 < M_{K^{*0}} < 0.986$ GeV/c^2	131	1.525	21.83
e^- veto (track $E/p < 0.9$)	1309	1.52	21.82
track 1 Not a Kaon	1263	1.53	21.05
Fisher < 1.25	947	1.48	15.78
$\lvert\cos\theta_H\rvert > 0.3$	919	1.49	15.32
$\lvert\cos\theta_T\rvert < 0.8$	836	1.47	13.93
$0.490 < m_{K^0_S} < 0.506$ GeV/c^2	793	1.47	13.22
$c\,\tau\ /\ \sigma_{c\tau} > 6$	751	1.48	12.52
$E_\gamma > 0.03$ GeV	751	1.47	12.52
$0 < LAT < 0.6$	742	1.47	12.37
Is a Composite	742	1.47	12.37
$\lvert M_{\gamma\gamma} - m_{\pi^0}\rvert < 0.02$ GeV/c^2	703	1.32	11.72
Total Raw Efficiency, $\epsilon_{raw\ MC}$	703	1.32	11.72

Table 5.2: Initial selection criteria with corresponding total efficiency. The mean number of candidates per event demonstrates the need for a best candidate selection.

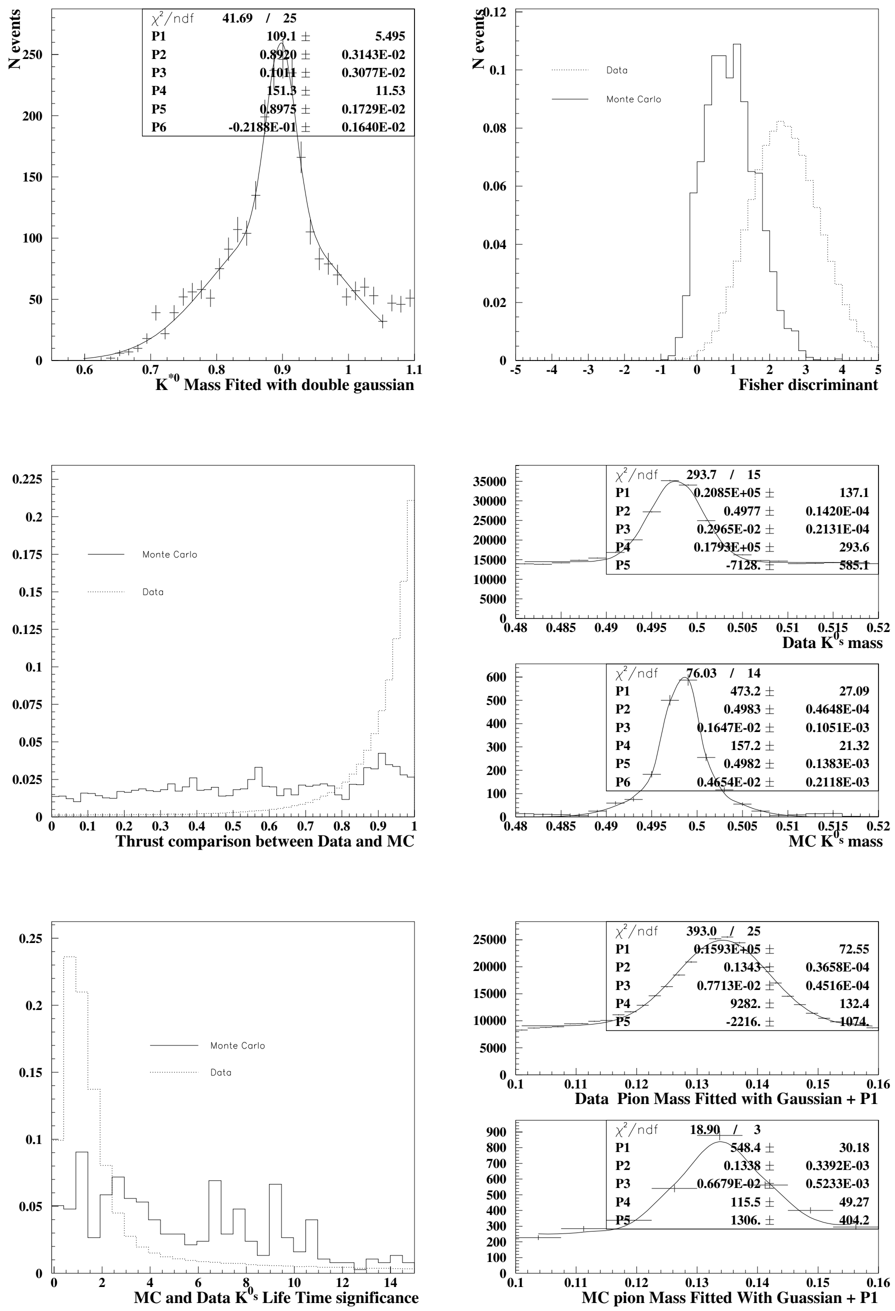

Figure 5.2: This figure shows the event shape distributions for $B^+ \to K^{*0}\pi^+$. From top left to bottom right we have the Monte Carlo K^{*0} resonant mass fitted with a double gaussian, the Fisher discriminant for Monte Carlo and data, the thrust comparison for Monte Carlo and data, K_S^0 mass fitted with a gaussian to a linear background, the lifetime significance variable and the π^0 mass for Monte Carlo and data.

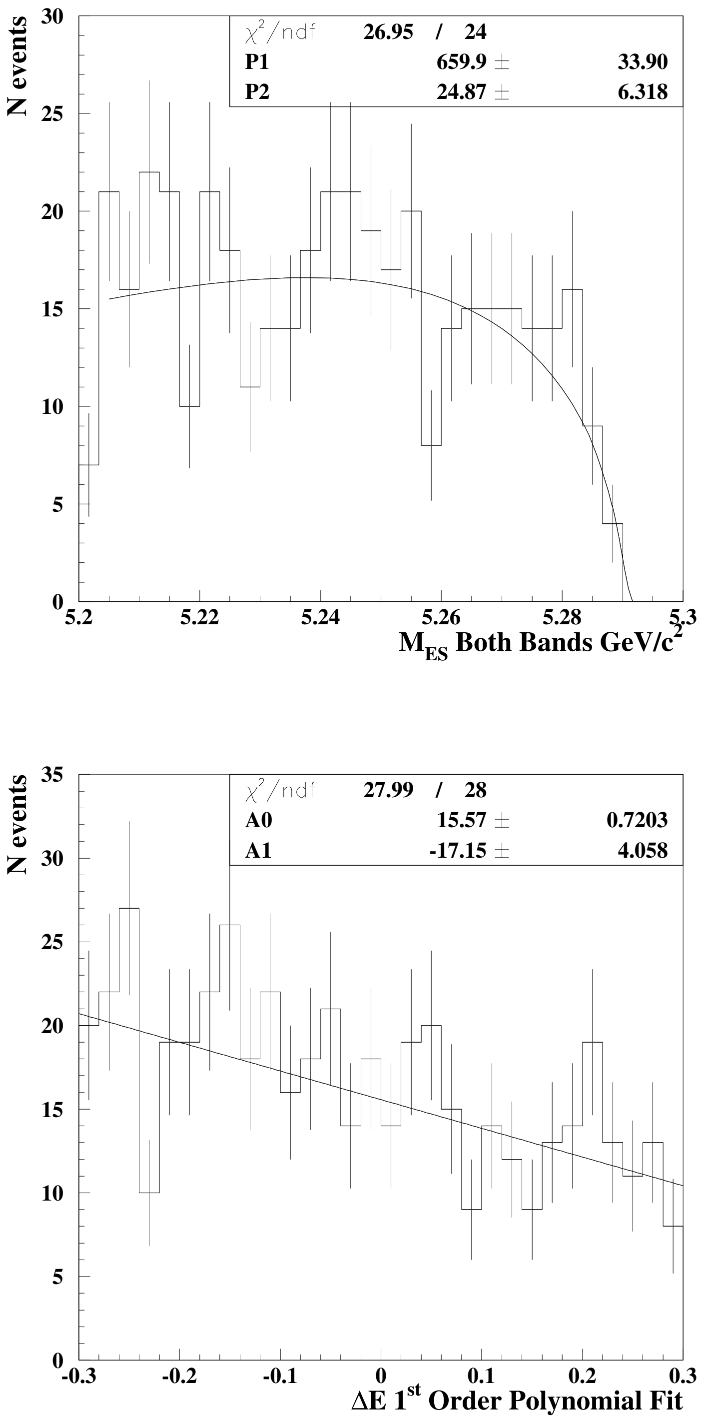

Figure 5.3: The top plot shows the combined upper and lower bands in M_{ES} fitted with an Argus shape. The bottom plot shows the ΔE distribution fitted with a first order polynomial.

Argus parameter value	
Area fitted	ξ Value
Upper Band	15.3 ± 11.8
Lower Band	24.5 ± 7.4
Both Bands	24.9 ± 6.3

Table 5.3: The Argus ξ parameter for data after applying selection criteria and best candidate selection. We use the combined value for our characterisation.

involving a low energy π^0 candidate. This only occurs at $\cos\theta_H \cong -1$ as only the K_s^0 is used for helicity angle characterisation, hence when the angle between the direction of the B meson and K_s^0, in the resonant rest frame, is large, the resultant π^0 momentum is small. The unfolded helicity of the Monte Carlo $B^+ \rightarrow K^{*0}\pi^+$ events shows no asymmetry, as expected from a decaying vector particle. Optimisation was conducted across the whole region. The final cuts applied were $\cos\theta_H > -0.95$ and $|\cos\theta_H| > 0.2$

5.1.3 Selection Optimisation

We optimised the selection criteria with the method described in section 4.9. After each parameter was optimised the value was updated before continuing. Criteria optimised were:

- K^{*0} mass optimised with respect to fitted mass from $\pm 2\sigma$ to $\pm 5\sigma$.
- The Fisher discriminant; optimised over range 0.25 to 2.
- Studies were conducted using both a folded and unfolded helicity. An unfolded helicity angle was selected. See section 5.1.2.
- $|\cos\theta_T|$ optimised over range 0.1 to 1.0.
- K_s^0 mass range optimised with respect to fitted mass distribution from $\pm 1\sigma$ to $\pm 6\sigma$.

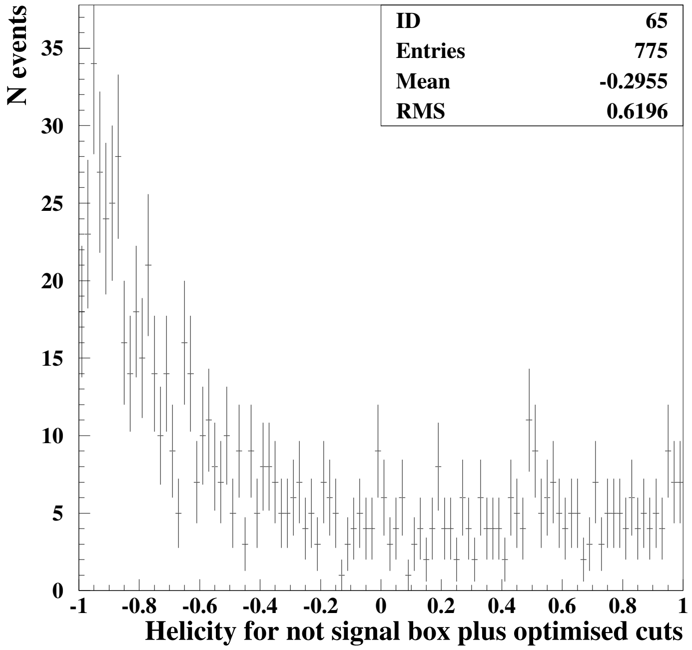

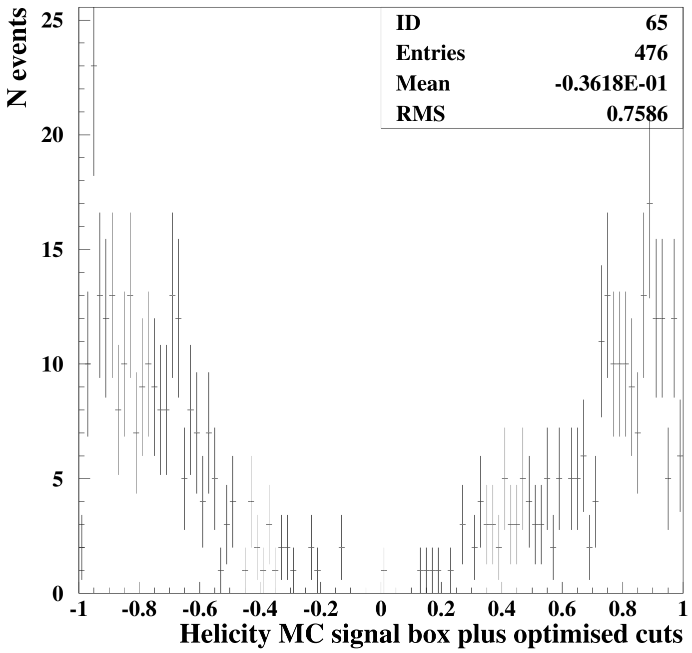

Figure 5.4: Top plot shows the unfolded helicity angle for data with all optimised cuts excluding the signal box region. The bottom plot shows the unfolded helicity for Monte Carlo $B^+ \to K^{*0}\pi^+$ events with optimised cuts and signal region specified. Both plots have all other optimised selection criteria applied.

- Lifetime significance is optimised over range 2 to 10.
- Photon energies are optimised together over the range 30 MeV to 200 MeV.
- Lateral energy distribution is optimised over the range 0.0 to 1.0.
- Reconstructed π^0 mass optimised with respect to fitted mass ranging from $\pm 1\sigma$ to $\pm 4\sigma$.

Table 5.5 shows that the greatest drop in efficiency was due to the Fisher selection cut. Although a tighter cut was observed to give greater $S/\sqrt{S+B}$ values one reaches a point where this optimisation process breaks down. This occurs when we have high background to signal. Hence a selection of Fisher < 0.75 was taken as harsh enough, this was achieved by eye. After optimising the selection criteria the background characterisation required repeating. Figure 5.5 shows the new background distributions whose value is given in Table 5.4. Again the upper and lower M_{ES} bands are combined before fitting.

Argus parameter value	
Area fitted	Value
Both Bands	34.1 ± 10.3

Table 5.4: Fitted ξ value after optimisation of cuts

5.1.4 Background Studies

Background from higher resonances was not expected to be large. Further background studies were conducted to identify possible contaminants. Studies were conducted on generic B decays (both charged and neutral), light quark modes ($e^+e^- \to u\overline{u}, d\overline{d}, s\overline{s}$), charm events ($e^+e^- \to c\overline{c}$) and on a cocktail of rare charmless modes. The cocktail incorporates rare two, three and four body final states. Table 5.6 shows the results of these searches. The three events from the charmless cocktail were investigated

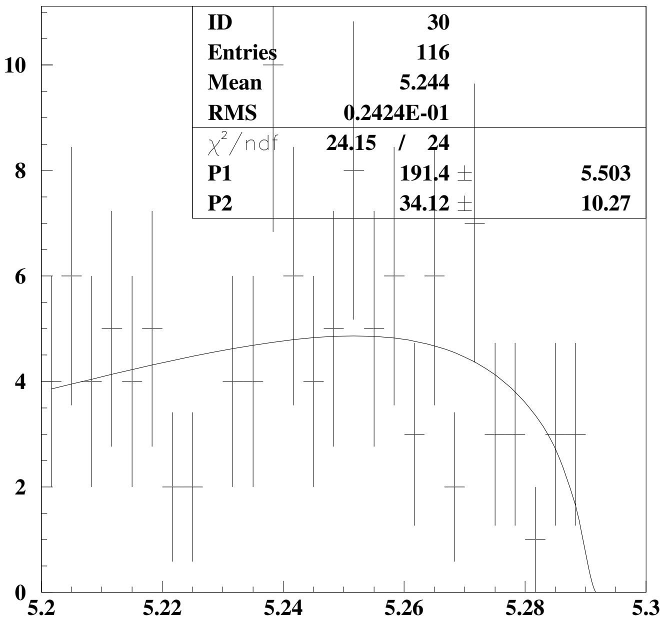

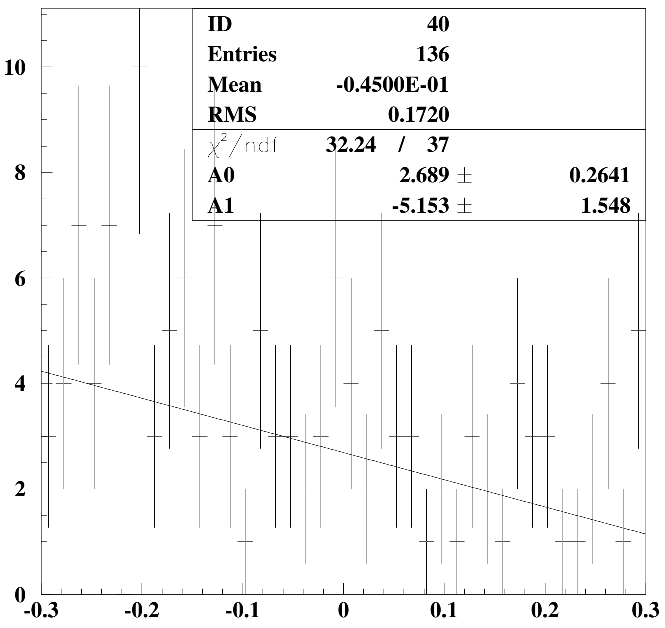

Figure 5.5: M_{ES} and ΔE distributions after optimisation and with optimised unfolded helicity

$B^+ \to K^{*0}\pi^+$ Selection Cut Efficiencies (%)			
Selection Cut	Events	Efficiency	Events in GSB
Preselection and signal Box	1581	26.35	NA
0.804 GeV$/c^2 < M_{K^{*0}} < 0.986GeV/c^2$	1274	21.23	134159
e^- veto (track $E/p < 0.9$)	1273	21.22	130848
track 1 Not a Kaon	1229	20.48	95874
Fisher < 0.75	616	10.27	2529
$\cos\theta_H > -0.95$ and $\lvert\cos\theta_H\rvert > 0.2$	588	9.93	2131
$\lvert\cos\theta_T\rvert < 0.7$	547	9.23	1421
$0.484 < m_{K^0_S} < 0.512$ GeV$/c^2$	538	9.05	1193
$c\,\tau\ /\ \sigma_{c\tau} > 4$	517	8.78	472
$E_\gamma > 0.05$ GeV	480	8.07	367
$0 < LAT < 0.5$	467	7.85	307
$0.1122 < M_{\gamma\gamma} < 0.1577$ GeV$/c^2$	450	7.6	275
Total Raw Efficiency, $\epsilon_{raw\ MC}$	450	7.5	275

Table 5.5: Efficiencies after optimisation of selection criteria have been applied. As seen a further $\cos\theta_H$ selection criterion was added, see section 5.1.2 for details. We still impose a best candidate selection criterion and only use resolved π^0's.

further to rule out any possible contaminant. They were a result of one four body final state where the last track is missing, a $K^{*+}\pi^+\pi^-$ event and the final one being a $B^- \to D^{*-}(2010)\pi^0$ with $D^* \to D^0\pi^-$ and $D^0 \to K_s^0\pi^0$.

	Events (10^6)	events in Signal Region	Scaled
B^+B^-	4.5	0	0
$B^0\overline{B^0}$	3.7	0	0
$c\overline{c}$	12.1	2	4
uds	18.1	2	4
Charmless Cocktail	1.1	3	3

Table 5.6: Shows results of possible contaminant check. We scale the Monte Carlo to the data set size.

The number of charmless cocktail events observed in the signal region were included in our background estimation. The continuum background is already accounted for from the grand-side-band estimation.

A check was also conducted into possible cross channel contamination. The optimised selection criteria were applied to 6000 Monte Carlo mode specific $B^+ \to K^{*+}\pi^0$, $K^{*+} \to K_s^0\pi^+$ and $B^+ \to \rho^+K_s^0$, $\rho^+ \to \pi^+\pi^0$ events. In each case the upper limit from table 4.1 was taken as the assumed branching fraction. 16 events passed the selection conditions which equated to 1 event in the signal region. This was small enough to neglect.

A further check was conducted on 22,000 $B^+ \to K^+K^{*0}$, $K^{*0} \to K_s^0\pi^0$ events. Optimised selection criteria were applied resulting in 77 events being selected. The upper limit for the resonant mode,$B^+ \to K^+K^{*0}$, was taken from the 2002 particle physics data group (UL $< 5.3 \times 10^{-6}$) [24], and combined with relative decay rates factored in for a final three-body state of $B^+ \to K^+K_S^0\pi^0$. This resulted in 0 events being expected in the signal region. These results are given in table 5.7.

Resonant Mode	Events selected	Events in Signal region
$K^{*+}\pi^0$	0	0
$\rho^+ K_s^0$	16	1
$B^+ \to K^+ K^{*0}$, $K^{*0} \to K_S^0 \pi^0$	77	0

Table 5.7: Possible cross channel and misidentified π^+ contamination check.

5.1.5 Efficiency corrections

Table 5.8 contains all corrections applied to the Monte Carlo signal efficiency. Corrections were applied to several of our selection criteria. Errors on these corrections provide an overall systematic uncertainty on our final result. The mode under investigation contains only one charged track we need to concern ourselves with. (The $\pi^+\pi^-$ that make up the K_s^0 are dealt with separately). We follow the Tracking Efficiency working group recommendations [20] and incur a systematic error of 1.2% for our GoodTracksLoose candidate. The K_s^0 Monte Carlo correction again comes from the Tracking Efficiency working group. A systematic of 2.6% is applied. Particle Identification corrections were made using the recommended PID tables and method [25]. The π^0 corrections are conducted in accordance to the recommendations made by the Neutral Identification and Reconstruction AWG [26]. Corrections to Monte Carlo in regards to ΔE and M_{ES} distributions were calculated through the calibration channel $B^+ \to \overline{D^0}\pi^+$. Full details are given in section 5.1.6.

5.1.6 $B^+ \to \overline{D^0}\pi^+$ Calibration Channel.

The aim of the calibration channel is to correct for Monte Carlo simulation inconsistenties with real data. This is achieved by choosing a similar mode to that studied, which has a much higher branching fraction, and examining the Monte Carlo and data returns from similar cuts. For this report the calibration channel was used to produce efficiency corrections as well as systematics on the ΔE and M_{ES} parameters.

	Correction
Tracking	0.988 ± 0.012
K_s^0	0.964 ± 0.026
π^0	0.939 ± 0.047
PID	0.997 ± 0.003
ΔE	$0.992^{+0.016}_{-0.015}$
M_{ES}	$0.978^{+0.018}_{-0.015}$
TOTAL	$0.865^{+0.060}_{-0.059}$

Table 5.8: This table shows the relevant corrections to be applied to our overall Monte Carlo calculated efficiency.

The calibration channel that was chosen was $B^+ \to \overline{D^0}\pi^+$ with secondary decays $\overline{D^0} \to K^0\pi^0$, K^0 decaying to K_S^0 and $K_s^0 \to \pi^+\pi^-$. The PDG [8] gives $\mathcal{B}(B^+ \to \overline{D^0}\pi^+) = (5.3 \pm 0.5) \times 10^{-3}$;$\mathcal{B}(\overline{D^0} \to K^0\pi^0) = (2.12 \pm 0.21)\%$;$\mathcal{B}(K^0 \to K_S^0) = (50)\%$; $\mathcal{B}(K_S^0 \to \pi^+\pi^-) = (68.61 \pm 0.28)\%$. The overall expected branching fraction was $(3.6 \pm 0.5) \times 10^{-5}$.

The analysis used was the same as that for $B^+ \to K^{*0}\pi^+$, excluding event shape selection criteria. Particle identification, M_{ES} and ΔE were consistent with the previous analysis as were both K_S^0 and π^0 selection. The resonant mass cut, after optimisation, was chosen to be $|M_{K\pi} - M_{D^0}| < 20$ MeV$/c^2$. The efficiency was calculated using 22,000 Monte Carlo signal events. Table 5.9 gives the overall branching fraction result. As can be seen the result is in good agreement with the PDG value.

Background Characterisation

For background characterisation the same bands were selected as those used in the channel under investigation (see Figure 5.6). Only the upper band (0.1 MeV$/c < \Delta E <$ 0.3 MeV$/c$ for 5.2 GeV$/c^2 < M_{ES} <$ 5.29 GeV$/c^2$) was used for M_{ES} characterisation. The lower band showed a possible resonance below our signal region. Due to this we

Monte Carlo Efficiency	0.12 ± 0.002
Corrected	$0.11 \pm 0.002 \pm 0.004$
Number Background in Signal	$139 \pm 12 \pm 7$
Events in Signal Region	229 ± 15
Signal Yield	$90 \pm 19.2 \pm 7$
Branching Fraction	$(3.4 \pm 0.44 \pm 0.23) \times 10^{-5}$

Table 5.9: Calibration Channel Efficiencies.

rescaled our characterisation region to exclude this region. An R value of (0.058 ± 0.003) was obtained.

ΔE and M_{ES}

We compared these distributions in Monte Carlo and data to correct for imperfect modelling in our $B^+ \to K^{*0}\pi^+$,$K^{*0} \to K_s^0\pi^0$ mode specific Monte Carlo . Figure 5.7 shows these distributions for our calibration channel. Table 5.10 gives the full details.

	MC	Data	shift/scale factor
ΔE mean (MeV)	3.3 ± 0.5	-4.3 ± 4.3	-3.3 ± 4.3
ΔE σ (MeV)	25.34 ± 3.95	26.37 ± 3.76	1.04 ± 0.15
M_{ES} Mean (GeV)	5.279	5.279	NA
M_{ES} σ (GeV)	2.63 ± 0.01	3.20 ± 0.43	1.23 ± 0.16

Table 5.10: The resolutions and means of gaussian fits to Monte Carlo and data ΔE and M_{ES} distributions for $B^+ \to \overline{D}^0\pi^+$, $\overline{D}^0 \to K^0\pi^0$. The final column shows the scaling/shift of these comparisons. We are primarily concerned with the resolution.

We observed a shifting and an increase in the resolution. To extrapolate this back as an efficiency correction for $B^+ \to K^{*0}\pi^+$ we fixed the latter three crystal-ball parameters as described in the signal-box creation and varied the means and widths. The correction then became a ratio of the functions bounded by the signal box with

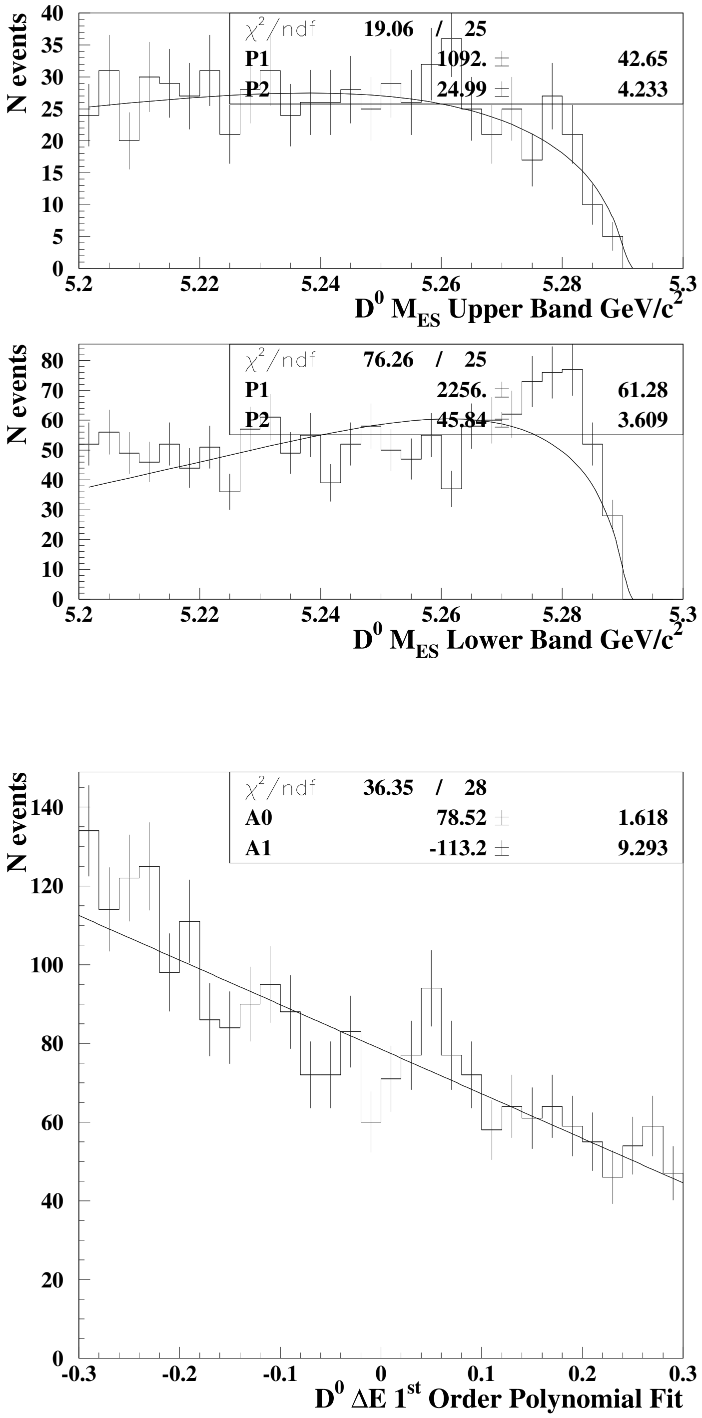

Figure 5.6: Top plot shows upper M_{ES} band fitted with an Argus function. The middle plot shows the contamination from possible resonances. (This is not used for background characterisation). Bottom plot shows the ΔE distribution fitted with a first order polynomial.

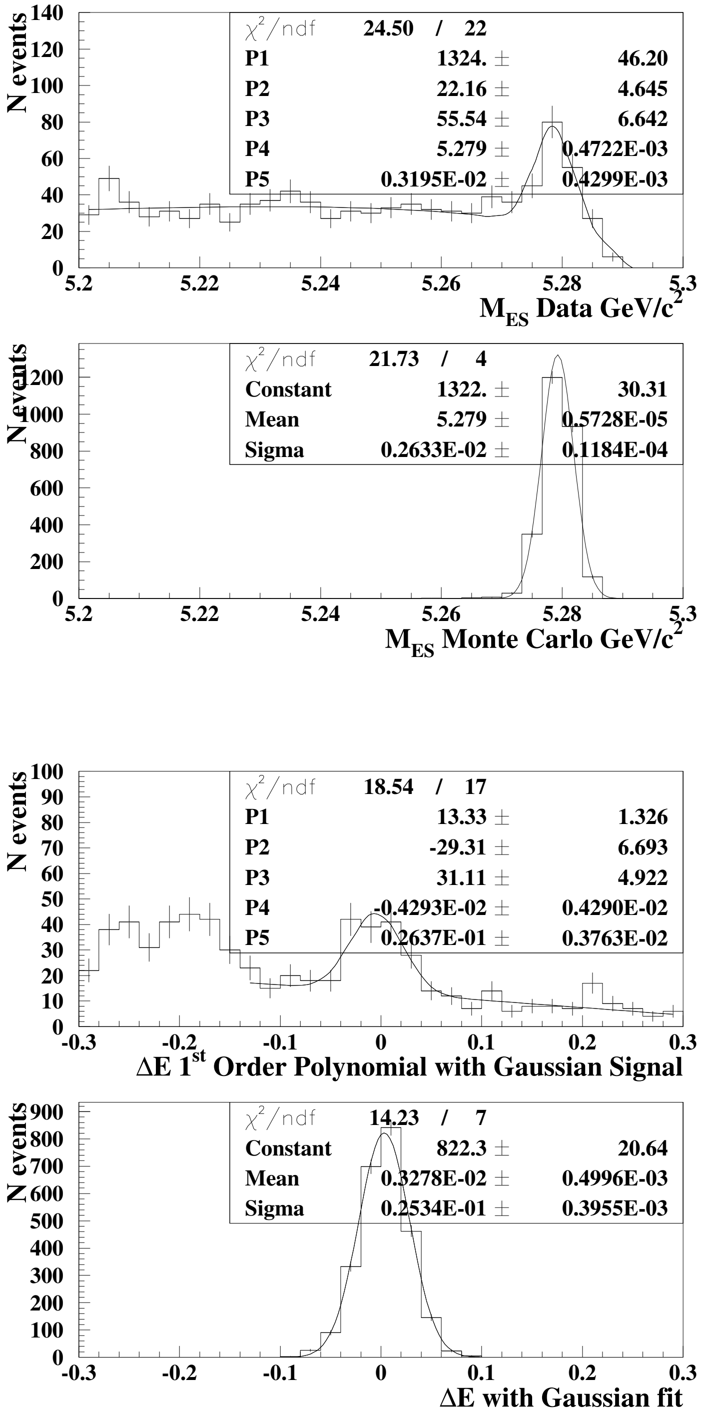

Figure 5.7: Top two plots show the energy substituted mass distributions for the calibration mode for both Data and Monte Carlo. Bottom two plots show the ΔE distributions for Data and Monte Carlo. Here we only fitted data from $\Delta E > -0.12$ so as to exclude the same region encountered in the lower ΔE band when conducting background characterisation.

errors calculated by the variation of the means and widths. The full method is given in Appendix B.

5.1.7 Results

The results for this decay mode are shown in table 5.11.

Events in GSB	275
Ratio R	0.052 ± 0.010
Expected BG in SR	$17.3 \pm 1.0 \pm 4.0$
Expected Signal in SR	$2.4 \pm 1.5 \pm 0.2$
Total Expected Events in SR	$19.7 \pm 1.8 \pm 4.0$

Table 5.11: Summary of background study and the number of expected events in the signal region with breakdown into expected background and signal events.

The optimised selection criterion gave 275 events in the grand-side-band. Re-characterisation of the background gave a product ratio of R $= 0.052 \pm 0.010$. Using RN_{sig} gives 14.3 background events. Combining with the 3 ± 3 charmless cocktail background events gave us an expected background number in the signal region of $17.3 \pm 1.0 \pm 4.0$. The large systematic error is due to the number of charmless cocktail candidates. The new total efficiency gaves an expected signal in the signal region of $2.4 \pm 1.5 \pm 0.2$, where the branching fraction had been assumed to be given by the branching fraction published by the BELLE collaboration [16]. The total expected number of events in the signal region was predicted to be $19.7 \pm 1.8 \pm 4.0$ with the main systematic error due to charmless background.

The unblinded M_{ES} vs ΔE plot is shown in figure 5.8. The upper plot shows the ΔE-M_{ES} plane with grand-side-band and signal box. The bottom plots show the ΔE and M_{ES} distributions.

We observed 18 events inside the signal region. This is consistent with zero signal.

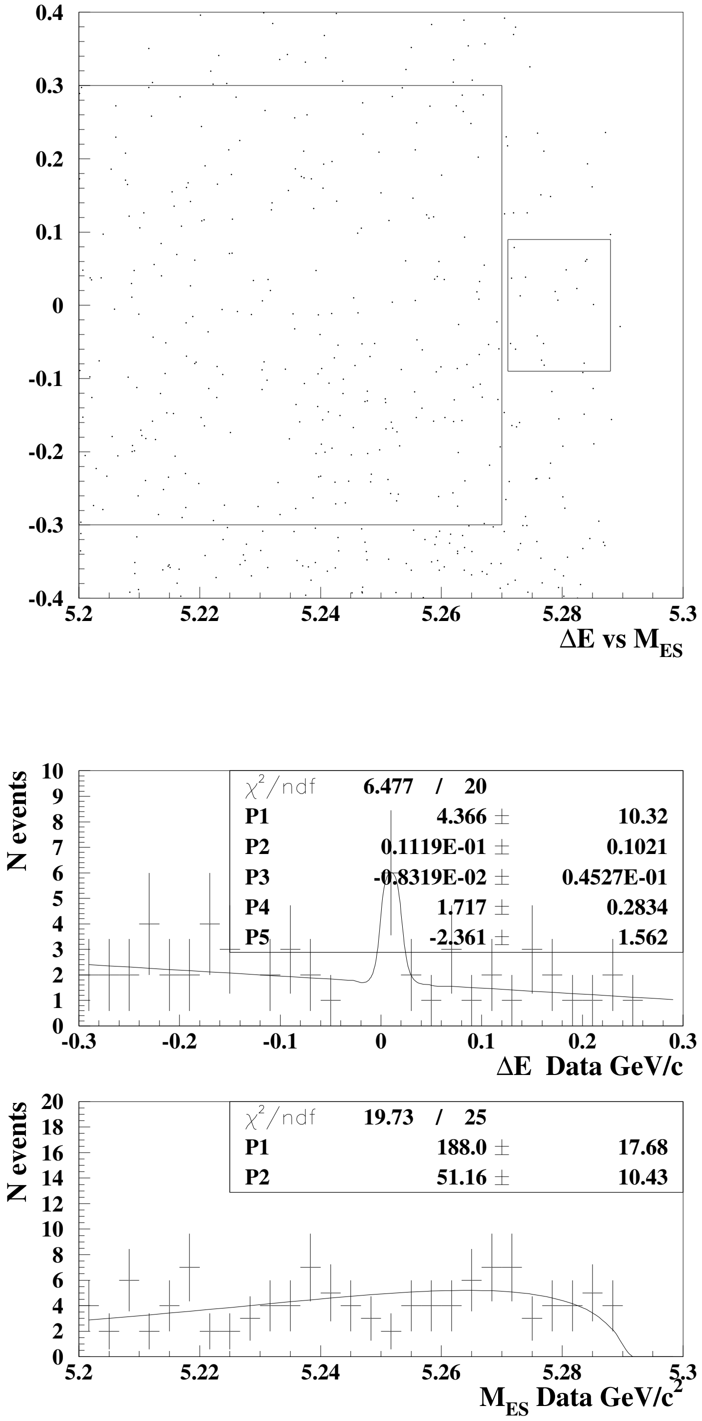

Figure 5.8: (Top) M_{ES} vs ΔE phase space with the signal box and grand-side-band overlaid. (Bottom two) shows the M_{ES} and ΔE distributions for the unblinded signal.

Hence we set an upper limit on the branching fraction $B(B^+ \to K^{*0}\pi^+,\ K^{*0} \to K_S^0\pi^0) < 3.0 \times 10^{-6}$ with 90% CL. This value has been calculated using the upper limit calculator provided by [31].

The upper limit calculator produces an approximate value based upon a Monte Carlo method. A trial value for the signal is taken, then it has background added, drawn from a gaussian of mean background b, and standard deviation σ_b, before being multiplied by a sensitivity drawn from a gaussian of mean S and standard deviation σ_S. The result is then used as the mean of a Poisson distribution from which a number of events r is generated. By counting the fraction of cases in which r is less than the observed number, the probabilities are generated.

The sensitivity is defined as the expected signal yield divided by its statistical uncertainty. However for these rare mode upper limit calculations we use the expected background for our sensitivity value.

The upper limit calculator provides three probability calculations, this report uses one recomended by the BaBar statistics working group. It is based on Bayesian intervals [32]. The calculator does not fully consider the case when observed events are smaller than background.

5.2 $B^+ \to K^{*+}\pi^0$, $K^{*+} \to K_S^0\pi^+$

This section describes the analysis for $B^+ \to K^{*+}\pi^0$, $K^{*+} \to K_S^0\pi^+$. The final state is accessible via either a tree or penguin decay. Table 5.12 shows the bounding limits on the signal and grand-side-band boxes as dictated by figure 5.9. The wider selection criteria in ΔE are due to the fast π^0.

Area	ΔE bounded GeV	M_{ES} bounded GeV/c^2
Signal Region	$\|\Delta E\| < 0.14$	$5.27 < M_{ES} < 5.288$
Grand Sideband	$\|\Delta E\| < 0.3$	$5.2 < M_{ES} < 5.269$

Table 5.12: The signal box and grandside band box as calculated from 6000 Monte Carlo mode specific events.

Table 5.13 shows the effects of each successive cut. Figure 5.10 shows some of the signal characteristic distributions. The efficiency was calculated from 6000 Monte Carlo events and requiring each event to contain at least one candidate to ensure no bias by multi-counting. The result obtained from the table is an overall efficiency of 10.3%.

5.2.1 Background Characterisation

Figure 5.11 shows the shape of the background in the characterisation regions as described in Section 4.8. The calculated 'R' value is 0.092 ± 0.008, as seen in table 5.14

5.2.2 Unfolding the Helicity Angle

A study into unfolding the helicity distribution was made, however no asymmetry was observed.

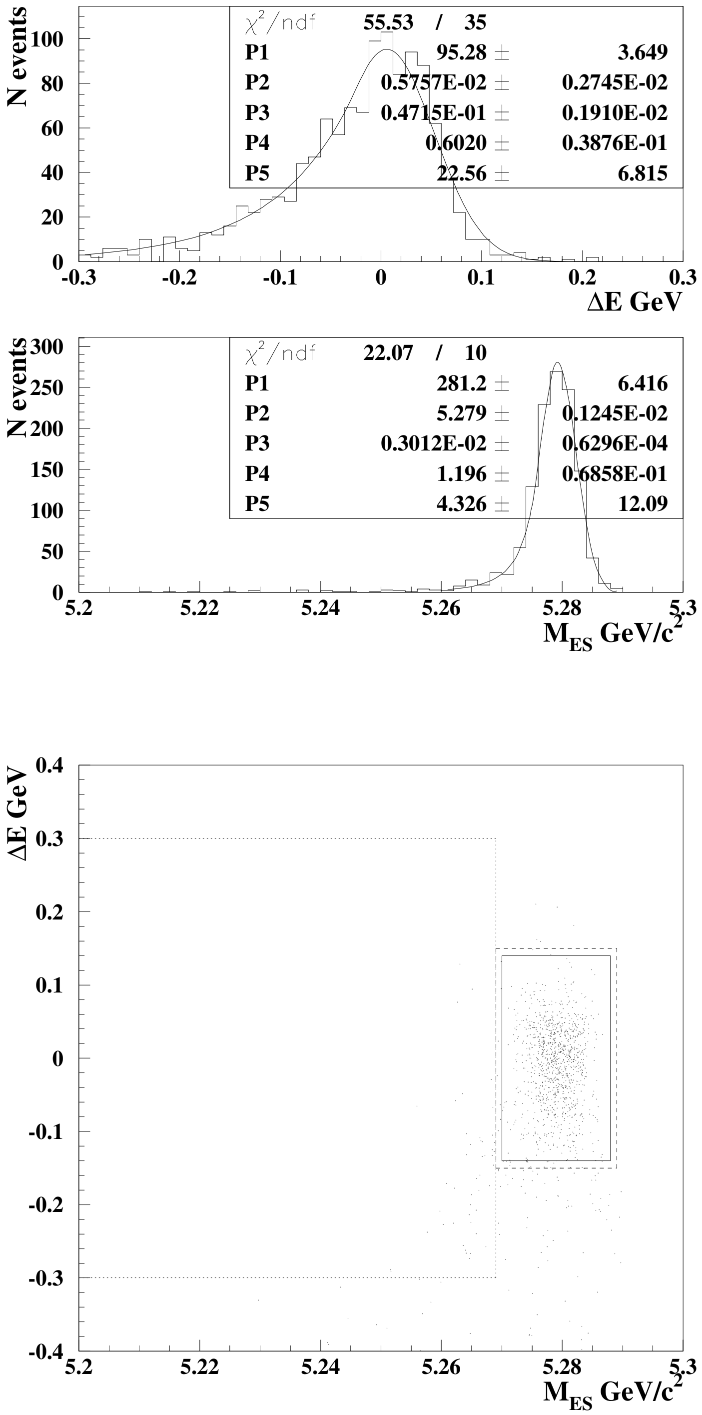

Figure 5.9: The top two plots shows the ΔE and M_{ES} distributions fitted with Crystal Ball functions. The bottom plot shows the constructed signal box.

$B^+ \to K^{*+}\pi^0$ Selection Cut Efficiencies (%)			
Selection Cut	Events	Mean Cand/Event	Efficiency
Preselection and signal Box	1393	1.4	23.2
$0.764 < M_{K^{*+}} < 1.020$ GeV/c^2	1170	1.2	19.5
e^- veto (track $E/p < 0.9$)	1150	1.1	19.2
track 1 Not a Kaon	1131	1.1	18.9
Fisher < 1.5	937	1.1	15.6
$\lvert \cos\theta_H \rvert > 0.3$	922	1.1	15.4
$\lvert \cos\theta_T \rvert < 0.8$	777	1.1	13.0
$0.490 < m_{K^0_S} < 0.506$ GeV/c^2	720	1.1	12.0
$c\,\tau \,/\, \sigma_{c\tau} > 4$	695	1.1	11.6
$E_\gamma > 0.03$ GeV	653	1.0	10.9
$0 < LAT < 0.6$	648	1.0	10.8
$\lvert M_{\gamma\gamma} - m_{\pi^0} \rvert < 0.02$ GeV/c^2	619	1.0	10.3
Total Raw Efficiency, $\epsilon_{raw\ MC}$	619	1.0	10.3

Table 5.13: Initial selection criteria with corresponding total efficiency. Efficiency is shown as the overall efficiency. Only resolved π^0's are used.

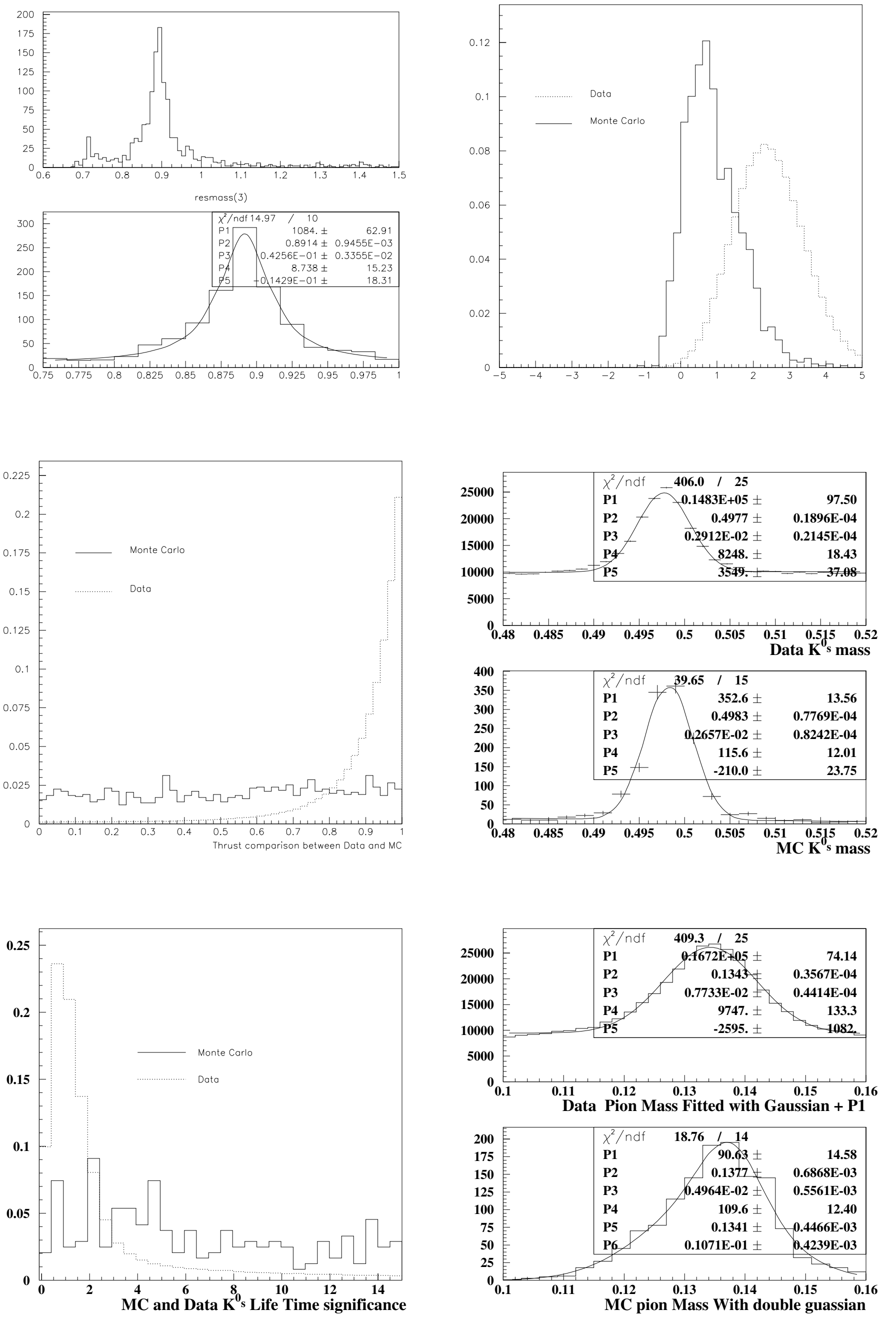

Figure 5.10: This figure shows the event shape distributions for $B^+ \to K^{*+}\pi^0$. From top left to bottom right we have the Monte Carlo K^{*+} resonant mass fitted with a Breit-Wigner, the Fisher discriminant for Monte Carlo and Data, the thrust comparison for Monte Carlo and Data, K_S^0 mass fitted with a gaussian to a linear background, the lifetime significance variable and the π^0 mass for Monte Carlo and Data.

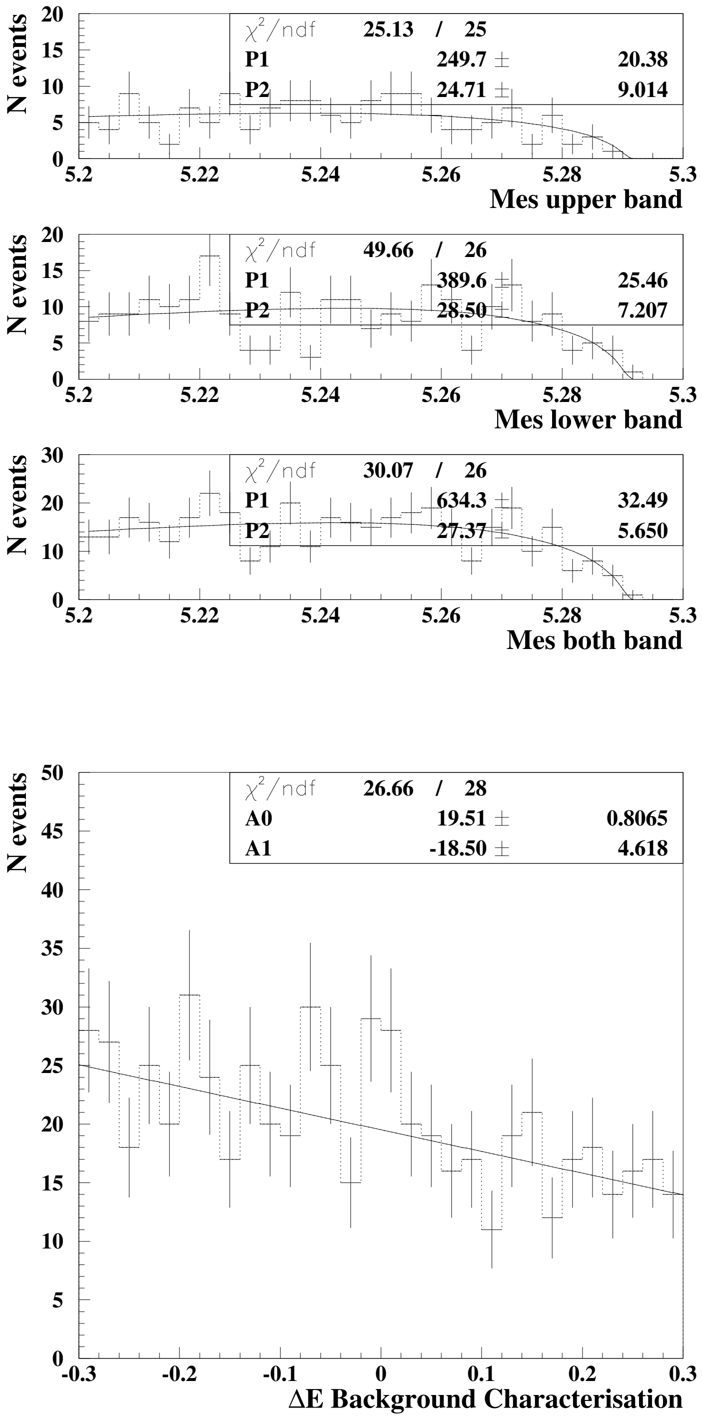

Figure 5.11: The top three plots show the M_{ES} upper, lower and combination bands, all fitted with an Argus shape. The bottom plot shows the ΔE distribution fitted with a first order polynomial.

Argus parameter value	
Area fitted	Value
Upper Band	24.7 ± 9.0
Lower Band	28.5 ± 7.2
Both Bands	27.4 ± 5.7

Table 5.14: The Argus ξ parameter for data after applying selection criteria and best candidate selection. We used the combined value for our characterisation.

5.2.3 Selection Optimisation

We again optimised using the method covered in section 4.9. We used the upper limit stated in Table 4.1 as an assumed value for the branching fraction to calculate S in the optimisation. Studies were conducted into using a smaller branching fraction than the upper limit stated, but the result gave a much reduced efficiency($\approx 5\%$). Also reduced statistics resulted in the breakdown of any reasonable results. Criteria optimised are:

- Mass K^{*+} optimised over range $\pm 1\sigma$ to $\pm 5\sigma$.
- The Fisher discriminant was optimised over range 0.25 to 2.
- $|\cos\theta_H|$ optimised over range 0. to 0.7.
- $|\cos\theta_T|$ optimised over range 0.5 to 0.9.
- Mass K_s^0 optimised with respect to fitted mass distribution over range $\pm 1\sigma$ to $\pm 6\sigma$.
- Lifetime significance is optimised over range 2 to 10.
- Photon energies are optimised together over range 30 MeV to 300 MeV.
- Lateral energy distribution is optimised over the range 0.3 to 0.8.
- Reconstructed π^0 mass optimised with respect to fitted mass ranging from $\pm 1\sigma$ to $\pm 7\sigma$.

Efficiency values for optimised cuts are shown in Table 5.16. We re-characterise the background distribution to obtain a new 'R' value. Figure 5.12 shows the new background distributions whose value is given in table 5.15. Again the combined Argus parameter was taken. The new 'R' value is found to be 0.080 ± 0.013

Argus parameter value	
Area fitted	Value
Both Bands	18.3 ± 10.7

Table 5.15: ξ value after optimisation.

5.2.4 Background Studies

Background studies were again conducted in order to identify possible contaminants. Studies were conducted on generic B decays (both charged and neutral), light quark modes ($e^+e^- \rightarrow u\overline{u}, d\overline{d}, s\overline{s}$), charm events ($e^+e^- \rightarrow c\overline{c}$) and on a cocktail of rare charmless modes. The cocktail incorporates rare two, three and four body final states. Table 5.17 shows the results of these searches.

Checks were again conducted into possible cross channel contamination. The optimised selection criteria were applied to 6000 Monte Carlo mode specific $B^+ \rightarrow K^{*0}\pi^+$, $K^{*0} \rightarrow K^0_s\pi^0$ and $B^+ \rightarrow \rho^+ K^0_s$, $\rho^+ \rightarrow \pi^+\pi^0$ events. The 16 events passing the selection conditions equate to 1 event in the signal region for the luminosity used in this analysis. A further check was again also conducted on 22,000 $B^+ \rightarrow K^+K^{*0}$, $K^{*0} \rightarrow K^0_s\pi^0$ events. No events were observed passing the selection criteria. The results are given in table 5.18.

5.2.5 Efficiency Corrections

Table 5.19 contains all corrections applied to our Monte Carlo signal efficiency. Again corrections are applied to several of our selection criteria with the errors on these

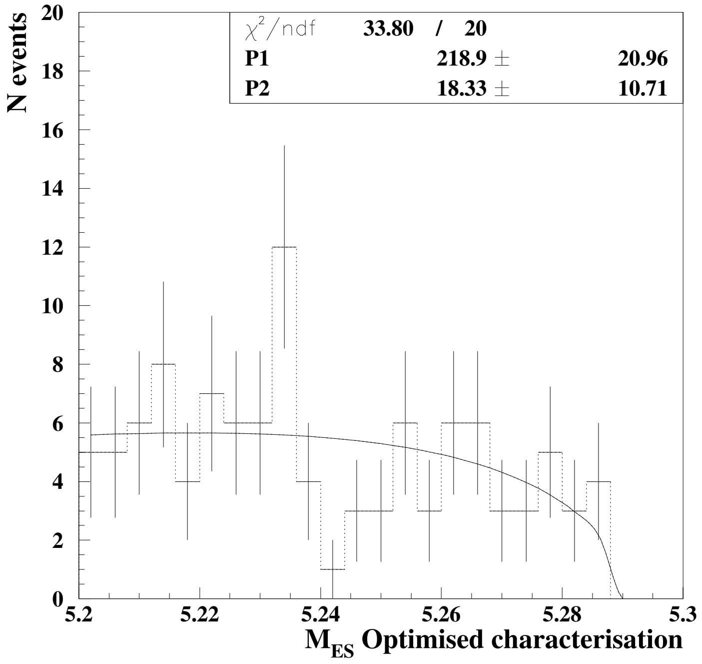

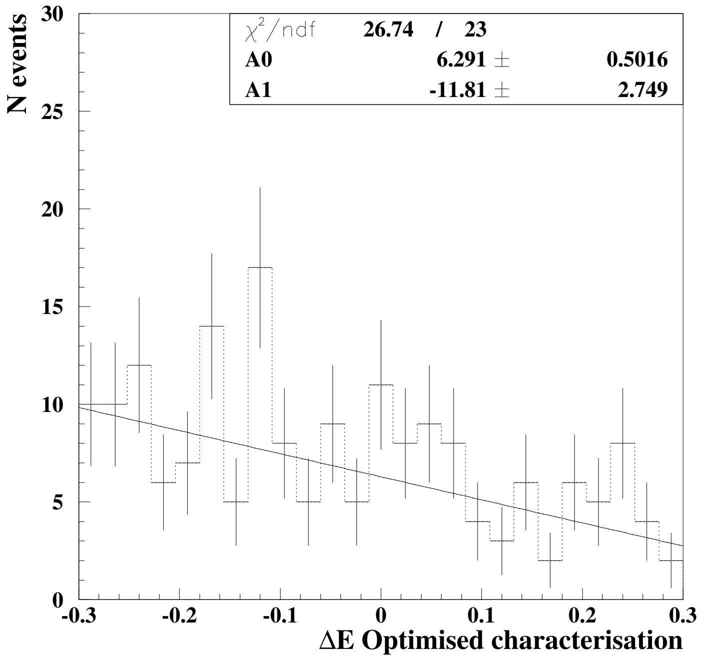

Figure 5.12: $B^+ \to K^{*+}\pi^0$ M_{ES} and ΔE distributions after optimisation.

$B^+ \to K^{*+}\pi^0$ Selection Cut Efficiencies (%)			
Selection Cut	Events	Efficiency	Number of events in GSB
Preselection and signal Box	1393	23.2	NA
0.700 GeV/c^2 $< M_{K^{*+}} <$ 1.084 GeV/c^2	1276	21.3	110674
e^- veto (track $E/p < 0.9$)	1256	20.9	105418
track 1 Not a Kaon	1239	20.7	95995
Fisher < 0.75	652	10.9	2422
$\lvert\cos\theta_H\rvert > 0.3$	635	10.6	1766
$\lvert\cos\theta_T\rvert < 0.75$	613	10.2	1339
$0.487 < m_{K^0_S} < 0.508$ GeV/c^2	590	9.8	1110
$c\,\tau\ /\ \sigma_{c\tau} > 7$	566	9.4	472
$E_\gamma > 0.03$ GeV	540	9.0	396
$0 < LAT < 0.6$	535	8.9	396
$0.105 < M_{\gamma\gamma} < 0.165$ GeV/c^2	535	8.9	391
Total Raw Efficiency, $\epsilon_{raw\ MC}$	535	8.9	391

Table 5.16: Efficiencies after optimised cuts have been applied. Efficiency is given as the total efficiency. Only resolved π^0's are used.

	Events (10^6)	Events in Signal Region	Scaled
B^+B^-	4.5	0.0	0.0
$B^0\overline{B^0}$	3.7	0.0	0.0
$c\overline{c}$	12.1	3	6
uds	18.1	8	16
Charmless Cocktail	1.1	8	8

Table 5.17: Results of the check into possible contamination modes.

Resonant Mode	Events selected	Events in Signal region
$K^{*0}\pi^+$	0	0
$\rho^+K_s^0$	10	1
$B^+ \to K^+K^{*0}$, $K^{*0} \to K_S^0\pi^0$	0	0

Table 5.18: Possible cross channel contamination check.

corrections providing the systematic uncertainty of the cuts. Just like the previously discussed mode there is only one charged track we need to concern ourselves with. The $\pi^+\pi^-$ that make up the K_s^0 are dealt with separately. We again impose the Tracking Efficiency working group recommendations [20] with the systematic of 1.2% for our GoodTracksLoose candidate. The K_s^0 Monte Carlo correction also comes from the Tracking Efficiency working group. A systematic of 2.6% is applied. Particle Identification corrections are conducted using the recommended PID tables and method as before. The π^0 corrections are made in accordance with the recommendations made by the Neutral Identification and Reconstruction AWG [26].

Corrections to Monte Carlo ΔE and M_{ES} distributions were studied using a control sample with a fast π^0. $B^+ \to \overline{D}^0\rho^+$, $\overline{D}^0 \to K^+\pi^-$, $\rho^+ \to \pi^+\pi^0$, with the helicity angle of the ρ restricted to allow only the faster half of the π^0 distribution, has a similar π^0 spectrum to the signal. This channel has previously been studied in [29]. The results showed agreement between Monte Carlo and data. However large uncertainties on the means and resolution of the data distributions were observed. M_{ES} errors on the mean and resolution were found to be ± 0.5 MeV/c^2 and ± 0.2MeV/c^2 respectively. ΔE errors on the mean and resolution were observed to be ± 10 MeV/c^2 and ± 5MeV/c^2 respectively. The correction is 1.0 with the error being calculated by varying the resolutions and means of the functions fitted to Monte Carlo signal by the errors in the calibration channel and measuring the integral between the cuts, as explained in Appendix B.

	Correction
Tracking	0.973 ± 0.012
K_s^0	0.964 ± 0.026
π^0	0.900 ± 0.050
PID	0.992 ± 0.008
ΔE	$1.000^{+0.025}_{-0.026}$
M_{ES}	$1.000^{+0.011}_{-0.017}$
TOTAL	$0.837^{+0.068}_{-0.069}$

Table 5.19: This table shows the relevant corrections to be applied to our overall Monte Carlo calculated efficiency.

5.2.6 Results

The results for this analysis are given in table 5.20. They show the expected number of events to be observed after the analysis is unblinded.

Events in GSB	391
Ratio R	0.080 ± 0.013
Expected BG in SR	$39.2 \pm 1.6 \pm 9.5$

Table 5.20: Summary of background study and the number of expected events in the signal region. Again we include the charmless events in the overall expected backgrounds.

The optimised selection criterion gave 391 events in the grand-side-band. Re-characterising the background gave a product ratio of $R = 0.080 \pm 0.013$. Combining these two (RN_{sig}) with the 8 ± 8 expected background events from charmless cocktail we achieve an expected background number in the signal region of $39.2 \pm 1.6 \pm 9.5$. The largest systematic was found to be from the charmless background. No estimate on the number of signal events was hypothesised as optimisation was conducted with an upper limit instead of a branching fraction.

The unblinded results are shown in figure 5.13. The top plot shows the the ΔE-M_{ES} distributions while the bottom two plots show the projections of the ΔE and M_{ES} on to their relative axis. From these plots it is clear that a signal cannot be obtained.

We observed 26 events in the signal region. This is consistent with zero signal. We set an upper limit on the branching fraction $B(B^+ \rightarrow K^{*+}\pi^0,\ K^{*+} \rightarrow K^0_S\pi^+)$ $< 1 \times 10^{-7}$ at 90%CL. This value has again been calculated using the upper limit calculator provided by [31].

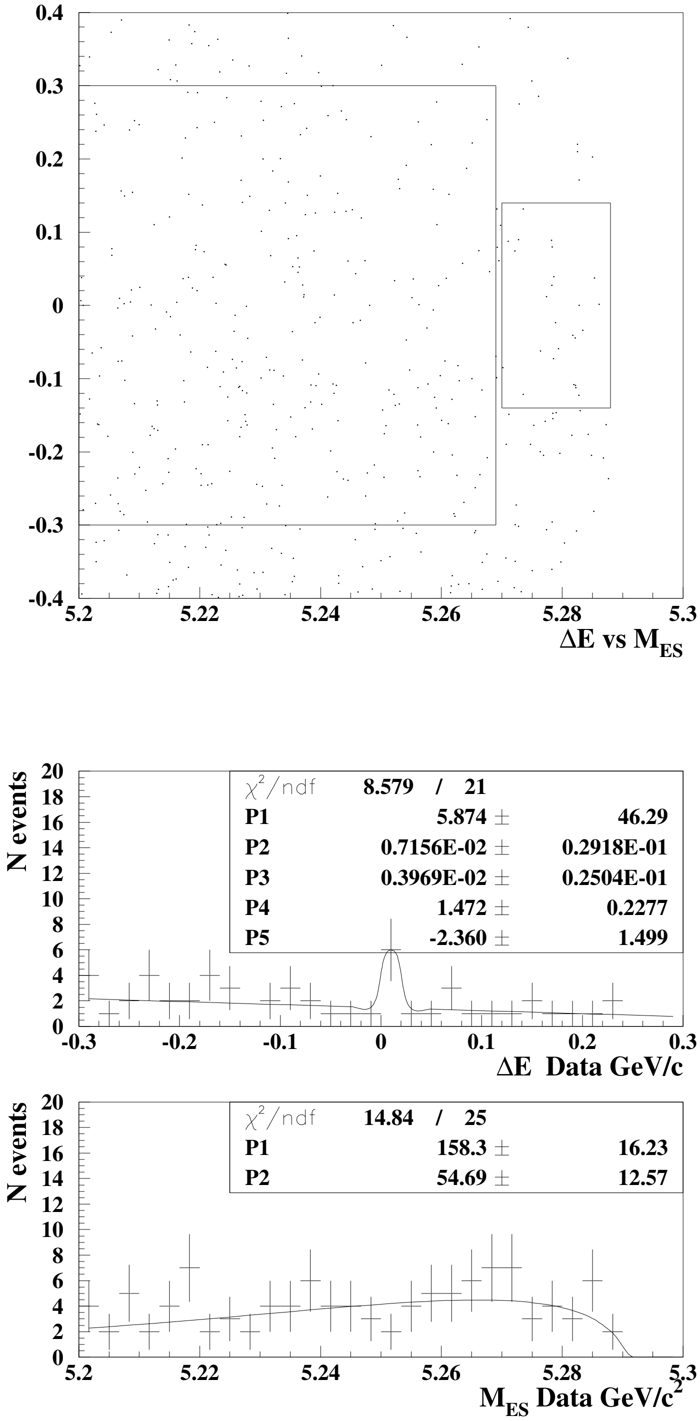

Figure 5.13: Top plot shows the M_{ES}-ΔE phase space with the signal box and grand-side-band overlaid. The lower plots show the M_{ES} and ΔE distributions for the unblinded signal.

5.3 $B^+ \to \rho^+ K_S^0$

This section describes the analysis $B^+ \to \rho^+ K_S^0$, $\rho^+ \to \pi^0 \pi^+$. Table 5.21 contains the bounding limits on the signal and grand-side-band boxes as shown by figure 5.14.

Area	ΔE bounded GeV	M_{ES} bounded GeV/c^2
Signal Region	$\|\Delta E\| < 0.096$ GeV	$5.27 < M_{ES} < 5.288$ GeV/c^2
Grand Sideband	$\|\Delta E\| < 0.3$ GeV	$5.2 < M_{ES} < 5.269$ GeV/c^2

Table 5.21: The signal box and grand-side-band box as calculated from 6000 Monte Carlo mode specific events.

Table 5.22 shows the effects of each successive selection criterion as it is imposed. Conducted on 6000 Monte Carlo events and requiring each event to contain at least one candidate we ensure no bias by multi-counting. Here the result obtained from the table is an overall efficiency of 14.3%. Some of the distribution comparisons are shown in Figure 5.15.

5.3.1 Background Characterisation

Figure 5.16 shows the shape of the background in the characterisation regions as described in Section 4.8. The calculated 'R' value is 0.051 ± 0.003, as calculated from the Argus parameter shown in table 5.23.

5.3.2 Unfolding the Helicity Angle

A study into unfolding the helicity selection was made, however no asymmetry was observed.

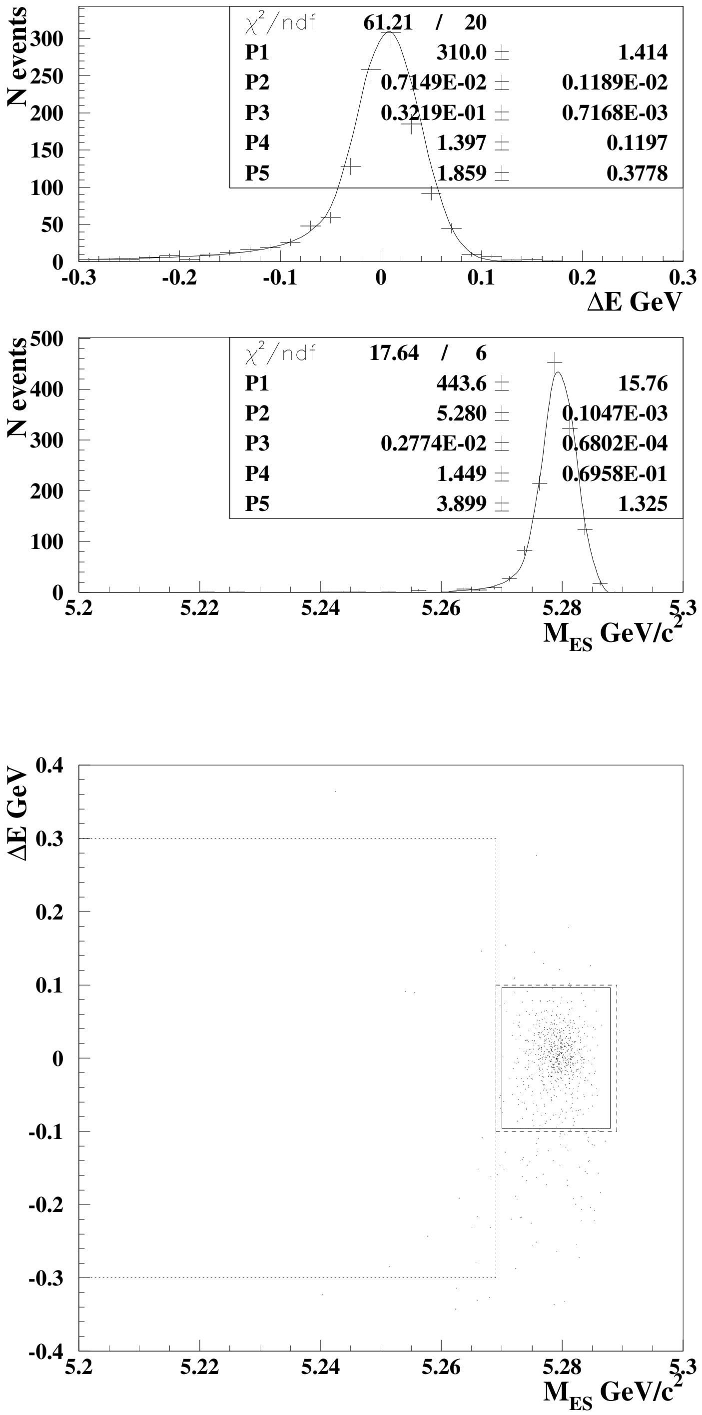

Figure 5.14: The top two plots show the ΔE and M_{ES} distributions. The bottom plot shows the constructed signal box.

$B^+ \to \rho^+ K^0_S$ Selection Cut Efficiencies (%)			
Selection Cut	Events	Mean Cand/Event	Efficiency
Preselection and signal Box	1583	2.2	26.4
$0.490 < M_{\rho+} < 1.050$ GeV/c^2	1402	1.9	23.4
e^- veto (track $E/p < 0.9$)	1389	1.9	23.2
track 1 Not a Kaon	1358	1.9	22.6
Fisher < 2.0	1264	1.8	21.1
$\lvert\cos\theta_H\rvert > 0.3$	1236	1.7	20.6
$\lvert\cos\theta_T\rvert < 0.8$	1013	1.7	16.9
$0.489 < m_{K^0_S} < 0.506$ GeV/c^2	955	1.7	15.9
$c\,\tau\ /\ \sigma_{c\tau} > 3$	938	1.6	15.6
$E_\gamma > 0.03$ GeV	925	1.6	15.4
$0 < LAT < 0.6$	916	1.5	15.3
$\lvert M_{\gamma\gamma} - m_{\pi^0}\rvert < 0.02$ GeV/c^2	860	1.5	14.3
Total Raw Efficiency, $\epsilon_{raw\ MC}$	860	1.5	14.3

Table 5.22: Initial selection criteria with corresponding total efficiency. Again only resolved π^0's are used.

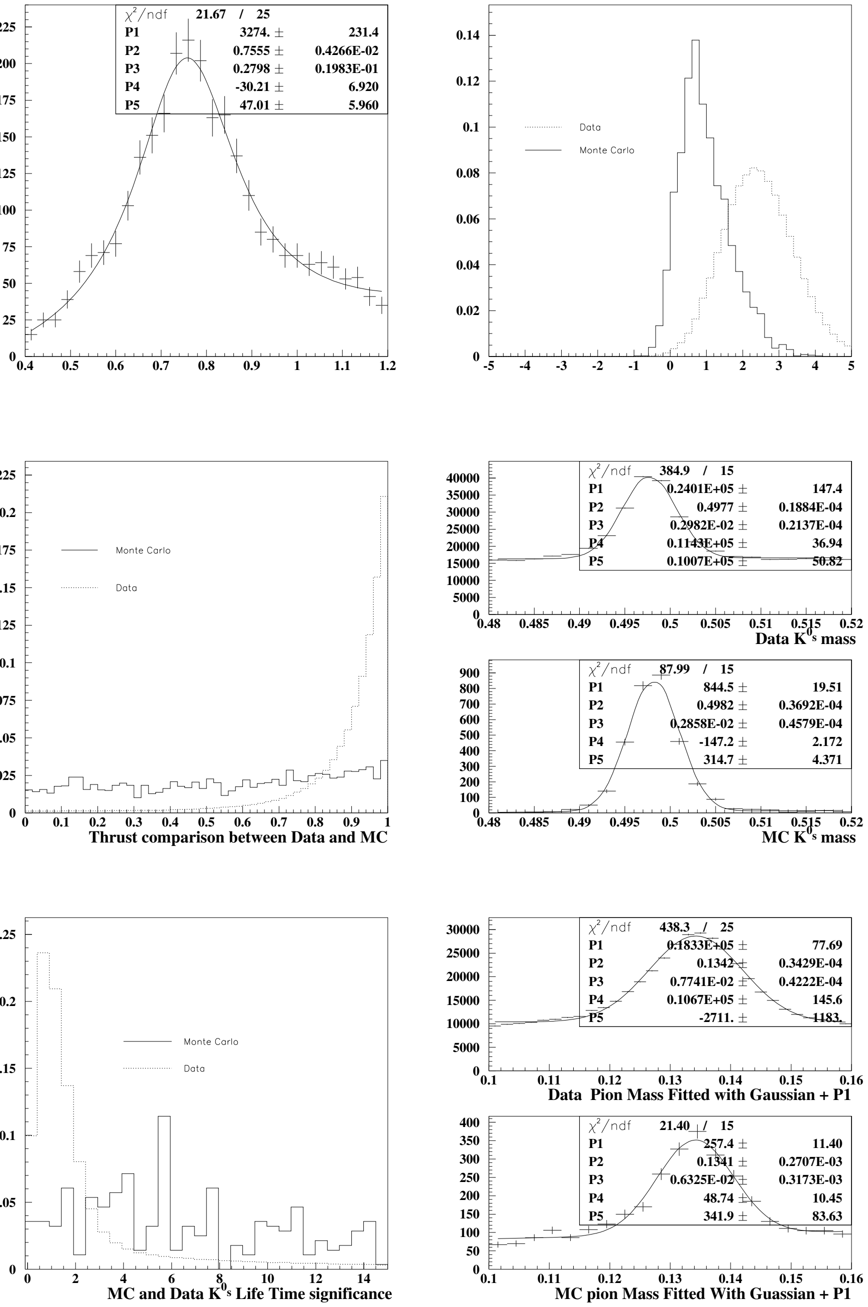

Figure 5.15: This figure shows the event shape distributions for $B^+ \to \rho^+ K^0_S$. From top left to bottom right we have the Monte Carlo ρ^+ resonant mass fitted with a Breit-Wigner, The Fisher discriminant for Monte Carlo and Data, the thrust angle comparison for Monte Carlo and Data, K^0_S mass fitted with a gaussian to a linear background, the lifetime significance variable and the π^0 mass for Monte Carlo and Data.

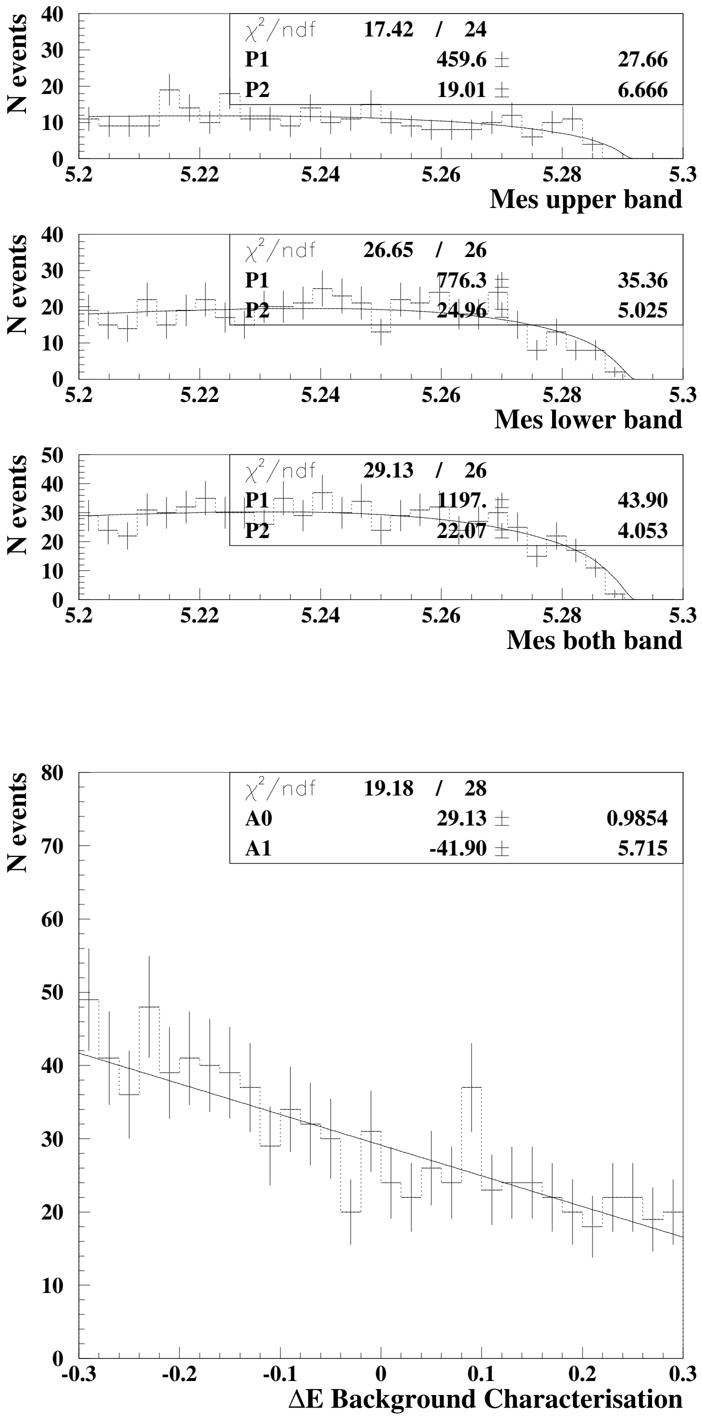

Figure 5.16: The top three plots show the M_{ES} upper, lower and combination bands, all fitted with an Argus shape. The bottom plot shows the ΔE distribution fitted with a first order polynomial background.

Argus parameter value	
Area fitted	Value
Upper Band	19.0 ± 6.7
Lower Band	25.0 ± 5.0
Both Bands	22.1 ± 4.1

Table 5.23: The Argus ξ parameter for data after applying selection criteria and best candidate selection. We use the combined value for our characterisation.

5.3.3 Selection Optimisation

Again we optimise the cuts. After each parameter is optimised we update the value and continue. Criteria optimised were:

- Mass ρ^+ optimised over range $420 < M_{\rho^+} < 1120$ MeV/c^2.
- Fisher optimised over range 0.5 to 2.5.
- $|\cos\theta_H|$ optimised over range 0.1 to 0.8.
- $|\cos\theta_T|$ optimised over range 0.4 to 0.9.
- Mass K_s^0 optimised with respect to fitted mass distribution over range $\pm 1\sigma$ to $\pm 5\sigma$.
- Lifetime significance is optimised over range 2 to 9.
- Photon energies are optimised together over range 30 MeV to 200 MeV.
- Lateral energy distribution is optimised over the range 0.4 to 0.8.
- Reconstructed π^0 mass optimised range $110 < M_{\pi^0} < 160$ MeV/c^2.

Efficiency values for optimised cuts are given in Table 5.25. Now we have the optimised values we re-characterise the background distribution to obtain a new 'R' value. Figure 5.17 shows the new background distributions whose value is given in table 5.24. Again the combined Argus parameter is taken.

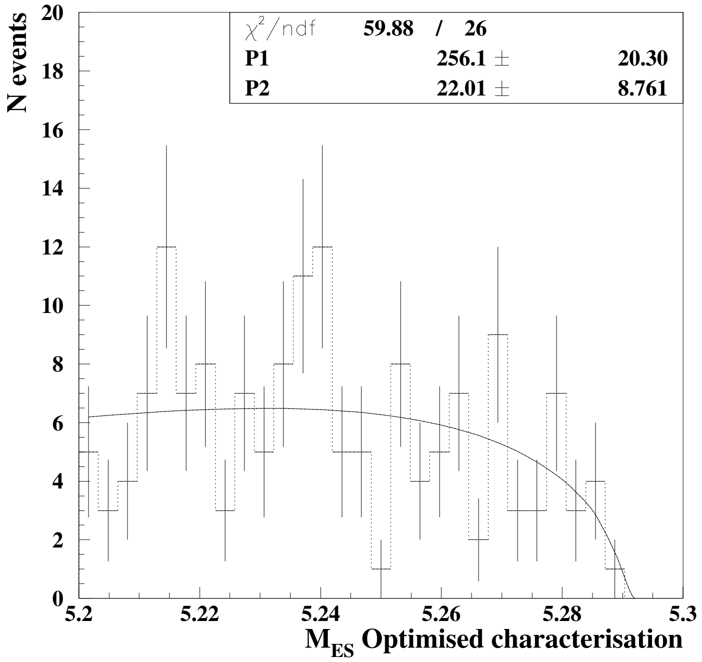

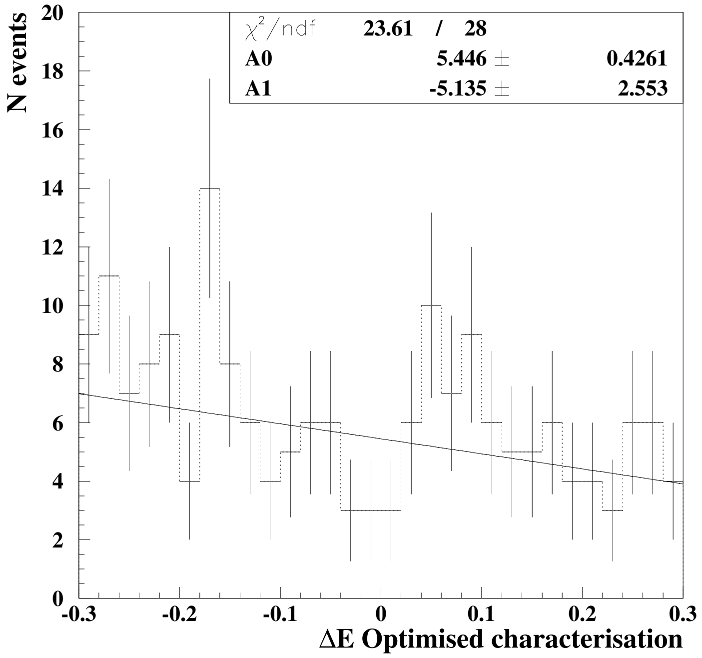

Figure 5.17: $B^+ \to \rho^+ K^0_S$ M_{ES} and ΔE distributions after optimisation.

Argus parameter value	
Area fitted	Value
Both Bands	22.0 ± 8.8

Table 5.24: ξ value after optimisation

5.3.4 Background Studies

Background studies were conducted in order to identify possible contaminants. Studies were made on generic B decays (both charged and neutral), light quark modes ($e^+e^- \to u\overline{u}, d\overline{d}, s\overline{s}$), charm events ($e^+e^- \to c\overline{c}$) and on a cocktail of rare charmless modes. The cocktail incorporates rare two, three and four body final states. Table 5.26 shows the results of these searches.

Checks were again done on possible cross channel contamination. The optimised selection criteria were applied to 6000 Monte Carlo mode specific $B^+ \to K^{*0}\pi^+$, $K^{*0} \to K^0_s\pi^0$ and $B^+ \to K^{*+}\pi^0$, $K^{*+} \to K^0_S\pi^+$ events. The 17 events passing the selection conditions equate to 1 event in the signal region, again for the luminosity used in this analysis. A further check was conducted on 22,000 $B^+ \to K^+K^{*0}$, $K^{*0} \to K^0_s\pi^0$ events. Again optimised selection criteria were applied resulting in 16 events being selected. This equated to 0 events in the signal region. The results are given in table 5.27.

5.3.5 Efficiency corrections

The efficiency corrections follow the same method as that covered in section 5.1.5. Table 5.28 contains all corrections applied to our Monte Carlo signal efficiency.

To correct for the uncertainty in the Monte Carlo ΔE and M_{ES} distributions a control sample was used, in this case $B^+ \to \overline{D}^0\pi^+$ with $\overline{D}^0 \to K^0_S\pi^+\pi^-$. This channel has been studied previously [33]. The correction was obtained as described in Appendix A. The errors were calculated by adding in quadrature Monte Carlo fit errors and those

$B^+ \to \rho^+ K^0_S$ Selection Cut Efficiencies (%)			
Selection Cut	Events	Efficiency	Number of Events in the GSB
Preselection and signal Box	1583	26.4	NA
$0.620 < M_{\rho+} < 0.920$ GeV/c^2	1164	19.4	167280
e^- veto (track $E/p < 0.9$)	1152	19.2	162406
track 1 Not a Kaon	1122	18.7	131016
Fisher < 1.0	733	12.2	7683
$\vert\cos\theta_H\vert > 0.3$	714	11.9	1664
$\vert\cos\theta_T\vert < 0.8$	676	11.3	1182
$0.486 < m_{K^0_S} < 0.509$ GeV/c^2	661	11.0	933
$c\,\tau\ /\ \sigma_{c\tau} > 4$	642	10.7	402
$E_\gamma > 0.03$ GeV	633	10.6	375
$0 < LAT < 0.6$	629	10.5	375
$110 < M_{\gamma\gamma} < 0.160$ GeV/c^2	617	10.3	360
Total Raw Efficiency, $\epsilon_{raw\ MC}$	617	10.3	360

Table 5.25: Efficiencies after optimisation of selection criteria have been applied. Again only resolved π^0's are used.

	Events (10^6)	Events in Signal region	Scaled
B^+B^-	4.5	0.0	0.0
$B^0\overline{B^0}$	3.7	1.0	6.0
$c\overline{c}$	12.1	4.0	8.0
uds	18.1	9	18
Charmless Cocktail	1.1	7	7

Table 5.26: Shows results of the check into possible contamination modes.

Resonant Mode	Events selected	Events in Signal region
$K^{*+}\pi^0$	17	1
$K^{*0}\pi^+$	0	0
$B^+ \to K^+K^{*0}$, $K^{*0} \to K_S^0\pi^0$	16	0

Table 5.27: Possible cross channel contamination check.

calculated from the calibration channel and varying the resolutions and means of the functions fitted to Monte Carlo signal before measuring the integral between the cuts.

5.3.6 Results

The results for this analysis are given in table 5.29. They show the expected number of events to be observed after the analysis is unblinded.

The optimised selection criteria give 360 events in the grand-side-band. Re-characterising the background gives us a product ratio of $R = 0.050 \pm 0.007$. Combining these two (RN_{sig}) with the expected events from charmless cocktail we achieve an expected background number in the signal region of $25.0 \pm 1.0 \pm 7.4$. Again our dominant systematic is due to charmless backgrounds with low statistics. Larger data sets should reduce this effect.

The unblinded results are shown in figure 5.18. The top plot shows the the ΔE-

	Correction
Tracking	0.973 ± 0.012
K_s^0	0.964 ± 0.026
π^0	0.939 ± 0.047
PID	0.991 ± 0.009
ΔE	$0.982^{+0.002}_{-0.003}$
M_{ES}	0.998 ± 0.002
TOTAL	0.857 ± 0.056

Table 5.28: This table shows the relevant corrections to be applied to our overall Monte Carlo calculated efficiency.

Events in GSB	360
Ratio R	0.050 ± 0.007
Expected BG in SR	$25.0 \pm 1.0 \pm 7.4$

Table 5.29: Summary of results with total expected number of background events in the signal region.

M_{ES} distributions while the bottom two plots show the projections of ΔE and M_{ES} on to their respective axis. From these plots it is again clear that a signal cannot be obtained.

We observed 15 events in the signal region. This is consistent with zero signal. We set an upper limit on the branching fraction $B(B^+ \to \rho^+ K_S^0, \rho^+ \to \pi^+\pi^0) < 8\times10^{-7}$ at 90%CL. This value has again been calculated using the upper limit calculator provided by [31].

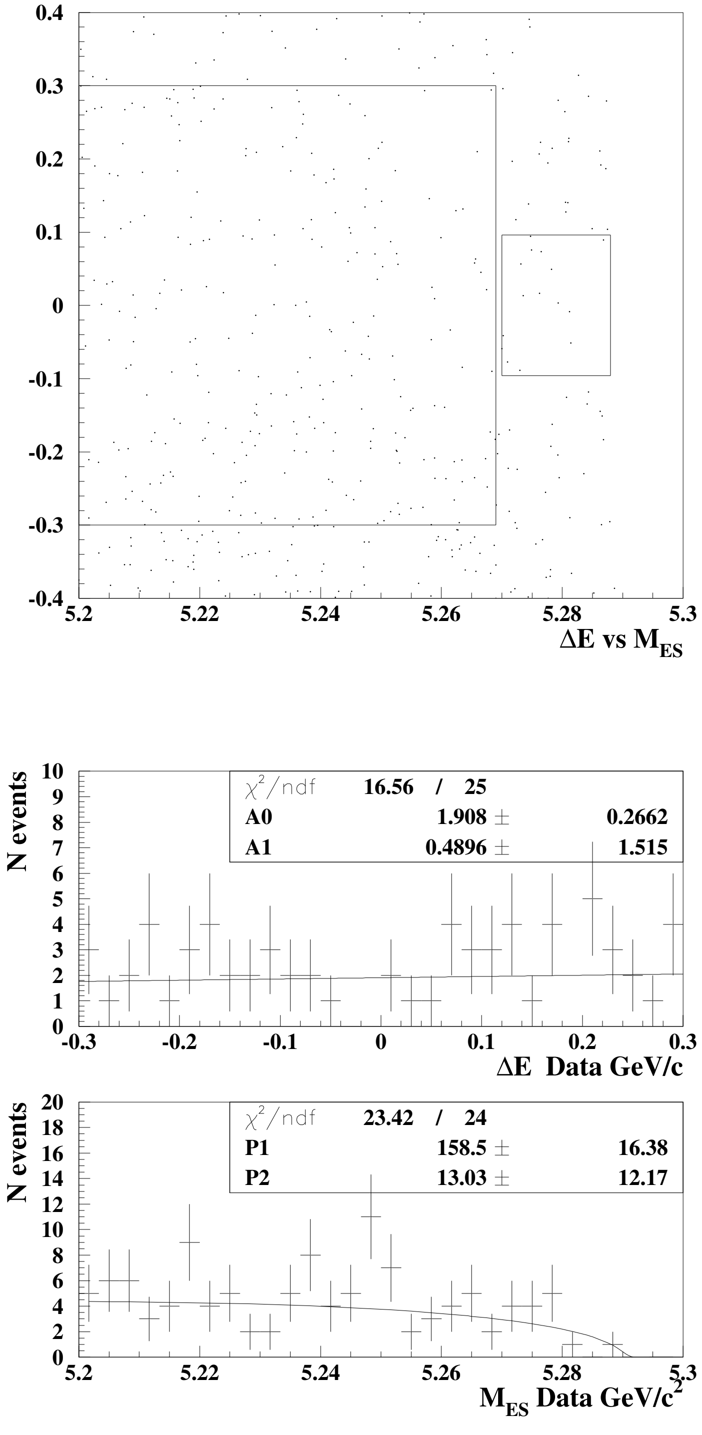

Figure 5.18: Top plot shows the M_{ES}-ΔE phase space with the signal box and grand-side-band overlaid. The lower plots show the M_{ES} and ΔE distributions for the unblinded signal.

5.4 Chapter Summary

Upper limits on the following branching fractions have been measured using data and Monte Carlo obtained from the BaBar collaboration. The results are:

$B(B \to K^{*0}\pi^+, K^{*0} \to K^0_S\pi^0) \; < 3 \times 10^{-6}$ 90%CL
$B(B \to K^{*+}\pi^0, K^{*+} \to K^0_S\pi^+) \; < 1 \times 10^{-7}$ 90%CL
$B(B \to K^0_S\rho^+, \rho^+ \to \pi^0\pi^+) \; < 8 \times 10^{-7}$ 90%CL

By dividing out the known branching fractions from secondary decays we can represent these results in terms of limits on the following:

$B(B \to K^{*0}\pi^+) \; < 2 \times 10^{-5}$ 90%CL
$B(B \to K^{*+}\pi^0) \; < 3 \times 10^{-7}$ 90%CL
$B(B \to K^0_S\rho^+) \; < 8 \times 10^{-7}$ 90%CL

While $B \to K^{*0}\pi^+$ is consistent with previous published results [24] $B \to K^{*+}\pi^0$ and $B \to K^0_S\rho^+$ results represent tighter constraints than previously published results [24].

No theoretical predictions could be found to corroborate the rare three body final state results mentioned above.

Chapter 6

Report Summary

Chapter one introduced the baryon asymmetry mystery and the CP hypothesised solution. In chapter two we introduced the concept of Charge Conjugation and Parity, with a discussion on how they can be combined to form the CP operator. It showed how CP violation may arise in field theory and how it is generated within the Standard Model. We looked at how its effects can be examined through constraining the CKM matrix, and mybe interpreted graphically through the Unitarity Triangle. In presenting the Unitarity Triangle evidence was presented in favour of using the B meson to study CP violation. A discussion on the types of CP violation in the B meson system was also given. An introduction to charmless haronic B decays, and their importance was also presented, along with the modes studied in this report. Finally a brief explanation of how possible new physics could manifest themselves in this system was presented.

Details on the Stanford Linear Accelerator, PEP-II system and BaBar detectors have been presented in chapter three. Here explanations were given as to how the PEP-II−BaBar system is arranged, and why this is so. The chapter then gave a detailed breakdown of the sub detectors present in the BaBar detector and their function in the experiment.

Chapter four discussed the analysis techniques and selection variables used in this report. The final results of the discussed methods of chapter four were finally presented in chapter five, cumulating in the upper limits given at the end of chapter five.

This report lays the foundation for future work in many areas of B physics, CP violation and possible new physics. It is hoped that the reader has enjoyed reading this report as much as I had compiling it.

Appendix A

Crystal Ball Function

The signal ΔE distribution is modelled on a Crystal Ball function. The Crystal Ball function is defined as:

$$C(\Delta E) = e^{\frac{(\Delta E - m)^2}{2\sigma^2}} \quad \text{if } \Delta\text{E} > m - \alpha\sigma \tag{A.1}$$

$$C(\Delta E) = \frac{(\frac{n}{\alpha})^n e^{-\frac{\alpha^2}{2}}}{(\frac{m - \Delta E}{\sigma} + \frac{n}{\alpha} - \alpha)^n} \quad \text{if } \Delta\text{E} \leq m - \alpha\sigma \tag{A.2}$$

where m is the position of the maximum. The parameter α determines the cross-over point from a Gaussian behaviour to a power-law, and is expressed in units of the peak width σ. The parameter n is a real number that enters into the power-law portion of the function.

Appendix B

ΔE-M_{ES} Efficiency Correction Method

The correction to the ΔE-M_{ES} Monte Carlo efficiency is achieved through calibration channels of similar kinematics. The corrections are calculated by varying the resolutions and means of the functions fitted to the Monte Carlo signal, by the errors in the calibration channel and measuring the integral between the cuts.

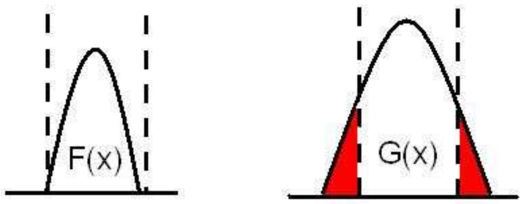

Figure B.1: This diagram represents the distribution function for both ΔE and M_{ES} before efficiency corrections (F(x)) and after corrections have been added (G(x)). The ratio of these distributions gives our correction factor

Figure B.1 represents the distribution function for both ΔE and M_{ES} before efficiency corrections (F(x)) and after corrections have been added (G(x)). The ratio of these distributions gives our correction factor. Errors are added in quadrature before being applied to F(x). Errors on the mean and width of the distributions are calculated independently before they are combined. An example follows.

B.1 $B^+ \rightarrow K^{*0}\pi^+$

B.1.1 ΔE

ΔE Crystal Ball Function	Monte Carlo	Data
Mean	(4.4 ± 1.1)MeV	(1.2 ± 4.3)MeV
Width	(29.0 ± 1.0)MeV	(30.2 ± 3.8)MeV
Amplitude	297.5	297.5
Merge Point	1.125	1.125
Power	3.146	3.146

Table B.1: Shows the Crystal Ball function values for the decay $B^+ \rightarrow K^{*0}\pi^+$ with the data values being obtained by application of the $B^+ \rightarrow \overline{D}^0\pi^+$ Monte Carlo and data calibration comparisons. Here we have fixed the amplitude, merge point and power function.

Table B.1 shows the results of the calibration channel Monte Carlo-Data comparison. The differences are added to our Monte Carlo signal channel to produce an estimated data signal response. We observed a shifting of the mean and an increase in the width. The remaining parameters of the Crystal Ball function were fixed. The efficiency correction becomes:

$$H = \frac{\int_a^b G(x)\ dx}{\int_a^b F(x)\ dx} = 0.992 \tag{B.1}$$

H is the correction factor, a and b are the limits defined by the initial signal box cuts, in the case of this example limits -0.09 to $+0.09$. Errors are added in quadrature.

$$\pm\text{Mean} = \sqrt{(1.1)^2 + (4.3)^2} = 4.4\text{MeV}, \pm\ \text{Width} = \sqrt{(1.0)^2 + (3.8)^2} = 3.9\text{MeV} \quad \text{(B.2)}$$

Each is then applied separately to F(x,σ).

Mean errors:

$$+ve = \left| \int_a^b F(x,\sigma)dx - \int_a^b F(x+\delta x,\sigma)\ dx \right| = +0.004 \quad \text{(B.3)}$$

$$-ve = \left| \int_a^b F(x,\sigma)dx - \int_a^b F(x-\delta x,\sigma)\ dx \right| = -0.004 \quad \text{(B.4)}$$

Width errors:

$$+ve = \left| \int_a^b F(x,\sigma)dx - \int_a^b F(x,\sigma+\delta\sigma)\ dx \right| = +0.016 \quad \text{(B.5)}$$

$$-ve = \left| \int_a^b F(x,\sigma)dx - \int_a^b F(x,\sigma-\delta\sigma)\ dx \right| = -0.014 \quad \text{(B.6)}$$

Total ΔE efficiency corrections for $B^+ \to K^{*0}\pi^+$ is:

$$\Delta E_{correction} = 0.992^{+0.016}_{-0.015} \quad \text{(B.7)}$$

where errors are created in quadrature.

B.1.2 M_{ES}

Table B.2 shows the results of the calibration channel Monte Calo-Data comparison. Again we observed a shifting of the mean and an increase in the width and we fix the remaining parameters of the Crystal Ball function. Efficiency corrections are:

$$H = \frac{\int_a^b G(x)\ dx}{\int_a^b F(x)\ dx} = 0.978 \quad \text{(B.8)}$$

M_{ES} Crystal Ball Function	Monte Carlo	Data
Mean	(5.279 ± 0.0001)GeV	(5.279 ± 0.0005)GeV
Width	(2.6 ± 0.1)MeV	(3.2 ± 0.4)MeV
Amplitude	191.7	191.7
Merge Point	0.944	0.944
Power	18.1	18.1

Table B.2: Shows the Crystal Ball function values for the decay $B^+ \to K^{*0}\pi^+$ with the data values being obtained by application of the $B^+ \to \overline{D}^0\pi^+$ Monte Carlo and data calibration comparisons. Here we have fixed the amplitude, merge point and power funtion.

H is the correction factor, a and b are the limits defined by the initial signal box cuts. In the case of M_{ES} they are 5.272 GeV and 5.288 GeV respectivily. The errors are again added in quadrature.

$$\pm\text{Mean} = \sqrt{(0.1)^2 + (0.5)^2} = \pm 0.5\text{MeV}, \pm \text{ Width} = \sqrt{(0.1)^2 + (0.4)^2} = \pm 0.5\text{MeV} \tag{B.9}$$

Each is then applied separately to F(x,σ).

Mean errors:

$$+ve = \left| \int_a^b F(x,\sigma)dx - \int_a^b F(x+\delta x,\sigma)\ dx \right| = +0.005 \tag{B.10}$$

$$-ve = \left| \int_a^b F(x,\sigma)dx - \int_a^b F(x-\delta x,\sigma)\ dx \right| = -0.006 \tag{B.11}$$

Width errors:

$$+ve = \left| \int_a^b F(x,\sigma)dx - \int_a^b F(x,\sigma+\delta\sigma)\ dx \right| = +0.017 \tag{B.12}$$

$$-ve = \left| \int_a^b F(x,\sigma)dx - \int_a^b F(x,\sigma-\delta\sigma)\ dx \right| = -0.014 \tag{B.13}$$

Total ΔE efficiency corrections for $B^+ \to K^{*0}\pi^+$ is:

$$M_{ES_{\text{correction}}} = 0.978^{+0.018}_{-0.015} \tag{B.14}$$

where errors are created in quadrature.

Bibliography

[1] J. H. Christenson, J.W. Cronin, V.L. Fitch, R. Turlay, Phys. Rev. Lett. 13, p 138, 1964.

[2] A. D. Sakharov, ZhETF Pis. Red. 5 32; JETP Lett. 5, p. 24 1967

[3] The BABAR Physics Book, Physics at an Aysmmetric B Factory, SLAC-R-504, ed. P.F. Harrison and H.R. Quinn (BABAR Collaboration), 1998.

[4] J. W. Herb et al Phys. Rev. Lett. 39 p252 (1977)

[5] The BABAR Collaboration "Observation of CP violation in the B^0 meson system" Phys. Rev. Lett. 87, (2001)

[6] M. Kobayashi and T. Maskawa. CP violation in the renormalizable theory of weak interactions. Prog. Theor. Phys. 49(1973) p652.

[7] N. Cabibbo. Phys. Rev. Lett., 10(1963) p531

[8] The European Physics Journal, Review of Particle Physics, Vol 15. Num1-4, 2000 p.110

[9] C. Jarlskog. Phys. Rev. Lett. 55(1985) p1039

[10] M. Neubert B decays and CP violation, Int. J. Mod. Phys. A11, 4173(1996) hep-ph/9604412

[11] L. Wolfenstein. Phys. Rev. Lett., 51(1983) p1945

[12] The BaBar Collaboration Technical Design Report, March 1995.

[13] Official DCH Performance Plots
http://www.slac.stanford.edu/BFROOT/www/Physics/official/DCH/index.html

[14] Luminosity Measurements for Run I and Run II data using SP4 Simulation, R. Gamet, R. Parry, C Touramanis. BaBar Analysis Document # 535 Version 1.

[15] N. Chevalier and A. Anjomshoaa, A Study of $B \to K^*\pi$, BaBar Analysis Document #232 (2001).

[16] Study of three-body charmless B decays at Belle, BELLE-CONF-0114,

[17] D. M. Asner et al., Search for Exclusive Charmless Hadronic B Decays, Physical Review D 53, p1039 (1996)

[18] K. Lingel, T. Skwarnicki, J. G. Smith, Penguin Decay Of B Mesons, SLAC-PUB-7796

[19] E. Varnes et al, Measurements of the GoodTrackLoose efficiency using SVT tracks, BaBar Analysis Document #157 Version 6.

[20] Tracking Efficiency Task Force
http://www.slac.stanford.edu/BFROOT/www/Physics/TrackEfficTaskForce/
TrackingTaskForce-2001.html

[21] P. F. Harrison et al, Studies of Three-Body Charmless Hadronic B Decays, BaBar Analysis Document #36

[22] B. Dunwoodie, Simple Observations on B Bbar Kinematics.
http://www.slac.stanford.edu/ wmd/bbkinematics/kinematics.note

[23] W. T. Ford, Choice of Kinematic Variables in B Meson Reconstruction, BaBar Analysis Document #53 Version 5.

[24] Parictle Data Group Particle Physics Booklet July2002.

[25] BaBar Particle Identification Action Working Group, http://www.slac.stanford.edu/BFROOT/www/Physics/Tools/Pid/pid.html.

[26] Neutral Identification and Reconstruction AWG, Studies on π^0 reconstruction Status report, BaBar Analysis Document #20

[27] G. Mancinelli, S. Spanier, Kaon Selection at the BABAR Experiment, BABAR Note 116 Version 1.0.

[28] A. Hocker, A Maximum Likelihood Method for DIRC Particle Identification, BaBar Analysis Document #23 Version 2.

[29] F. Bianchi, M. Bona, J. Olsen, Measurement of Branching Fraction for Charmless $B^- \to h^+ h^0$ Decays, BaBar Analysis Document #98 Version 5

[30] M. Bona, R. Faccini, M. Langer, $K_S^0 \to \pi^+\pi^-$ reconstruction, BaBar Analysis Document#19, Version 5.

[31] R. Barlow, A Calculator for Confidence Intervals, BaBar Analysis Document #340

[32] R. Barlow et al, Recommended Statistical Procedures for BaBar, BaBar Analysis Document #318 version 2.

[33] L. Mir, A. Gritsan, Search for the $B^+ \to \rho K^*$ and $B^+ \to \rho^0 \rho^+$, BaBar Analysis Document #483